Dielectric focusing elements for integrated optics

Brian David Jennings

A thesis presented for the degree of
Doctor of Philosophy

13th March 2018

Declaration

I declare that this thesis has not been submitted as an exercise for a degree at this or any other university and that it is entirely my own work.

I agree to deposit this thesis in the University's open access institutional repository or allow the Library to do so on my behalf, subject to Irish Copyright Legislation and Trinity College Library conditions of use and acknowledgement.

I have read and I understand the plagiarism provisions in the General Regulations of the University Calendar for 2017–18, found at `http://www.tcd.ie/calendar`. I have also completed the Online Tutorial on avoiding plagiarism 'Ready Steady Write', located at `http://tcd-ie.libguides.com/plagiarism/ready-steady-write`.

Summary

Planar, dielectric waveguides are a key component for directing and routing light in integrated optical devices. These waveguides support discrete solutions to the wave equation (called *modes*) and depending on the size of the waveguide's core, either a single mode or multiple modes are supported. In this thesis, the control and focusing of light in slab and rectangular planar, dielectric waveguides in both the single and multiple mode regimes are discussed. Analytical and numerical modelling are used to design structures which focus guided modes through refraction and diffraction of light. The structures are fabricated in silicon nitride and investigated in the visible light regime. Two imaging techniques are used to experimentally study the samples: the first images the light from within the structures that is scattered at the edges, surfaces or other discontinuities in the waveguide, and the second images the fluorescence of a dye-doped film coated on the waveguide core excited by light within the structures. Rectangular waveguides of varying width and slab waveguides are both investigated.

In a slab waveguide—where the width of the waveguide is effectively infinite—multiple modes propagating simultaneously cause interference. It is shown that the interference pattern resulting from mode beating in the planar waveguides can be used to determine the difference of the effective refractive indexes of the modes. In rectangular waveguides which have a width of a few microns, the intensity distribution around bends and along tapers was mapped experimentally to demonstrate the bend loss and multi-mode interference.

The first focusing element investigated is a dielectric disk a few micrometres in diameter. The disk is positioned at the *output* of the waveguide and is made of the same material as the core of the waveguide. The disk focuses light through refraction but due to its size (relative to the wavelength), diffraction of the incident beam also plays a considerable role. The position of the focal spot depends on the ratio of disk's refractive index to the surrounding medium's refractive index. Here, two regimes are studied: the focal spot within the disk when the surrounding medium is air, and the focal spot outside the disk when the surrounding medium is poly-vinyl acetate (PVA). In the first case, measurements of the focal spot are diffraction limited in the experimental set-up used (this limit is about ~550 nm) and in the second, divergence of the beam in the direction of the cylinder axis reduces the intensity at the focus (though focusing is still observed). Simulations of both conditions reinforce experimental observations and predict focal spots as small as 220 nm ($\sim 0.41\lambda_0$) for the first case.

The second focusing element investigated is a purely diffractive element similar to a Fresnel zone plate and is based on an array of cylindrical holes in the core of the waveguide. The design differs significantly from the design of a standard far-field zone plate as the focal spot is still in the Fresnel diffraction region. The holes are a few hundred nanometres in diameter and are partially filled with PVA that is coated on the silicon nitride layer. Light propagating within the waveguide is scattered by the holes and by deliberately positioning

each of the holes, a focus can be produced. The position and diameter of each hole is determined analytically by considering the amplitude and phase calculated from the Mie solution for scattering from a cylinder. Although some light is lost to scattering out of the waveguide, having the focusing element incorporated in the waveguide is advantageous for the lack of divergence. Computational simulations of these *scattering lenses* predicted focal spots ~250 nm. Experimental measurements show good agreement with the predicted scattered fields but are limited by the resolution of the imaging set-up.

Finally, a conclusion and future outlook for focusing elements in planar, dielectric waveguides are provided.

Acknowledgements

I would like to thank my supervisor, Prof. John Donegan, for giving me the opportunity to do research as a postgraduate student and for his guidance over the last four years. I would also like to thank Prof. David McCloskey for his encouragement and time, as well as endless teaching and training.

I thank Alan Bell and Dermot Daly for their training on the EBL and FIB systems which were used to fabricate almost all of the structures presented here. I would also like to recognise our own research group and the larger photonics group in college for lots of help with questions, ideas, equipment and presentation practice during this research.

I would like to thank my family for taking an interest in my project and for their support over the last four years, particularly over the final few months.

On the social side, I would like to thank my friends for keeping me interested in things outside physics over the last four years. I would especially like to mention Andrew, Chuan, Enda C., Enda H., Ertuğrul, James, John, Kyle, Michael, Oliver, Romina and Ronan, everyone I shared the office with and all the people from the weekly football games.

I would like to acknowledge the Irish Research Council for funding the project.

Publications

B. D. Jennings, D. McCloskey, J. J. Gough, T. Hoang, N. Abadía, C. Zhong, E. Karademir, A. L. Bradley and J. F. Donegan, "Characterisation of multi-mode propagation in silicon nitride slab waveguides", *Journal of Optics*, vol. 19, no. 1, p. 015604 (2017).

B. D. Jennings, N. Abadía, C. Zhong, E. Karademir, D. McCloskey and J. F. Donegan, "Fluorescence imaging of waveguide mode beating and propagation in tapered and bend regions", in *Conference on Lasers and Electro-Optics*, Optical Society of America (California, 2016), SM1F.6.

B. D. Jennings, N. Abadía, C. Zhong, E. Karademir, D. McCloskey and J. F. Donegan, "Fluorescence imaging of multi-mode propagation in waveguide bends and tapers", in *Advanced Laser Technologies* (Galway, 2016), SN-P-5.

B. D. Jennings, D. McCloskey, J. F. Donegan, "Focusing elements in dielectric waveguides", in *Photonics Ireland* (Cork, 2015).

Dielectric focusing elements for integrated optics

Brian David Jennings

Abstract

The ability to propagate light around a 'circuit' on a single chip has an abundance of applications. Connecting different elements can bring huge functionality to a minuscule device—as evidenced by integrated electronic circuits. To make full use of the benefits afforded by integrated optical circuits, elements of different sizes and materials will need to be used. To do this, connections between relatively large waveguides and sub-micron elements and vice-versa will be made. In this thesis, the propagation of light in multi-mode waveguides is presented; these waveguides form the connections between the different elements. Dielectric focusing elements, used to decrease the beam width as it moves from one element to another are also discussed. The different structures are studied through simulation and experiment. The focusing elements operate in different regimes: one a structure separate from the waveguide, gathering the light radiated from the end-face of the waveguide; the other a *perturbation* of the core of the waveguide, redirecting the light propagating through it. The dielectric focusing elements were initially intended as couplers to more powerful plasmonic focusing elements but can find use in a host of applications.

Contents

1 Introduction

Dielectric waveguides in the form of optical fibres have been used for decades in industrial applications. This is in part due to the high quality of fabrication of optical fibres. In recent years, similarly high standards have been reached in both the deposition of dielectric thin films and the fabrication processes for microscale and nanoscale structures. This has led to the emergence of planar photonics and photonic integrated circuits where light is confined to thin films and dielectric waveguides of rectangular cross section. The ability to confine and manipulate light in these waveguides alongside other optical components, on the scale of micrometres, will prove advantageous to many applications. One application already taking advantage is heat assisted magnetic recording which requires planar photonic components—a laser, waveguide and focusing elements—to be integrated with the magnetic recording apparatus.

The aim of this work was to design a micrometre-scale light focusing element to be used in heat assisted magnetic recording. This intention arose from previous research within our group which was based on light scattering by dielectric disks a few micrometres in diameter. The research used the microdisk as a stand-alone element illuminated directly by a laser beam and showed that it had favourable light focusing capabilities such as a subwavelength beam waist, high light gathering efficiency and control over the 'focal length'. Although plasmonic elements can produce smaller focal spots, dielectric focusing elements do not suffer from the intrinsic losses of metals or from heating while still focusing to spots a few hundred nanometres wide. A dielectric element could also be used to efficiently couple light into a plasmonic structure for further confinement.

1.1 Heat assisted magnetic recording

With more and more people using the internet as a source of information and entertainment, the need for large-scale data storage is ever increasing. Cloud computing and streaming services require vast quantities of information to be stored remotely (i.e., outside personal computers). The current means of industrial data storage is on hard disk drives (HDDs);

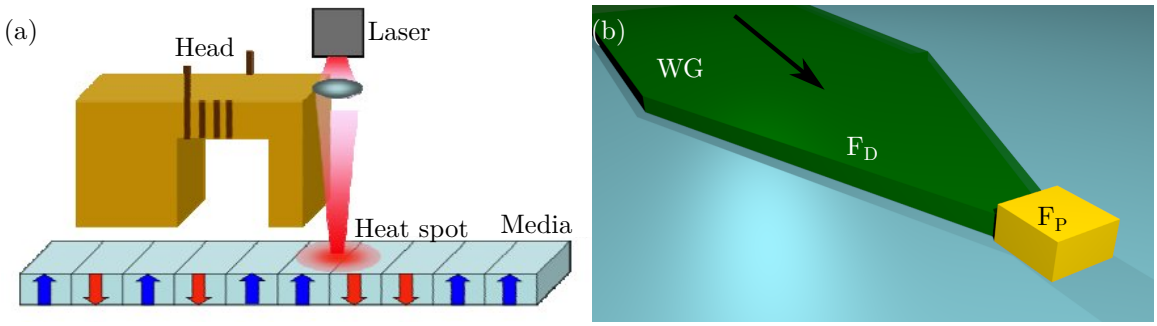

Figure 1.1 (a) Simplified schematic for HAMR operation [7]. A focused laser beam is used to heat the magnetic medium during recording. (b) Proposed focusing structure for use in a HAMR system. The laser is coupled to the waveguide (WG) and a dielectric focusing element (F_D) couples light to the plasmonic element (F_P) which focuses onto the magnetic medium. (Light propagates along the direction of the arrow.)

however, the conventional technology for writing information to HDDs—perpendicular magnetic recording (PMR)—is reaching the limit of its data storage density (see the ASTC roadmap [1]). To reach higher densities, new technologies are needed and the next advance in PMR is heat assisted magnetic recording (HAMR). HAMR allows for different materials to be used in the HDD: materials which can support higher densities. HAMR is expected to replace traditional PMR in the coming years, with Seagate planning to ship HAMR HDDs before the end of this year [2].

Magnetic recording has become an omnipresent means of data storage in this computer age. To store information, the magnetisation of a region (a *bit*) of the recording medium (the *disk*) is used. The disk is made of magnetic material and an electromagnet is used to magnetise a bit 'up' or 'down', aligning the dipoles along a given direction. A simplified version of the recording method in HAMR is shown in figure 1.1(a)—bits are magnetised at the narrower end of the electromagnet ("head") where the field is more concentrated and unaffected by the weaker field at the wider end. The energy required to reverse the magnetisation of a bit (i.e. to convert it from down to up) depends on the uniaxial anisotropy constant (K_u) of the disk material as well as the volume (V) of the bit as $E = K_u V$ [3]. As the bit size is decreased, the amount of energy required to reverse its magnetisation decreases and once a certain size is reached, the thermal energy available at room temperature is enough to cause the magnetisation to fluctuate. To guard against these fluctuations, hard disk manufacturers like to keep bit sizes larger than the limit set by $\frac{K_u V}{k_B T} \gtrsim 70$. Thus, if the areal density of hard disks (i.e., the number of bits per unit area) is to be increased, materials with larger K_u must be used.

Guarding against thermal fluctuations by using a magnetic material with higher K_u also increases the strength of the magnetic field needed to write the bit when desired. For the bit size that corresponds to 1 Tbit in^{-2} (~25 nm × 25 nm) the field strength is not feasible for an electromagnet that could be incorporated into a commercial HDD. However, the coercivity

of the material (i.e., the magnetic field strength needed to demagnetise it) decreases with increasing temperature and so temporarily heating individual bits while they are being written allows weaker magnetic fields to be used. This decrease happens sharply above the point known as the Curie temperature of the material [4]; FePt is the preferred material for HAMR and has a bulk Curie temperature of 750 K which can be lowered to 650 K by the inclusion of copper (FeCuPt, with 10% Cu) [5]. Thus, new materials can be used in PMR to achieve greater densities if localised heating of individual bits can be achieved; this is the basis of HAMR, which intends to achieve areal densities $>1\,\mathrm{Tbit\,in^{-2}}$ [6]. Optical energy has established itself as the preferred source for heating the magnetic medium during writing.

Using optical energy for heating is convenient because diode lasers are cost effective, are small enough to be integrated into the write head and output milliwatts of power—making high intensities when focused to nanometre scales. Light from a diode laser can be simply routed (e.g. through a waveguide) alongside the electromagnet and the laser switched on to heat each bit during writing. The difficulties associated with HAMR are related to efficiently focusing light to a spot similar in width to a bit and in the durability of the focusing element. To heat a single bit at a time, light must be focused to a spot much smaller than its wavelength which cannot be done so efficiently. To have a focal spot width similar to the bit size, a plasmonic focusing element is currently the best option and a number of different designs for an integrated HAMR head have been proposed and tested [8–13]. An example of a focusing structure is shown in figure 1.1(b) where a tapered dielectric waveguide couples light to a plasmonic transducer which heats the individual bit.

1.1.1 Dielectric focusing elements

The methods of coupling light from the dielectric waveguide into the plasmonic transducer fall into the categories of evanescent coupling—where the transducer extracts light from the waveguide—and a method similar to end-fire coupling—where light in the dielectric is focused onto the transducer [9, 14–16]. In this thesis, dielectric elements for the end-fire method are studied. In this geometry, the dielectric element is used to increase the intensity incident on the plasmonic transducer which may be less than a micrometre in size. As well as producing a small, intense focal spot, a suitable focusing element needs to have little or no back reflection so that no light returns to the laser.

Focusing elements direct light to a point by either refraction, reflection or diffraction or by a combination of them. The most prevalent focusing element is the glass lens, a refractive element that bends towards the focus the light incident on it. Perhaps the simplest dielectric focusing element is the taper: tapering the core of the waveguide causes the beam to narrow. However, tapering the core too sharply causes undesired scattering, to avoid this scattering the waveguide must be tapered adiabatically [17]. Free space focusing elements such as the lens can suggest design approaches for waveguide focusing elements but often the size of the waveguide structures and the field profiles of the modes means that simply scaling down

the size of the free space element won't give satisfactory results.

Focusing elements have a limit to how small a spot they can focus light to, given by

$$\text{FWHM} \approx \frac{0.51\lambda_0}{\text{NA}}$$

where FWHM is the full width at half maximum intensity of the spot (transverse to the direction of propagation), λ_0 is the free space wavelength, and NA ($= n \sin\theta$) is the numerical aperture of the focusing element. The NA depends on the range of angles made by light rays travelling from the focusing element to the focus (θ is the largest of these angles) and on the refractive index (n) of the medium where the focus forms. It is clear that gathering light from large angles to the focus and using a high refractive index medium, is important for creating a sub-wavelength spot. For dielectrics, 3–4 is usually considered a high refractive index; to focus light to smaller spots a different class of materials—plasmonics—needs to be used. Plasmonic elements are covered later in this section but first some of the state of the art dielectric focusing elements are introduced.

Mirrors are often used for focusing electromagnetic waves and have the advantage over refractive elements of being free from chromatic aberration [18]. To avoid significant spherical aberrations the mirror must have the shape of a parabola. A planar solid immersion mirror (PSIM) has been demonstrated as a focusing element [19]. The PSIM is somewhat similar to a taper in that the width of the waveguide is gradually made smaller (a schematic of the PSIM is shown in figure 1.2(a)). As a mode propagates along the waveguide it is reflected by the sidewalls toward the focal point; due to the high angle of incidence of the input mode and the sidewalls of the waveguide, there is total internal reflection. In [19], light was coupled into a slab waveguide millimetres away from the beginning of the PSIM (the material of the structures had a refractive index of 2.1). The focusing was measured using a near-field scanning optical microscope (NSOM) an image of which is shown in figure 1.2(b). The intense focus is clear and a focal spot size of 94 nm for an input wavelength of 413 nm was measured, suggesting a NA of greater than 2. One drawback of this type of focusing element is its size—50 µm × 100 µm.

An element similar to a regular lens, the solid immersion lens (SIL), has also been demonstrated for high NA focusing [22]. The SIL focuses light with a regular objective but places a high refractive index solid near the focus to further the confinement. A planar SIL was recently demonstrated [23]; though experiments were limited in measuring the NA, a theoretical value of 1.7 was predicted in simulations and corresponds to focusing to $\lambda/3.4$. This structure was still in the size range of $\gtrsim 10$ µm. Similar but smaller elements are the microsphere and microcylinder/microdisk which have been demonstrated as accomplished focusing elements.

Dielectric spheres with diameters of a few microns are known to focus light to sub-wavelength spot sizes and have been demonstrated for very high resolution optical applications [24, 25]. These microspheres can produce high intensity, slowly diverging focal spots (termed *photonic jets* or *nanojets*) depending on the refractive index ratio of the sphere to

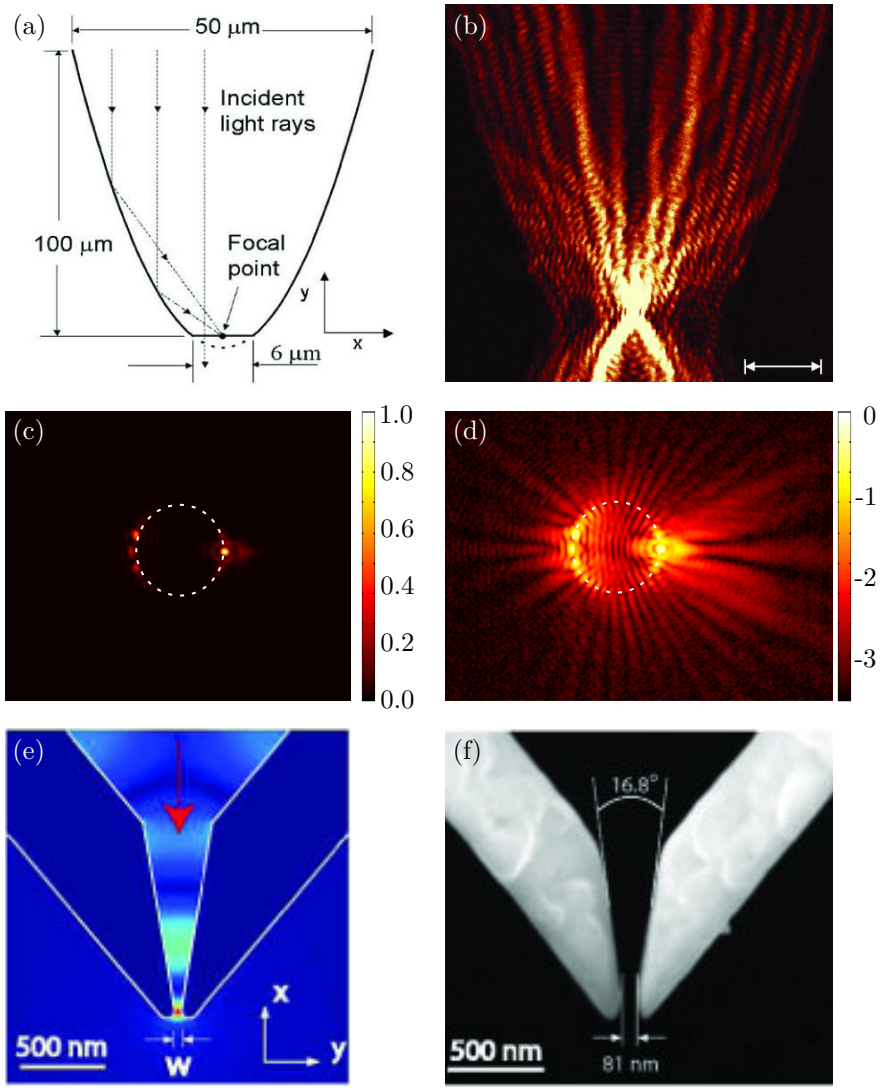

Figure 1.2 Examples of focusing elements. (a), (b) Geometry and SNOM measurement of a PSIM element that reflects an incident dielectric waveguide mode to a focal point [19]. The scale bar in (b) is 3 µm. (c), (d) Experimental scattered light image of a dielectric microdisk 6 µm in diameter illuminated by a laser beam; the intensity is plotted on linear and log scales, respectively [20]. (e), (f) Simulated intensity and scanning electron micrograph of a tapered metallic V-groove focusing element [21].

the surrounding medium [26–28]. The planar analogue of the microsphere, the microdisk, has demonstrated similar focusing capabilities [20, 29]. The microdisk brings light to a focus by a combination of refraction and diffraction. As it does so it gathers light from an area greater than its cross sectional size creating the high intensity focus. Experimental images of a Si_3N_4 disk with a diameter of 6 µm and a height of 400 nm are shown in figure 1.2(c) and (d). The disk was illuminated in free space by a laser and the scattered light was imaged. The refractive index ratio was such that the focus formed within the disk but the images exhibit the focusing effect that the disk has. (The intensity is plotted on a linear and log scale in (c) and (d), respectively.)

1.1.2 Plasmonic elements

Ultimately in a HAMR write head, a plasmonic transducer is used to transfer optical energy to the magnetic medium to cause heating. To focus to spot sizes of tens of nanometres or smaller, materials other than typical dielectrics need to be used. Plasmonic structures consisting of metals and dielectrics are capable of focusing to these sizes and are even capable of focusing to a few nanometres [30]. Plasmonic structures support modes at the metal dielectric interface; the modes are oscillations of the free electrons in the metal and can have frequencies equal to those of visible light [31]. The effective refractive indexes of these modes can be much larger than any standard dielectric and this is how plasmonic structures achieve such confinement of light. A plasmonic structure reported to focus light to $\lambda/_{40}$ is shown in figure 1.2(e) and (f) [21]. The tapered V-groove plasmon waveguide was fabricated in gold on a silicon wafer is shown in figure 1.2(e). The wide end of the taper was illuminated for tapers of different groove widths (w in figure 1.2(e)). It was found that the guided beam could be brought down to a width of 45 nm for $\lambda = 1.53$ µm. Specifically for HAMR, plasmonic structures such as a taper, a "nanobeak" and other transducers have demonstrated satisfactory focusing capabilities [12, 16, 32–34]. A drawback of plasmonic structures, however, is that they have intrinsic losses arising from the interband transitions of the metals and heating of the metals can be an issue at high intensities. Dissipating this heat to avoid damage of both the write head and the plasmonic element itself is one of the issues HAMR has had to overcome [35, 36].

1.2 Photonic integrated circuits

The past decade has seen extensive research into applications of confining light into thin films. Although work on this has been done for decades, current standards of fabrication processes along with the ever decreasing size and cost of lasers has led to an abundance of applications seeking to take advantage of integrated optical systems. As with the development of integrated circuits (ICs) in the electronics industry, interest in photonic integrated circuits (PICs) is driven by the improvements gained from having many components in a single, compact device. Integration has the advantage of reduced cost through simplified

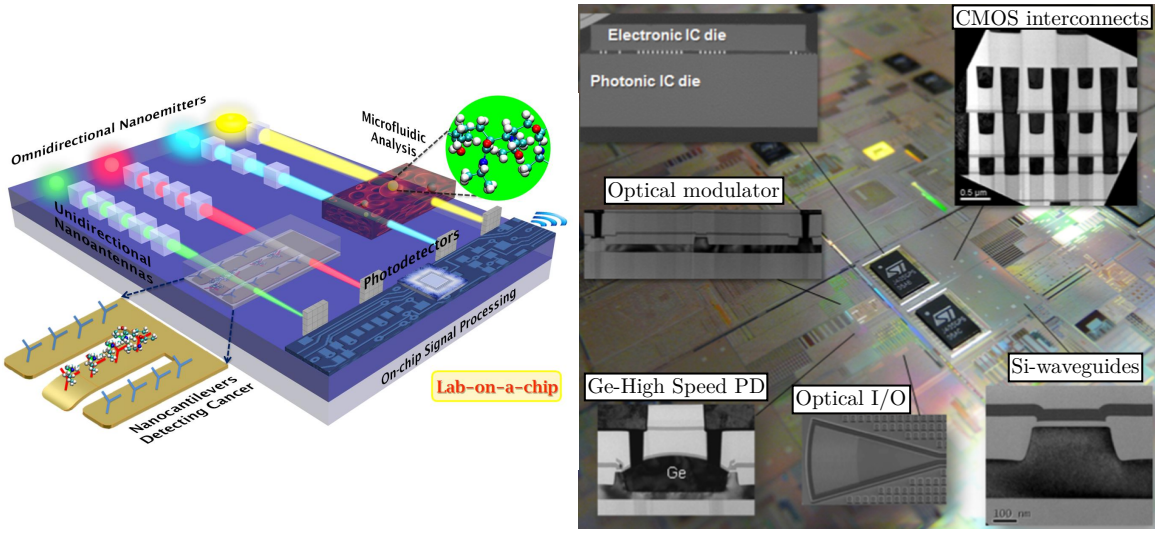

(a) (b)

Figure 1.3 Examples of PICs in applications. (a) Schematic of a lab-on-a-chip device containing sources, samples, sensors and detectors on a single wafer (taken from [46]). (b) Proposed hybrid platform for communications combining IO and IC components on a single wafer (taken from [47].

fabrication (i.e. a single fabrication run), miniaturisation of complete devices and reduced coupling losses between elements. In PICs, the connections between the various elements of the circuit/device are made with waveguides (the photonic wire to the ICs electric wire); one technology taking advantage of PICs has been biosensing.

The non-invasive and generally non-destructive nature of light matter interactions makes it well suited to biosensing [37, 38]. The transmission of light through a waveguide is sensitive to refractive index changes along the waveguide; attaching 'receptors' (which bind to certain biomolecules) to the waveguide and tracking the transmission, the biomolecules can be 'sensed'. The ability to do this on a small chip which can have other functions added is clearly valuable. Other sensing applications—such as nanoparticle sensing, where the resonance of an optical cavity is tuned or perturbed by nearby particles—have also been demonstrated in IO [39–42]. A step beyond sensing, complete lab-on-a-chip devices [43–45] which contain all the functionalities (sample preparation, signal delivery, sensing, etc.) on a single chip have been developed. As well as the capabilities of miniaturisation and mass production, a lab-on-a-chip device benefits from the high sensitivity of optical elements. A schematic of a lab-on-a-chip device is shown in figure 1.3(a). The chip contains a number of light sources used for cantilever sensing and microfluidic analysis. The schematic suggests that photodetectors would be used and signals would be processed electronically.

One of the other big technologies driving developments in PICs is telecommunications, where demand for ever increasing bandwidth/data rates can benefit greatly from the multiplexing capabilites of waveguides. Multiplexing is the ability of a single waveguide to carry numerous signals over different *channels*, utilising the discrete states of light travelling in

the waveguide [48]. A further benefit of IO circuits is the absence of Joule heating in optical elements and lower loss and lower dispersion at high data rates [49]. Light has been used to send signals over long distances through optical fibres for decades and now bringing optical interconnections from the well established long-haul regime down to chip scale connections is expected to help datacentres cope with the rising data rates [50–53]. Many optical components have already been demonstrated in a planar format: wavelength division (de)multiplexers [54–56], polarisation rotators and splitters [57–60], modulators [61, 62] and many others [63–65]. An example of a PIC implemented alongside an electronic device for use in telecommunications is shown in figure 1.3(b). Images of some of the elements comprising the circuit, such as input and output (I/O) grating couplers and germanium photodetectors (Ge PD) are marked. With the improvements in PICs, hybrid integrated structures, containing both electronic and photonic components, might replace electronic ones in the future.

1.2.1 Characterising dielectric waveguides

Experimentally characterising planar waveguides is clearly of importance to the applications above. Measuring the film thickness and refractive index can be done with ellipsometry and interferometry but to determine the waveguiding characteristics, other techniques have been developed [66–69]. Knowing the waveguide propagation losses would be a requirement for telecommunications and they are often found by measuring the power before coupling and after coupling out of waveguides of varying length; the measured difference in power includes losses from coupling light into and out of the waveguide but varying length means these losses can be separated from the propagation losses [70–72]. Another way of determining propagation loss is by measuring the scattering from the surface of the waveguide (either by imaging the scattered light or by scanning a detector along the waveguide). This scattering is caused by surface roughness which can be assumed to be uniformly random along the waveguide thus the decrease in scattered intensity can be related to the propagation loss [73–75]. These methods do not distinguish between modes and will measure the overall propagation loss whether there is a single mode or multiple modes propagating.

One of the more wide-ranging methods of waveguide characterisation is prism coupling which can identify multi-mode propagation [76]. The prism coupling method works by bringing a prism into close contact with the waveguide and evanescently coupling light through the prism into the waveguide but the coupling is sensitive to the separation of the prism and the waveguide [77]. Index matching fluid is often used to achieve this close contact; a screw pushing the waveguide into the prism can also be used and provides for some adjustment of the separation. Prism coupling is a momentum matching technique meaning that the wavenumber in the prism has to match the wavenumber of the mode [71]; to achieve this the incident angle is varied (a set-up for prism coupling is shown in figure 1.4(a)). The requirement of momentum matching means that prism coupling is mode specific, i.e., individual modes are coupled at different angles. This allows measurements

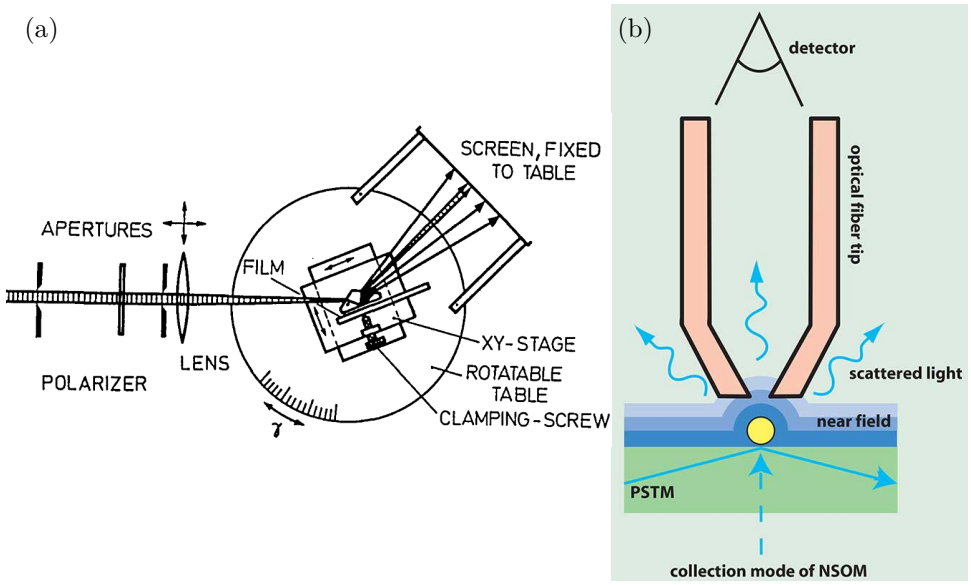

Figure 1.4 Different measurement techniques for dielectric waveguides. (a) Experimental set-up for prism coupling, the out-coupled modes are marked by the arrows; the angles can be related to the modes' effective indexes (taken from [76]). (b) Simplified schematic of the operation of NSOM showing that the near-field is collected (taken from [84]).

of the loss of the individual modes as well as the effective index of the individual modes [78–80]. Measurement methods based on far-field imaging have also been used to determine refractive index profiles and mode propagation in waveguides [81–83].

Near-field optical measurements can map electric fields with sub-diffraction limited resolution. This can be done with photon scanning tunneling microscopy (PSTM) and near-field scanning optical microscopy (NSOM) [85, 86]. These methods work by bringing a sharp probe close to the sample surface, allowing the evanescent optical waves to tunnel or couple to the probe. A schematic of a NSOM probe is shown in figure 1.4(b). Capturing the evanescent waves means that a larger range of spatial frequencies is acquired and thus the resolution is improved beyond that of far-field optical microscopy, with resolutions of ~100 nm achievable [87]. In PICs, detection of the near-field has proved very useful as waveguide modes can be mapped out with fine resolution. As well as measuring the effective refractive index of a waveguide mode, PSTM and NSOM have been used in studying single mode propagation in waveguides, scattering of modes in waveguides, propagation around bends and other characteristics [88–92].

1.2.2 Silicon Nitride

An emerging material for planar photonics when working in the visible and near infrared region of the spectrum is silicon nitride (Si_3N_4) which has also been used as the waveguide in HAMR designs [10, 93]. Si_3N_4 has long been used in the semiconductor industry as a passivation layer and so its mechanical properties are well known and suitable growth

processes are well established. It is compatible with the CMOS fabrication processes used in the semiconductor industry and films a few hundred nanometres thick of optical quality and with low stress (i.e. low likelihood to fracture) can be deposited by low pressure chemical vapour deposition (CVD) or plasma enhanced CVD. This has led to considerable integrated optics research into Si_3N_4 and its optical properties are also very conducive to work in the visible range; its band gap is ~4.5 eV so it is transparent to visible frequencies of light (with negligible two photon absorption at 532 nm), no free carrier absorption [94], relatively high refractive index ($n_{Si_3N_4} \approx 2.1$ over the visible spectrum) and nonlinearity of refractive index ($2.4 \times 10^{-19}\,m^2\,W^{-1}$) [95] and a low thermo-optical coefficient [96]. These properties have led to the demonstration of many important integrated optical elements in Si_3N_4 platforms such as complete multi-layer integrated optics circuits [97–99], on-chip lasers [100] multi-mode interference couplers [101], spectrometers [102, 103] and many others [104–108].

Si_3N_4 waveguides fabricated by different growth processes have demonstrated low loss propagation for light of visible to the near infrared frequencies (~500 nm to 1550 nm) [72, 109, 110]. At 1550 nm, losses as low as $3\,dB\,m^{-1}$ were measured for a waveguide with a Si_3N_4 core (the method for this measurement incurred bending losses and, by reducing the curvature, losses as low as $0.1\,dB\,m^{-1}$ were predicted) and in the visible range, propagation losses as low as $\sim 10\,dB\,m^{-1}$ have been achieved [111]. While the extremely low-loss capabilities may not be required for light propagation across only a few millimetres it is certainly beneficial. Low propagation losses allow for high-Q resonators [112–114], with quality factors above 10^7. These high quality factors for structures which have micrometre or sub-micrometre cross sectional area allow high intensities to propagate over long distances for relatively low input power. Being able to maintain high intensities over long interaction lengths means that the nonlinearity of Si_3N_4 can be exploited; nonlinear effects such as harmonic generation [115, 116], frequency comb generation [117, 118] and supercontinuum generation [119–121] have been performed using ring resonators in Si_3N_4. An example of these processes is shown in figure 1.5.

The bright rings in figure 1.5(a) and (b) are formed by light scattered from a silicon nitride ring resonator. The scattered light consists of the pump beam (which had a wavelength of 1554 nm) as well as the second harmonic, (a), and third harmonic, (b). Harmonic generation was achieved with input pump powers of 3 mW and the waveguide had dimensions of 725 nm × 1500 nm while the radius of the ring resonator was 116 µm. The frequency comb spectrum shown in figure 1.5(c) was generated using a similar resonator (waveguide dimensions 725 nm × 1650 nm and ring radius 100 µm) though in this case the pump power was ~1–2 W.

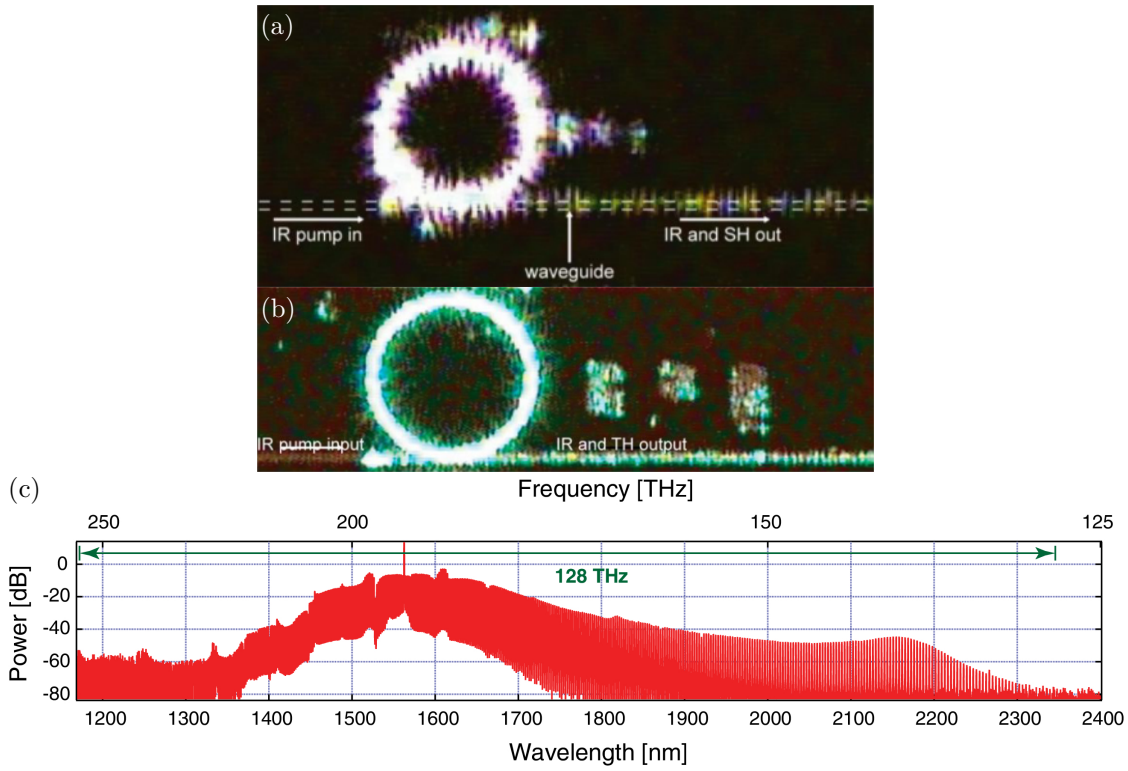

Figure 1.5 Harmonic generation in silicon nitride ring resonators. (a) Second harmonic generation of a 1550 nm pump beam in a ring resonator with radius 116 µm. (b) Third harmonic generation with the same pump and ring resonator. (c) Frequency spectrum produced by a similar ring resonator for a pump wavelength of 1562 nm. Images taken from [115, 117].

1.3 Overview of the thesis

In this thesis, the microdisk and another focusing element (based on light scattering by an array of sub-micron structures) are studied as integrated optical structures through simulation and experiment. The motivation for this work was to design a dielectric coupling element for use in a HAMR write head. With this application in mind and, every attempt was made to work within the fabrication limitations of UV lithography. Although the structures presented here were fabricated using electron beam lithography and focused ion beam milling, large-scale processing would need to be used for commercial viability. To test the viability of the coupling elements for HAMR, the elements were fabricated alongside and illuminated from planar dielectric waveguides. Dielectric waveguides, being the medium between light source and focusing element, play a significant role in the process. For most applications using light focusing, it is desirable to use only a single mode of the waveguide, however, the structures generally support more than a single mode. In consideration of this, the propagation of light in these waveguides was investigated experimentally and a method of characterising planar dielectric waveguides was developed.

Although HAMR was the targeted application for this work, the structures studied

here also lend themselves to sensing and optical manipulation which take advantage of the electromagnetic field distributions created in optical waveguides and focusing elements and in which our group has previously been involved [122–125].

This thesis is laid out as follows

- In chapter 2, the materials and the basic geometries used for the different structures are introduced. The groundwork for the theoretical methods used to study these structures—waveguides, microdisks, holes in waveguides—is covered and a brief description of the software used for simulations is given. One of the limitations of the measurement set-up is also covered and demonstrated as a factor in the disparity between theoretical simulations and experimental results.

- In chapter 3, the propagation of light in multimode dielectric slab waveguides is investigated. A description of the measurement set-up and methods used for all of the experimental chapters is given. The mode beating (the interference of the propagating modes) is found to create an intensity profile that is constant in time, thus affecting the power radiated from the end-face of the waveguide depending on where it is terminated. (Some of the work presented in this chapter has been published.)

- In chapter 4, the measurement technique set out in chapter 3 is extended to rectangular waveguides. Through experimental intensity maps, the perturbation of the propagating modes by different integrated optical elements (bends and tapers) is examined.

- In chapter 5, the first of the integrated focusing elements is presented. A microdisk positioned at the end of a waveguide and illuminated by the light radiated from the waveguide is presented. The deviation of the light scattering from the idealised case to the experimental setting is described. The influence of the disk diameter on the focal spot size and light gathering efficiency is demonstrated through simulation and experiment.

- In chapter 6, a focusing element which is contained within the waveguide core is studied. Holes milled/etched through the core layer scatter an incident mode; through deliberate placement of the holes, a focus is produced by the interference of their individual scattering. Again, the focusing capabilities are simulated and compared to experimental measurements.

- In chapter 7, some conclusions on the work as a whole are given and some of the directions in which the work could proceed are laid out.

2 Light in dielectric structures

Light propagating in dielectric media is subject to diffraction, reflection and refraction. Using these processes, light can be focused to a spot, confined as it propagates and redirected. In this chapter, the starting structure for the experiments in later chapters is described and the analytical and numerical methods used to analyse the structures are introduced. The properties (wavenumber, field profile) of light propagating in a slab waveguide can be found by analytical methods. Moving to rectangular waveguides, analytical methods give suitable results only for cases where light is well confined to the core. Similarly for light scattering, there are analytical solutions for "low dimensional" cases but numerical/computational methods must be used to simulate a full 3D structure.

2.1 Analytical Methods

2.1.1 Waveguides

A slab waveguide is a structure which confines light in one dimension and allows it to propagate along another. (Along the third dimension, there is no confinement and the fields do not vary with position.) Confining in this sense means that the beam width remains constant so that at any two positions along the waveguide, the profiles of the electromagnetic fields are identical (after accounting for the phase difference). A typical slab waveguide consists of layers of different materials each having a different refractive index; the simplest case is a high index, middle layer (referred to as the core) sandwiched between two semi-infinite layers of lower index (the cladding/superstrate/substrate). Confinement of light to the core layer is achieved by total internal reflection at the interfaces between the core and the cladding. (Although the field is considered confined to the core, there is a portion of it in the cladding layers.) In the ideal case, this geometry allows light to travel larger distances without as great a drop in intensity compared to free space propagation—the decrease is $\propto 1/r$ rather than $1/r^2$, since there is no divergence along the confined dimension. For waveguides consisting of dielectric materials, propagation loss should only arise from

scattering (from, e.g., surface roughness or fabrication defects) or absorption and is usually very small—silicon nitride waveguides similar to those used here have been shown to have propagation losses of $<0.5\,\mathrm{dB\,cm^{-1}}$ in the visible light range [111, 126]. The general material layer structure used in the experimental work for this thesis is shown in figure 2.1.

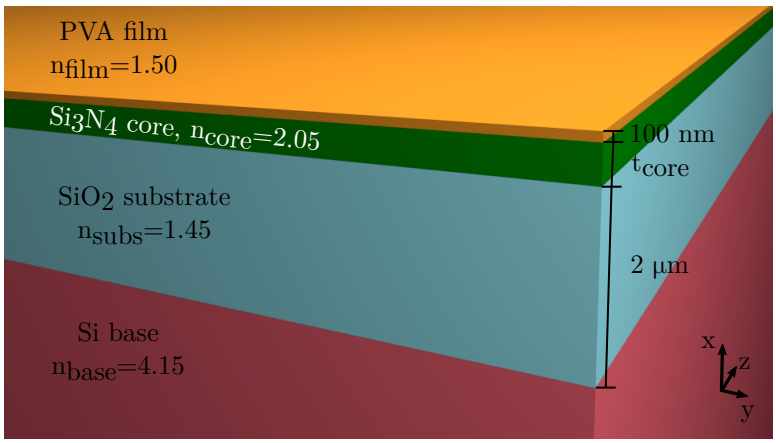

Figure 2.1 The material layers for the experiments discussed in this thesis. Three different thicknesses of Si_3N_4 are used—180 nm, 284 nm and 400 nm. Refractive indexes are given at $\lambda_0 = 532$ nm. The coordinate system is also shown, with z the propagation direction.

The starting material consisted of a base wafer of silicon (Si, refractive index $n_{base} = 4.15$) on which 2 µm of thermal oxide (SiO_2, $n_{subs} = 1.45$) was grown and then a layer of silicon nitride (Si_3N_4, n_{core} 2.05) deposited by low pressure chemical vapour deposition (LPCVD). (The refractive indexes stated are for the wavelength $\lambda_0 = 532$ nm used in experiment; this wavelength was chosen as it lies in the visible range and compact laser diodes are available at this wavelength.) These wafers were obtained from Si-Mat Silicon Materials. Three different thicknesses (t_{core}) of Si_3N_4 were used for the work in this thesis: 180 nm, 284 nm and 400 nm. For certain experiments, a film of poly-vinyl acetate (PVA) doped with the fluorescent dye rhodamine B (RhB) was spin-coated onto the Si_3N_4 layer. From ellipsometric measurements, this film had an average thickness of $100\,\mathrm{nm} \pm 8\,\mathrm{nm}$ and a refractive index of 1.50. As a slab waveguide, the width (in the y direction as shown, z is the direction of propagation) of each layer is considered infinite (the samples are typically 10 mm wide). The thickness of the SiO_2 layer is large enough that in most cases the fields decay to negligible strength before reaching the Si layer and the SiO_2 can be approximated as semi-infinite. For cases where the fields are more weakly confined to the core, the Si needs to be included in the analysis. The effect of varying core thickness and the reasons for using fluorescent dye are discussed later.

In this arrangement, the Si_3N_4 layer is the core of the waveguide and light coupled into the layer will undergo total internal reflection at the Si_3N_4 surfaces for any angle greater $\theta_c \simeq 50°$. However, even though total internal reflection occurs for a continuum of angles greater than this critical angle, light in a waveguide propagates in discrete modes

corresponding to specific reflection angles. The discrete nature of the modes arises from requirements of the phase of the rays in the propagating wave, i.e, separate rays on the same phase front need to maintain zero (or multiple of 2π) phase difference—a clearer description of this is given in [127]. Modes are defined by their order (for a slab this is the number of nodes in the electric field across the waveguide) and polarisation and are classified as transverse electric polarised (TE_m) or transverse magnetic polarised (TM_m) with $m = 0, 1, 2\ldots$ the order of the mode. TE modes are polarised such that the electric field has a component only along planes parallel to the interfaces of the materials (the y axis in figure 2.1) while TM modes have their magnetic fields (H-fields) in along these planes. Each mode has an effective refractive index (related to its angle of reflection by $n_{\mathrm{eff}} = n_{\mathrm{core}} \sin\theta_m$) which lies between the refractive index of the core and that of its surroundings. For our structure, the effective indexes of the modes will lie in the range 1.45–2.05. Each mode also has its own electromagnetic field distribution and the method for calculating these distributions and the effective indexes is outlined in the following section. The steps which are worked through explicitly below are also the basis for the other theoretical methods covered in this chapter (and electromagnetism generally) i.e. starting with Maxwell's equations and applying the appropriate interface and boundary conditions. For the later sections, these steps are not written out explicitly.

Dispersion relation

The dispersion relation of a waveguide describes how the wavenumber of light propagating in the waveguide varies with the frequency. These dispersion curves and the field distributions of the modes of a waveguide are calculated by solving the eigenvalue equations (which are versions of the wave equation) which is found as follows. Beginning with the Maxwell curl equations

$$\vec{\nabla} \times \vec{E} = -\mu \frac{\partial \vec{H}}{\partial t} \qquad \vec{\nabla} \times \vec{H} = \varepsilon \frac{\partial \vec{E}}{\partial t}$$

and defining a wave propagating in the z direction (the x and y components, for now, are left undefined)

$$\vec{E} = \vec{E}_0(x, y) \exp\left[\mathrm{i}(\beta z - \omega t)\right] \qquad \vec{H} = \vec{H}_0(x, y) \exp\left[\mathrm{i}(\beta z - \omega t)\right]$$

where the propagation constant $\beta = n_{\mathrm{eff}} k_0$, expressions for the x, y and z components of the fields are found

$$\frac{\partial E_z}{\partial y} - \mathrm{i}\beta E_y = \mathrm{i}\omega\mu H_x \qquad \frac{\partial H_z}{\partial y} - \mathrm{i}\beta H_y = -\mathrm{i}\omega\varepsilon E_x$$

$$\mathrm{i}\beta E_x - \frac{\partial E_z}{\partial x} = \mathrm{i}\omega\mu H_y \qquad \mathrm{i}\beta H_x - \frac{\partial H_z}{\partial x} = -\mathrm{i}\omega\varepsilon E_y$$

$$\frac{\partial E_y}{\partial x} - \frac{\partial E_x}{\partial y} = \mathrm{i}\omega\mu H_z \qquad \frac{\partial H_y}{\partial x} - \frac{\partial H_x}{\partial y} = -\mathrm{i}\omega\varepsilon E_z.$$

As the width of the slab is effectively infinite (y direction) it can be approximated that there is no variation of the fields along y so $^{\partial}/_{\partial y} = 0$. Applying this to the equations above, two separate cases present themselves. The first has its electric field only along the y direction (this is the transverse electric, TE, polarisation mentioned earlier) and the second has its magnetic (H) field only along the y direction and is termed transverse magnetic (TM). Gathering and substituting so that there are two equations in terms of only E_y and H_y, the wave equation is arrived at.

$$\mathrm{i}\beta\left(-\frac{\beta}{\omega\mu}E_y\right) - \frac{\partial}{\partial x}\left[\frac{-\mathrm{i}}{\omega\mu}\frac{\partial E_y}{\partial x}\right] = -\mathrm{i}\omega\varepsilon E_y \qquad \mathrm{i}\beta\left(\frac{\beta}{\omega\varepsilon}H_y\right) - \frac{\partial}{\partial x}\left[\frac{\mathrm{i}}{\omega\varepsilon}\frac{\partial H_y}{\partial x}\right] = \mathrm{i}\omega\mu H_y$$

$$\frac{1}{\omega\mu}\frac{\partial^2 E_y}{\partial x^2} - \left(\frac{\beta^2}{\omega\mu} - \omega\varepsilon\right)E_y = 0 \qquad \frac{1}{\omega\varepsilon}\frac{\partial^2 H_y}{\partial x^2} - \left(\frac{\beta^2}{\omega\varepsilon} - \omega\mu\right)H_y = 0$$

$$\frac{\partial^2 E_y}{\partial x^2} + \left(\omega^2\mu\varepsilon - \beta^2\right)E_y = 0 \qquad \frac{\partial^2 H_y}{\partial x^2} + \left(\omega^2\mu\varepsilon - \beta^2\right)H_y = 0.$$

The wave equation has the general solution

$$E_y = C^+ \exp[\mathrm{i}\kappa x] + C^- \exp[-\mathrm{i}\kappa x],$$

where $\kappa = \sqrt{\omega^2\mu\varepsilon - \beta^2}$. This solution is a superposition of waves propagating in the positive and negative x direction. As ε is different for each layer of the waveguide, κ is different for each layer and the electric field is expressed as a piecewise continuous function. To apply some physical constraints to the solutions, we restrict κ such that the waves can propagate within the core but decay outside it. In other words, κ is real within the core and imaginary in the other layers. The solutions are also set to be outward travelling waves, decaying towards zero as they move away from the core. Having imposed these conditions, the electric field for a TE mode in the slab waveguide described earlier can be written as

$$E_y = \begin{cases} \hat{E}_\mathrm{a}\exp(-\kappa_\mathrm{a}x) & \text{for } x > t_\mathrm{f} + \frac{t_\mathrm{c}}{2} \\ \hat{E}_\mathrm{f}^+\exp(-\kappa_\mathrm{f}x) + \hat{E}_\mathrm{f}^-\exp(\kappa_\mathrm{f}x) & \text{for } \frac{t_\mathrm{c}}{2} < x < t_\mathrm{f} + \frac{t_\mathrm{c}}{2} \\ \hat{E}_\mathrm{c}^+\exp(\mathrm{i}\kappa_\mathrm{c}x) + \hat{E}_\mathrm{c}^-\exp(-\mathrm{i}\kappa_\mathrm{c}x) & \text{for } \frac{-t_\mathrm{c}}{2} < x < \frac{t_\mathrm{c}}{2} \\ \hat{E}_\mathrm{s}\exp(\kappa_\mathrm{s}x) & \text{for } x < \frac{-t_\mathrm{c}}{2} \end{cases} \tag{2.1}$$

where the subscripts represent the air, film, core and substrate and $t_{\mathrm{c,f}}$ is the thickness of the core and the film, respectively, with the core centred on $x = 0$. (For the modes of the slab waveguides used in this thesis, the thickness of the SiO_2 substrate is large enough that the field has decayed to a sufficiently small value before it reaches the bottom and so it is treated as a semi-infinite layer.) To find the dispersion relation, the conditions of continuous $E_\parallel$ and continuous $H_\parallel$ across interfaces are applied. (For a TE mode, $E_\parallel = E_y$ and $H_\parallel = H_z = \frac{-i}{\omega\mu}\frac{\partial E_y}{\partial x}$.) The steps for finding the dispersion relation are, briefly, as follows.

At the bottommost interface ($x = {}^{-t_c}/_2$) we have

$$\hat{E}_\mathrm{s} \exp\left(\frac{-\kappa_\mathrm{s} t_\mathrm{c}}{2}\right) = \hat{E}_\mathrm{c}^+ \exp\left(\frac{-\mathrm{i}\kappa_\mathrm{c} t_\mathrm{c}}{2}\right) + \hat{E}_\mathrm{c}^- \exp\left(\frac{\mathrm{i}\kappa_\mathrm{c} t_\mathrm{c}}{2}\right)$$

and

$$\kappa_\mathrm{s}\hat{E}_\mathrm{s} \exp\left(\frac{-\kappa_\mathrm{s} t_\mathrm{c}}{2}\right) = \mathrm{i}\kappa_\mathrm{c}\left[\hat{E}_\mathrm{c}^+ \exp\left(\frac{-\mathrm{i}\kappa_\mathrm{c} t_\mathrm{c}}{2}\right) - \hat{E}_\mathrm{c}^- \exp\left(\frac{\mathrm{i}\kappa_\mathrm{c} t_\mathrm{c}}{2}\right)\right]$$

from the interface conditions. By substitution,

$$\begin{aligned}
\kappa_\mathrm{s}\left[\hat{E}_\mathrm{c}^+ \exp\left(\frac{-\mathrm{i}\kappa_\mathrm{c} t_\mathrm{c}}{2}\right) + \hat{E}_\mathrm{c}^- \exp\left(\frac{\mathrm{i}\kappa_\mathrm{c} t_\mathrm{c}}{2}\right)\right] &= \kappa_\mathrm{c}\left[\hat{E}_\mathrm{c}^+ \exp\left(\frac{-\mathrm{i}\kappa_\mathrm{c} t_\mathrm{c}}{2}\right) - \hat{E}_\mathrm{c}^- \exp\left(\frac{\mathrm{i}\kappa_\mathrm{c} t_\mathrm{c}}{2}\right)\right] \\
(\kappa_\mathrm{s} + \mathrm{i}\kappa_\mathrm{c})\hat{E}_\mathrm{c}^- \exp\left(\frac{\mathrm{i}\kappa_\mathrm{c} t_\mathrm{c}}{2}\right) &= (\mathrm{i}\kappa_\mathrm{c} - \kappa_\mathrm{s})\hat{E}_\mathrm{c}^+ \exp\left(\frac{-\mathrm{i}\kappa_\mathrm{c} t_\mathrm{c}}{2}\right) \\
\hat{E}_\mathrm{c}^- &= \frac{(\mathrm{i}\kappa_\mathrm{c} - \kappa_\mathrm{s})}{(\mathrm{i}\kappa_\mathrm{c} + \kappa_\mathrm{s})}\hat{E}_\mathrm{c}^+ \exp(-\mathrm{i}\kappa_\mathrm{c} t_\mathrm{c}) \\
\hat{E}_\mathrm{c}^- &= \hat{E}_\mathrm{c}^+ \exp\left[-\mathrm{i}(\kappa_\mathrm{c} t_\mathrm{c} - 2\varphi_\mathrm{s})\right],
\end{aligned}$$

using $\varphi_\mathrm{s} = \arctan\left({}^{\kappa_\mathrm{s}}/_{\kappa_\mathrm{c}}\right)$. The field in the core can then be written as

$$E_\mathrm{y}|_{|x|\le t_c/2} = \hat{E}_\mathrm{c}^+ \exp(\mathrm{i}\kappa_\mathrm{c} x) + \hat{E}_\mathrm{c}^+ \exp\left[-\mathrm{i}(\kappa_\mathrm{c} t_\mathrm{c} - 2\varphi_\mathrm{s})\right] \exp(-\mathrm{i}\kappa_\mathrm{c} x).$$

The field in the substrate is then found as

$$\begin{aligned}
E_\mathrm{y}|_{|x|\le t_c/2} &= \hat{E}_\mathrm{s} \exp\left(\kappa_\mathrm{s} x\right) \\
&= \left[\hat{E}_\mathrm{c}^+ \exp\left(\frac{-\mathrm{i}\kappa_\mathrm{c} t_\mathrm{c}}{2}\right) + \hat{E}_\mathrm{c}^- \exp\left(\frac{\mathrm{i}\kappa_\mathrm{c} t_\mathrm{c}}{2}\right)\right] \exp\left(\frac{\kappa_\mathrm{s} t_\mathrm{c}}{2}\right) \exp\left(\kappa_\mathrm{s} x\right) \\
&= \hat{E}_\mathrm{c}^+ \left[\exp\left(\frac{-\mathrm{i}\kappa_\mathrm{c} t_\mathrm{c}}{2}\right) + \exp\left(-\mathrm{i}\left(\frac{\kappa_\mathrm{c} t_\mathrm{c}}{2} - 2\varphi_\mathrm{s}\right)\right)\right] \exp\left(\kappa_\mathrm{s}(x + {}^{t_c}/_2)\right) \\
&= \hat{E}_\mathrm{c}^+ \exp\Big(-\mathrm{i}(\kappa_\mathrm{c} t_\mathrm{c}/2 - \varphi_\mathrm{s})\Big)\Big[\exp\left(-\mathrm{i}\varphi_s\right) + \exp\left(\mathrm{i}\varphi_s\right)\Big] \exp\Big(\kappa_\mathrm{s}(x + {}^{t_c}/_2)\Big) \\
&= 2\hat{E}_\mathrm{c}^+ \exp\Big(-\mathrm{i}(\kappa_\mathrm{c} t_\mathrm{c}/2 - \varphi_\mathrm{s})\Big) \cos\left(\varphi_s\right) \exp\Big(\kappa_\mathrm{s}(x + {}^{t_c}/_2)\Big).
\end{aligned}$$

The field in the other layers is found similarly in terms of the single unknown $\hat{E}_\mathrm{c}^+$. Doing this, a second expression is found for the field in the core

$$\hat{E}_\mathrm{c}^+ \exp(\mathrm{i}\kappa_\mathrm{c} x) + \hat{E}_\mathrm{c}^+ \exp\left[\mathrm{i}(\kappa_\mathrm{c} t_\mathrm{c} - 2\varphi_\mathrm{f})\right] \exp(-\mathrm{i}\kappa_\mathrm{c} x).$$

For this field to really exist, the two solutions must be identical.

$$\hat{E}_\mathrm{c}^+ \exp(\mathrm{i}\kappa_\mathrm{c} x) + \hat{E}_\mathrm{c}^+ \exp\left[-\mathrm{i}(\kappa_\mathrm{c} t_\mathrm{c} - 2\varphi_\mathrm{s})\right] \exp(-\mathrm{i}\kappa_\mathrm{c} x) =$$

$$\hat{E}_{\mathrm{c}}^{+}\exp(\mathrm{i}\kappa_{\mathrm{c}}x)+\hat{E}_{\mathrm{c}}^{+}\exp\left[\mathrm{i}(\kappa_{\mathrm{c}}t_{\mathrm{c}}-2\varphi_{\mathrm{f}})\right]\exp(-\mathrm{i}\kappa_{\mathrm{c}}x)$$

$$\begin{aligned}
&\exp\left[-\mathrm{i}(\kappa_{\mathrm{c}}t_{\mathrm{c}}-2\varphi_{\mathrm{s}})\right]=\exp\left[\mathrm{i}(\kappa_{\mathrm{c}}t_{\mathrm{c}}-2\varphi_{\mathrm{f}})\right]\\
&-(\kappa_{\mathrm{c}}t_{\mathrm{c}}-2\varphi_{\mathrm{s}})+2m\pi=(\kappa_{\mathrm{c}}t_{\mathrm{c}}-2\varphi_{\mathrm{f}})\\
&\kappa_{\mathrm{c}}t_{\mathrm{c}}-(\varphi_{\mathrm{f}}+\varphi_{s}+m\pi)=0,
\end{aligned}\tag{2.2}$$

where m is an integer and is termed the order of the mode, $\varphi_{\mathrm{f}}=\arctan\left(\frac{\kappa_{\mathrm{f}}}{\kappa_{\mathrm{c}}}A\right)$ and $A=(\kappa_{\mathrm{f}}\tanh(\kappa_{\mathrm{f}}t_{\mathrm{f}})+\kappa_{\mathrm{a}})/(\kappa_{\mathrm{f}}+\kappa_{\mathrm{a}}\tanh(\kappa_{\mathrm{f}}t_{\mathrm{f}}))$. The dispersion relation for any four layered waveguide is given by equation (2.2). Substituting in the appropriate values for thicknesses and refractive indexes returns the wavenumber for a given frequency. Although equation (2.2) is an analytical solution, it contains linear and trigonometric functions of κ so it must be solved graphically or numerically. To find the values of κ (and thereby β and n_{eff}) for which equation (2.2) is satisfied, the SciPy library of the programming language *Python* was used (specifically *fsolve* from the *optimize* module) [128]. Dispersion curves (where the core thickness is varied instead of the frequency) for the material layers used in experiment are shown below (figure 2.2). It can be seen that increasing the core thickness t_{c} while keeping everything else constant causes the wavenumber to increase and increases the number of modes supported by the waveguide. It is this effect which is studied later, in chapter 3. The steps above were for the TE modes, similar analysis for TM modes returns the same characteristic equation (2.2) but with

$$\varphi_{\mathrm{s}}=\arctan\left(\frac{\kappa_{\mathrm{s}}}{\kappa_{\mathrm{c}}}\left(\frac{n_{\mathrm{c}}}{n_{\mathrm{s}}}\right)^{2}\right),$$

$$\varphi_{\mathrm{f}}=\arctan\left(\frac{\kappa_{\mathrm{f}}}{\kappa_{\mathrm{c}}}\left(\frac{n_{\mathrm{c}}}{n_{\mathrm{f}}}\right)^{2}A\right)$$

and

$$A=\frac{(\frac{n_{\mathrm{a}}}{n_{\mathrm{f}}})^{2}\kappa_{\mathrm{f}}\tanh(\kappa_{\mathrm{f}}t_{\mathrm{f}})+\kappa_{\mathrm{a}}}{(\frac{n_{\mathrm{a}}}{n_{\mathrm{f}}})^{2}\kappa_{\mathrm{f}}+\kappa_{\mathrm{a}}\tanh(\kappa_{\mathrm{f}}t_{\mathrm{f}})}.$$

The additional factors of $(n_i/n_j)^2$ for the TM modes arise as $E_{\parallel}=E_z\propto\frac{1}{n^2}\frac{\partial H_y}{\partial x}$. The transverse fields for TE (E_y) and TM (H_y) modes then have profiles given by

$$E_y=\begin{cases}
E_0\,\alpha_0^{-1}\cos(\kappa_{\mathrm{c}}t_{\mathrm{c}}-\varphi_{\mathrm{s}})\exp(-\kappa_{\mathrm{a}}(x-t'_{\mathrm{f}}))\\
E_0\,\alpha_0^{-1}\,\alpha(x)\cos(\kappa_{\mathrm{c}}t_{\mathrm{c}}-\varphi_{\mathrm{s}})\\
E_0\cos(\kappa_{\mathrm{c}}(x+t_{\mathrm{c}}/2)-\varphi_{\mathrm{s}})\\
E_0\cos(\varphi_{\mathrm{s}})\exp(\kappa_{\mathrm{s}}(x+t_{\mathrm{c}}/2))
\end{cases}\tag{2.3a}$$

and

$$H_y = \begin{cases} H_0\,\gamma_0^{-1}\cos(\kappa_c t_c - \varphi_s)\exp(-\kappa_a(x - t_f')) \\ H_0\,\gamma_0^{-1}\,\gamma(x)\cos(\kappa_c t_c - \varphi_s) \\ H_0\cos(\kappa_c(x + {}^{t_c}/_2) - \varphi_s) \\ H_0\cos(\varphi_s)\exp(\kappa_s(x + {}^{t_c}/_2)) \end{cases} \tag{2.3b}$$

where $t_f' = t_f + {}^{t_c}/_2$,

$$\begin{aligned} E_0 &= 2\hat{E}_c^+\exp(-i\kappa_c t_c/2 - \varphi_s) \\ H_0 &= 2\hat{H}_c^+\exp(-i\kappa_c t_c/2 - \varphi_s) \\ \alpha(x) &= \cosh(\kappa_f(x - t_f')) - \frac{\kappa_a}{\kappa_f}\sinh(\kappa_f(x - t_f')), \\ \gamma(x) &= \cosh(\kappa_f(x - t_f')) - \left(\frac{n_f}{n_a}\right)^2\frac{\kappa_a}{\kappa_f}\sinh(\kappa_f(x - t_f')) \end{aligned}$$

and $\alpha_0 = \alpha({}^{t_c}/_2)$, $\gamma_0 = \gamma({}^{t_c}/_2)$. Since $\hat{E}_c^+$ and $\hat{H}_c^+$ are just field amplitudes, they can be set equal to 1 in a theoretical analysis. In the experiments discussed in this thesis a single wavelength is used ($\lambda_0 = 532\,\text{nm}$) but the thickness is varied so rather than plot the regular dispersion curves, the variation of wavenumber with thickness is plotted for the modes. These plots are shown in figure 2.2 for the three lowest order TE and TM modes of the waveguide along with the electric field profiles for the TE_0 and TM_0 modes (when $t_{core} = 180\,\text{nm}$).

The plot in figure 2.2(a) shows how the modes' effective indexes vary with the thickness of the core at constant frequency ($f = {}^{c}/_{532\,\text{nm}}$). Each solid line is a different mode of the waveguide and at a given thickness a lower order mode has a higher effective refractive index. It can be seen that a mode's n_{eff} increases with the core thickness. It can also be seen that at a certain thickness n_{eff} decreases to the refractive index of the substrate (1.45) at which point it is no longer a guided mode and is "cut off". The dotted vertical lines mark the core thicknesses used in the experimental work in this thesis. At each thickness a different number of modes are supported; the thinnest core (180 nm) supports only the fundamental TE and TM modes (TE_0 and TM_0). This thickness is used in chapters 5 and 6 for focusing elements. The middle thickness (284 nm) supports two TE and two TM modes and the thickest core (400 nm) supports three TE and two TM modes. These core thicknesses are used in chapter 3 where the interference of multiple modes propagating simultaneously in a single waveguide is studied.

Figure 2.2(b) shows the electric field distribution across the waveguide (the x direction in figure 2.1) for the TE_0 and TM_0 modes of the 180 nm thick core waveguide. (For TE_0 this is E_y while the TM_0 is E_x.) These are the modes used for illuminating the focusing elements in chapters 5 and 6. The fundamental modes of the other core thicknesses have

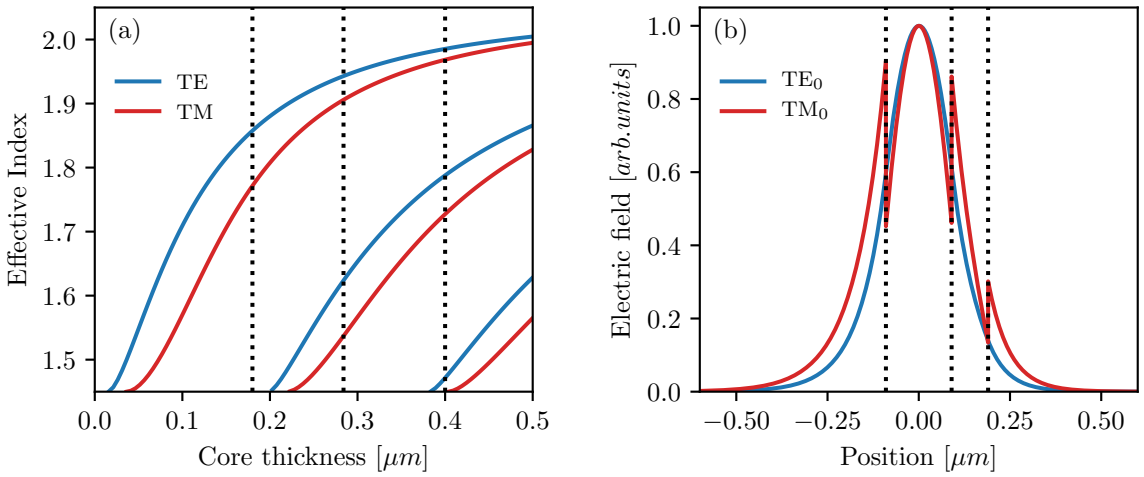

Figure 2.2 Propagation characteristics of slab waveguides. (a) Dispersion curves of the first three TE and TM modes of the waveguide shown in figure 2.1. The dotted lines indicate the different core thicknesses used in this thesis. (b) The electric field profiles of the fundamental TE and TM modes (TE_0 and TM_0), E_y and E_x respectively. The dotted lines indicate the boundaries of the core and the film layers.

similarly shaped profiles but narrower/wider widths. (The three TE modes of the 400 nm core are plotted in figure 3.1 in chapter 3.) The dotted vertical lines mark the boundaries of the core and the boundaries of the PVA film. The width of the electric fields of both modes is quite small and the majority of each field is confined within the core layer; both fields decay to negligible values before $x = \pm 0.5\,\mu m$. The discontinuities at the boundaries for the TM mode are present because it is $E_\perp$ that is plotted and $D_\perp = n^2 E_\perp$ is continuous across an interface. Although it might be difficult to discern, there is more of each field contained in the substrate than the superstrates and the field decays more slowly in this layer since it has the higher refractive index (compared to air). This effect is more apparent for modes of higher order. The overlap of the fields with the film is important for experiments in chapter 3 and it is from plots like figure 2.2(b) that the fraction of a mode overlapping the film is calculated.

Rectangular Waveguides

Complete analytical solutions to rectangular waveguides have not been found but a good approximate solution (Marcatili's method [129], Kumar's method [130]) can often be used. Marcatili's method finds the effective index and fields in two successive steps. The rectangular waveguide is treated as two slab waveguides (the layers of the first perpendicular to the layers of the second and the overlap of the core layers defining the rectangular waveguide's core); the first has a core thickness of the wider dimension of the rectangle and the effective index is found as outlined in the previous section. This effective index is then used as the core refractive index in the second slab waveguide which has the core thickness of

the narrower dimension of the rectangle's core.

As an approximation, this method relies on the fields being well confined to the core of the waveguide because it neglects the fields beyond the corners of the core. Once the core thickness (or width) falls below a certain value (dependent on $^{n_{\text{core}}}/_{n_{\text{clad}}}$ and λ_0) this approximation becomes unreliable and numerical methods are used to find more precise solutions. These numerical methods are described later in the chapter.

2.1.2 Light scattering

Two focusing elements are discussed in this thesis: a microdisk (in chapter 5) and a Fresnel zone plate (in chapter 6). The microdisk is a cylindrical element of the same height and material as the core of the waveguide (Si_3N_4, 180 nm), and has a diameter of a few microns. The Fresnel zone plate (FZP) consists of a number of cylindrical holes in the waveguide core; these holes are filled with PVA and have diameters of a few hundred nanometres. In experiment, the microdisk is positioned just outside the end of the waveguide and is illuminated by light exiting from the waveguide; the FZP is illuminated by a mode propagating in the waveguide (see figure 2.3).

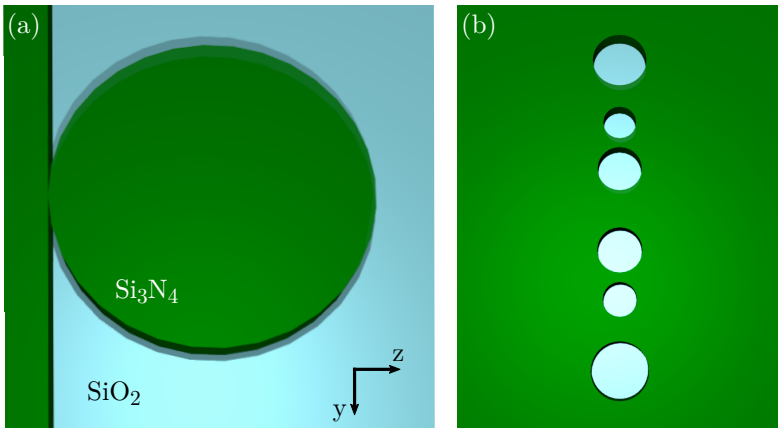

Figure 2.3 Schematic of the light scattering elements used in later experiments. (a) A Si_3N_4 microdisk at the end of a waveguide. (b) A Fresnel zone plate—a combination of holes in the waveguide core.

In figure 2.3, schematics of the two focusing elements used in experiment are shown: (a) microdisk and (b) FZP. (Light propagates along z.) Light incident on these elements is scattered due to the sudden change in refractive index. With visible light, structures with these diameters are too large to be in the Rayleigh scattering regime (where the phase of the incident field can be assumed to be constant over the scatterer) and are too small to be simplified with geometrical optics (where diffractive effects are considered negligible). Thus, the fields must be found by fully solving Maxwell's equations. Fortunately, there are certain geometries for which analytical solutions exist, e.g., spheres and infinitely tall cylinders. Light scattering by objects of these shapes and sizes is usually called Mie scattering since the solutions were found for an infinitely wide plane wave incident on the scatterer by Gustav

Mie [131]. Although the structures in experiment are not infinitely tall, the incident beam does not extend far beyond their height—the full width at half maximum (FWHM) of the TE_0 mode of 180 nm core is ~200 nm—so these solutions provide a good first approximation of how they would scatter the fundamental mode of the waveguide. A full derivation of the scattering by an infinite cylinder can be found in [132, 133]; here, a brief outline of the derivation is given to show how the scattering depends on parameters which are varied in experiment.

In the analytical method for finding how a plane wave is scattered by a cylinder, the symmetry of the cylinder is used and the wave equation is written in cylindrical polar coordinates. Similar to the analysis for a slab waveguide, the wave equation in cylindrical coordinates has modes (or harmonics) and the incident electric field can be written as a linear combination of these modes. To have physically realisable solutions, the boundary conditions at the surface of the cylinder (i.e. interface conditions of continuous $E_\parallel$ and $H_\parallel$) are imposed along with the condition that the scattered field far from the cylinder is an outward travelling wave. Working through these steps, the solutions for the scattered field are found to be

$$\text{(TM) } \vec{E}_\text{s} = -E_0 \sum_{n=-\infty}^{\infty} \mathrm{i}^n b_n H_n^{(1)}(kr) \exp(\mathrm{i}n\phi)\hat{\mathrm{e}}_x \tag{2.4}$$

$$\text{(TE) } \vec{E}_\text{s} = \frac{E_0}{k} \sum_{n=-\infty}^{\infty} \left[\hat{\mathrm{e}}_r \frac{n}{r} + \mathrm{i}k\hat{\mathrm{e}}_\phi \frac{\partial}{\partial kr}\right] \mathrm{i}^n a_n H_n^{(1)}(kr) \exp(\mathrm{i}n\phi), \tag{2.5}$$

where ϕ is the angle made by the scattered wave vector and the z axis, $H_n^{(1)}$ is the Hankel function of the first kind and a_n and b_n are expansion coefficients given by

$$a_n = \frac{mJ_n'(\eta)J_n(m\eta) - J_n(\eta)J_n'(m\eta)}{mJ_n(m\eta)H_n^{(1)\prime}(\eta) - J_n'(m\eta)H_n^{(1)}(\eta)}$$

$$b_n = \frac{mJ_n'(\eta)J_n(m\eta) - mJ_n(\eta)J_n'(m\eta)}{J_n(m\eta)H_n^{(1)\prime}(\eta) - mJ_n'(m\eta)H_n^{(1)}(\eta)},$$

where J_n is the Bessel function of the first kind, the $'$ signifies taking the derivative with respect to the argument, $\eta = {}^{2\pi r_\text{cyl}}/\lambda$ is the size parameter and $m = {}^{n_\text{background}}/_{n_\text{cylinder}}$ is the refractive index ratio. (The expressions given above include the assumption that the incident wave vector is perpendicular to the cylinder axis.) This is the scattered field outside the cylinder; the internal field (the field within the cylinder) is given by a different combination of J_n and $H_n^{(1)}$ but depends on the same parameters. The total field is the vector sum of the scattered field and the incident field. It can be seen from the equations above that the scattered field depends on the diameter of the cylinder (to be precise it depends on the ratio of the diameter to the wavelength but the experiments in this thesis use a fixed wavelength) as well as the refractive index contrast between the cylinder and the surrounding medium (m) through the expansion coefficients. Both of these parameters

are varied in experiments—the diameter is varied in the fabrication process and m is varied by including/removing the PVA-RhB fluorescent dye film.

Although the fields given above contain infinite sums, it has been shown that beyond a certain term further contributions are negligible [134]. This term is $n = \eta + 4.05\eta^{1/3} + 2$. The expressions of the scattered field were written and calculated in Python so that different cylinder parameters (e.g. changing diameter, polarisation, m) could be quickly simulated. Some images of the total intensity (the intensity of the total field) showing the difference made by changing the these parameters are given below.

Microdisk, $m > 1$

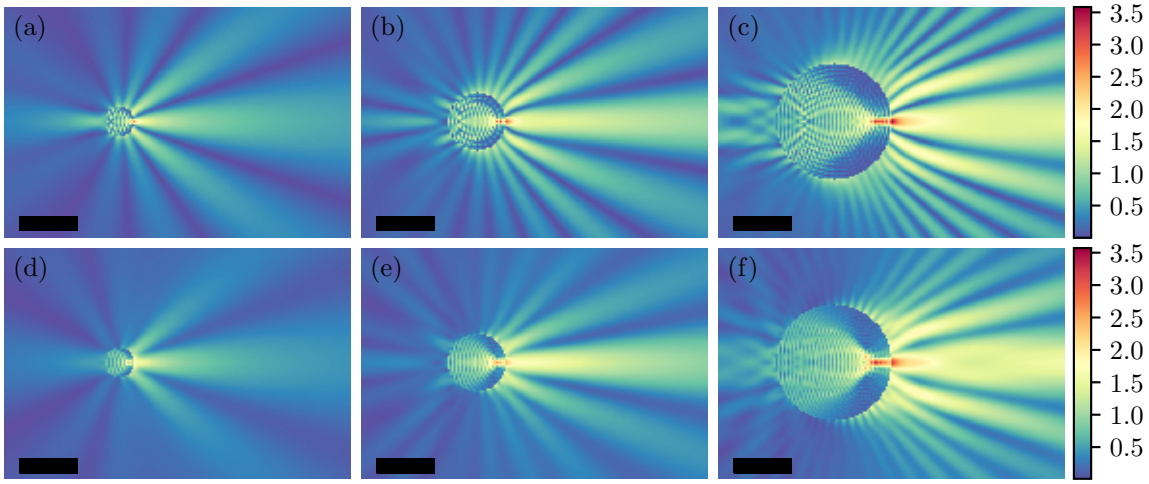

Figure 2.4 Scattered field amplitude when a Si_3N_4 cylinder surrounded by air is illuminated by a plane wave of wavelength 532 nm. (a)–(c) TM polarised input for diameters of 1, 2 and 4 µm, respectively; (d)–(f) show the same diameters for TE polarised input. Scale bar is 2 µm.

For the experiments using microdisks $m > 1$ and is either 1.4 (when the PVA-RhB fluorescent cladding is present) or 2.05 (when there's only air). In this case, the incident wave is focused by the microdisk and the position of the focus is dependent on the refractive index ratio as well as the diameter of the disk. The intensity of the focus depends on the diameter since larger disks have more light incident on them. These aspects can be seen in the images in figure 2.4.

The plots in figure 2.4 map the amplitude of the scattered field for cylinders of diameter 1, 2 and 4 µm with $m = 2.05$ for a TM (a)–(c) and TE (d)–(f) polarised input plane wave. The plots are normalised such that the incident field has an amplitude of 1. It can be seen that larger cylinders produce higher amplitude focal spots and that they also have more diffraction orders/scattering lobes. Comparing across polarisations, for an incident TM wave the focal spot is narrower and slightly higher in amplitude than for a disk of the same diameter with TE polarised input. Intensity maps for the total field (which take into account the interference between the incident and scattered fields) are given in chapter 5.

Inclusion, $m < 1$

For the experiments on FZPs described in chapter 6, $m < 1$ (the cylinder is PVA and the surrounding medium is the Si_3N_4 core layer). With $m < 1$, there is not the same focusing as for $m > 1$ but there is strong forward scattering. By using a combination of these cylinders the indivdual scattered fields interfere to form a focus. (The full structures are shown in chapter 6.) The scattered fields for cylinders of PVA in Si_3N_4 are shown in figure 2.5.

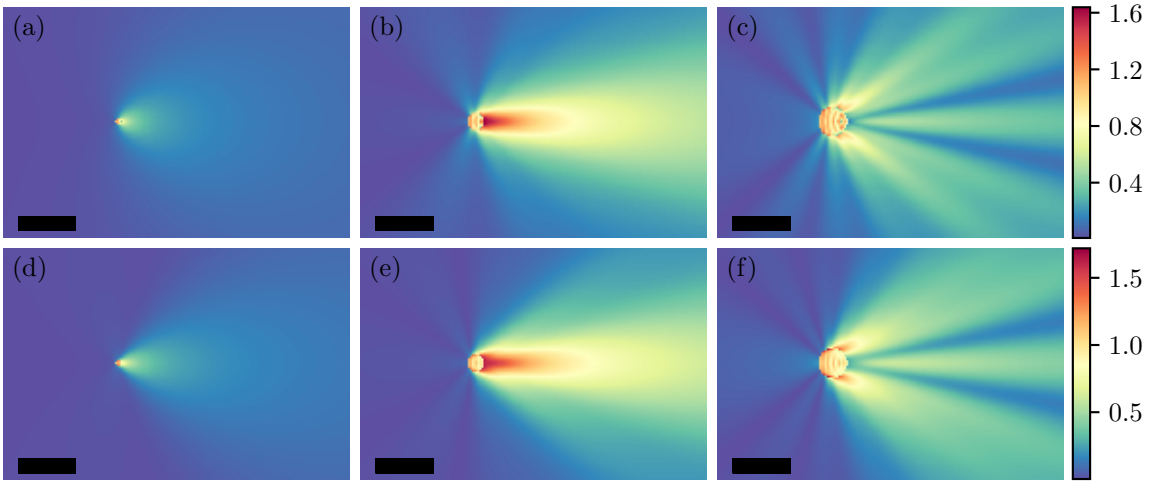

Figure 2.5 Amplitude of the scattered field for PVA cylinders in Si_3N_4. (a)–(c) Incident field is TM polarised for diameters of 0.2, 0.6 and 1 µm, respectively; (d)–(f) same cylinders when the input is TE polarised. Scale bar is 2 µm.

In the plots in figure 2.5 it can be seen how the amplitude of the scattered field varies with cylinder diameter (0.2, 0.4 and 1 µm) and incident field polarisation, (a)–(c) TM and (d)–(f) TE. (The plots are normalised such that the incident field has an amplitude of 1.) As was seen for $m > 1$, the smallest diameter produces the weakest scattered field but unlike $m > 1$, increasing the diameter does not simply increase the forward scattered field. For the largest diameter, there is less light scattered directly forward and the scattered field is stronger at an angle to the forward direction. As before, the scattered fields a few microns away from the cylinder have a similar shape for the two polarisations. The contrast in focusing between cylinders with $m < 1$ and $m > 1$ can be seen by studying figures 2.4(a), (d) and 2.5(c), (f)—because they have the same diameter. The method for designing a focusing element from these individual cylinders is covered in chapter 6.

2.2 Numerical methods

As mentioned earlier, the analytical theory only covers simplified geometries and gives an approximation of what to expect in experiment. Seeing the analytical solution gives a clear insight into the effects of changing different parameters and often gives a better physical understanding of the processes. However, for more complicated geometries analytical solu-

tions have not been found and it is necessary to use numerical methods to make precise simulations of these processes. (An example of a simulation set-up is shown in figure 2.6.) A number of different numerical methods are used to simulated electromagnetic processes with two of the most common being the finite element method (FEM) and the finite difference time domain (FDTD) method. In both of these methods, the simulation region is divided into elements that are fractions of a wavelength in size and although FEM has the advantage of being able to vary the shape of its elements, it is generally heavier on computational resources. Both of these methods were used for simulations over the course of this project but the simulations presented in this thesis, were performed using the FDTD method (through Lumerical's FDTD Solutions software [135]).

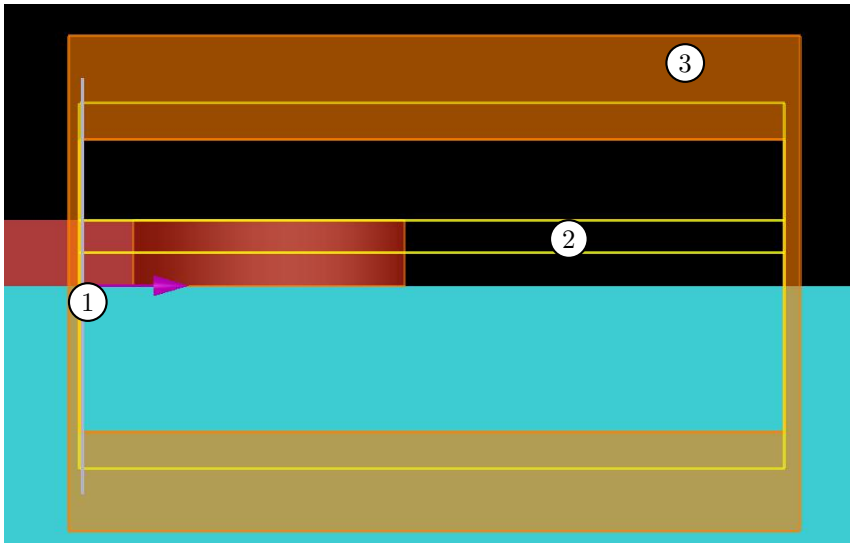

Figure 2.6 Simulation window in Lumerical's FDTD solutions. Some of the elements used to define the simulation are marked: including the input light source (1), 'monitors' (2) and the simulation boundary (3).

Figure 2.6 shows a two dimensional cross section of the simulation set-up in Lumerical's FDTD solutions. The input source (marked 1) is indicated by a faint line and an arrow pointing in the direction of propagation; 'monitors' (marked 2) are planes on which the electric and magnetic fields are stored—even though the fields are calculated over the entire simulation region, the values are only stored for desired coordinates—and the power flow through these planes is also calculated; the region marked 3 is the edge of the simulation domain where boundary conditions are set. A brief outline of the FDTD method is given below, covering the use of these elements and results which can be obtained from FDTD simulations.

Finite Difference Time Domain method

In the FDTD method, Maxwell's equations still need to be solved but to simplify the calculations the electric and magnetic fields are discretized in both time and space [136, 137].

The discretization of time is done by choosing a suitable time step (Δt) and calculating the fields only at these intervals. However, to improve accuracy the calculations of the fields are offset from each other half an interval, as such

$$\vec{E}(t) \rightarrow \vec{E}^{n\Delta t}, \qquad \vec{H}(t) \rightarrow \vec{H}^{(n+\frac{1}{2})\Delta t}.$$

The method for discretizing space was proposed by Yee [138] and works by first dividing the simulation region into a grid and then separating the electric and magnetic field components to different points of the grid cells (see figure 2.7(a)). Displacing the different field components in this way makes calculating the curl expressions in Maxwell's equations easier. The fields are given by the recursion relations

$$\vec{E}^{(n+1)\Delta t} = \vec{E}^{n\Delta t} + \nabla \times \vec{H}^{(n+\frac{1}{2})\Delta t}$$
$$\vec{H}^{(n+\frac{3}{2})\Delta t} = \vec{H}^{(n+\frac{1}{2})\Delta t} + \nabla \times \vec{E}^{(n+1)\Delta t}.$$

The fields are calculated for each step until a set time is reached or until the fields have decayed to a specified fraction of the incident field. By offsetting in time the calculations of the fields, the simulations are relatively light on computational power but there is the disadvantage that the fields are not known simultaneously. There is the same disadvantage in space as the fields are never calculated at the same position and must be interpolated if they are to overlap the same exact point in space. These aspects make it important to choose suitably small grid cell sizes (typically $\sim\lambda/6$) and time steps (typically $\sim c/(\lambda/6)$).

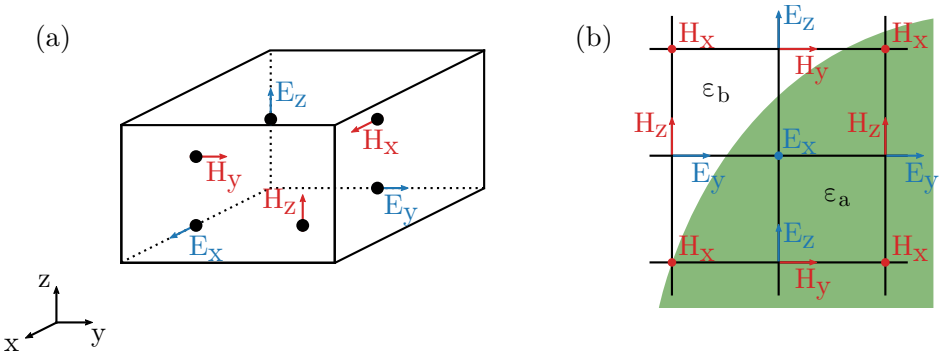

Figure 2.7 Yee cells used in FDTD to define the spatial components of the electromagnetic fields. (a) 3D grid used in FDTD showing the separation of the field components to different points in the cell. (Based on [138].) (b) 2D grid across the curved interface of two materials, ε_a and ε_b, used for calculating the modes of a cross section of waveguide. (Based on [139].)

In Lumerical's FDTD solutions, the incident field can be defined manually or by using one of the Lumerical's source generators. To simulate the waveguide modes which propagate in our experiments the 'mode source' was used to define the incident field. To find the modes of the waveguide Lumerical uses a finite difference eigenmode (FDE) solver based on Zhu

and Brown's method [139] but with proprietary modifications and extensions [135]. The eigenmode solver works by discretizing the fields onto a mesh of a 2D cross section of the waveguide (see figure 2.7(b)) and writing the wave equation in matrix form [139]

$$\mathrm{i}k_0 \begin{pmatrix} \mathbf{H}_x \\ \mathbf{H}_y \\ \mathbf{H}_z \end{pmatrix} = \begin{pmatrix} \mathbf{0} & -\mathrm{i}\beta\mathbf{I} & \mathbf{U}_y \\ \mathrm{i}\beta\mathbf{I} & \mathbf{0} & -\mathbf{U}_x \\ -\mathbf{U}_y & \mathbf{U}_x & \mathbf{0} \end{pmatrix} \begin{pmatrix} \mathbf{E}_x \\ \mathbf{E}_y \\ \mathbf{E}_z \end{pmatrix}, \tag{2.6}$$

where $\mathbf{I}$ is the identity matrix and $\mathbf{U}_{x,y}$ are square matrices defined by the boundary conditions of the simulation region. From equation (2.6) the eigenvalue equation is found as

$$\mathbf{P} \begin{pmatrix} \mathbf{E}_x \\ \mathbf{E}_y \end{pmatrix} = \beta^2 \begin{pmatrix} \mathbf{E}_x \\ \mathbf{E}_y \end{pmatrix},$$

where $\mathbf{P}$ is a 2×2 matrix made up of a combination of the variables from equation (2.6). The eigenvalue equation can then be solved quickly by many computational techniques returning the fields and effective indexes of the modes. (In Lumerical the fields are normalised such that $|E|^2 = 1$.) This FDE solver can find the modes of rectangular waveguides which are beyond the scope of analytical methods. Using these modes as the incident fields, precise simulations of the experimental measurements could be performed. A few examples of the FDTD method simulations are given below.

Rectangular Waveguides

Rectangular waveguides are used with the focusing elements described later in chapters 5 and 6. Unlike the modes of slab waveguides, the electromagnetic fields of rectangular waveguide modes are not strictly TE or TM but have finite components of their electric or magnetic fields along the direction of propagation. For the core widths used in this thesis the longitudinal field component is much weaker than the transverse component and the modes are still referred to as TE and TM. Since the core of the waveguide now has finite length in both transverse directions, the field and intensity distributions are structured along both the x and the y direction (as opposed to just along x for slab waveguides). This can be seen in the intensity maps in figure 2.8.

In figure 2.8, intensity maps for the modes of a rectangular waveguide (calculated with Lumerical's FDE solver) are shown. The material layers of the waveguide are the same as for the slab waveguide described earlier but for these calculations the width (along y) of the core was 5 µm. Truncating the core width and thus causing the refractive index to change along y, the field profiles now have some y dependence as can be seen in each of the images. The plot in figure 2.8(a) maps the variation of intensity of the fundamental TE mode (TE_{00}) on a cross section of the waveguide and (b) shows the same for TM_{00} (the discontinuities in intensity can be seen at the boundaries parallel to y). In (c) and (d), it can be seen that the field can have intensity nodes along both x and y directions; the modes plotted are

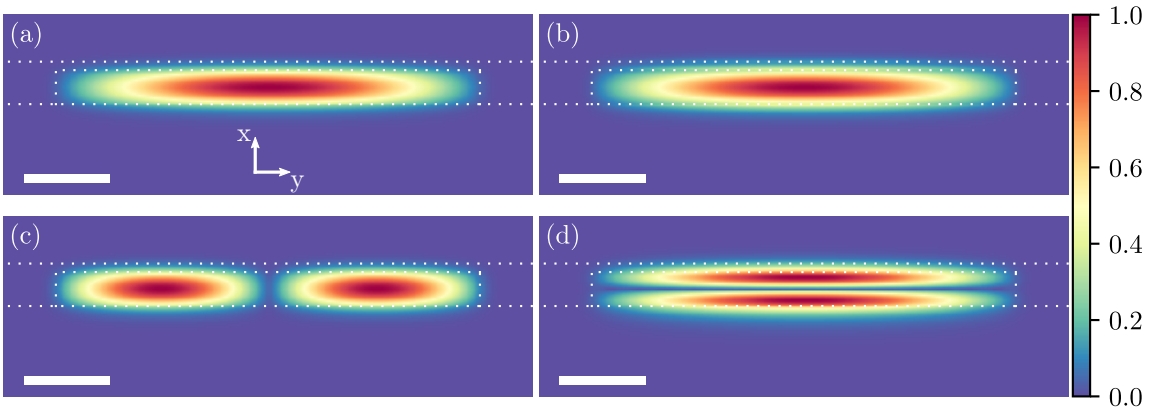

Figure 2.8 Modes in a rectangular waveguide—core width 5 µm and thickness 400 nm. The material layers are the same as for the slab shown in figure 2.1 and light propagates along z. (a) Intensity map of the fundamental TE mode (TE_{00}), (b) TM_{00}, (c) TE_{01} and (d) TE_{10}. The dotted lines mark the boundaries of the substrate, core and PVA-RhB film. The scale bar is 1 µm.

TE_{01} and TE_{10}, respectively. In the ideal case, only the fundamental modes would be used for illuminating any focusing elements; when higher order modes are focused the intensity profile of the focal spot contains multiple peaks, similar to their intensity profile before focusing.

Disk illuminated by waveguide

Once the modes have been found they can be used as the illumination source for the different focusing elements. From the mode profiles shown above in figure 2.8 it can be seen that the incident field is much narrower than in the case of the analytical solutions shown earlier (see figure 2.4). An example of a 3 µm microdisk illuminated by the fundamental TM mode of a 6 µm wide waveguide is shown in figure 2.9. The intensity maps are taken through the centre of the waveguide in both height and width and are normalised such that the peak incident intensity is 1.

A more comprehensive description of the 3D simulations for microdisks is given in chapter 5 but here a couple of the differences with the analytical solutions are stated. The first is simply that the incident intensity varies over the disk and so there is a variation of the contribution of the different angles from which light is gathered. Possibly the greater factor is the divergence of the incident field as it exits from the Si_3N_4 layer. This can be seen in the bottom image of figure 2.9. This effect is completely neglected in the analytical solutions since they are effectively two dimensional. It might be seen that the divergence affects how much light the microdisk can gather and also the intensity of the focus.

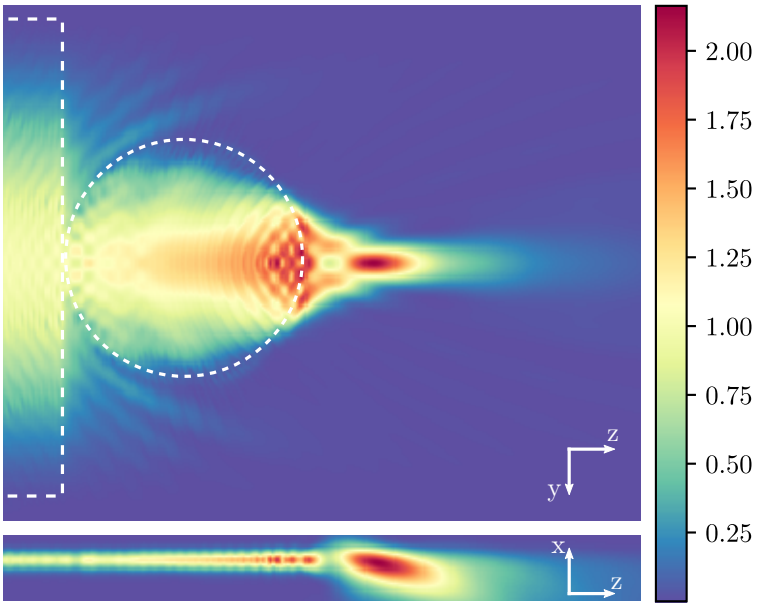

Figure 2.9 A 3 µm diameter disk illuminated by the fundamental TM mode of a 6 µm wide rectangular waveguide. Intensity cross sections through the centre of the Si_3N_4 layer as top and side views. The dotted lines mark the boundaries of the core and the disk.

Hole in waveguide core

Simulating a slab waveguide mode in FDTD can be problematic due to the non-zero propagating fields at the simulation boundaries; to overcome this, periodic boundary conditions are used. This boundary condition is similar to simulating an infinite array of the structure in the defined simulation region which allows for non-zero propagating fields at boundaries but causes unrealistic interference from the *virtual* neighbouring structures. However, this effect was not deemed detrimental and so simulations were performed in this way. An example is shown in figure 2.10

The interference caused by "neighbouring cells" can be seen as the ripple effect in the intensity maps in figure 2.10. The underlying intensity caused by a solitary hole can be determined and, as with the microdisk above, there is a full discussion in chapter 6. The agreement between the analytical method and this numerical method is also discussed in that chapter. In the image at the bottom of figure 2.10 it can be seen that some light is lost from the waveguide core when it reaches the hole.

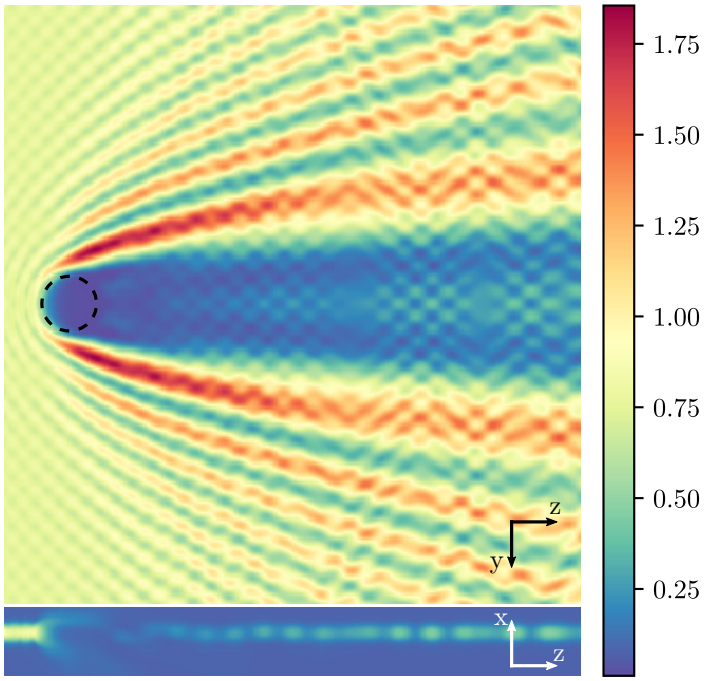

Figure 2.10 Intensity map for a hole (filled with PVA) in the core layer of the slab waveguide shown in figure 2.1 illuminated by the fundamental TE mode. The cross sections are taken through the centre of the core layer (top) and the centre of the hole (bottom). The dashed line in the top image marks the boundary of the hole.

2.3 Diffraction limited imaging

The experimental work described in later chapters relies on imaging and uses an optical microscope which is limited in its resolution. For all the simulations shown and discussed above, the resolution is limited by either the computing power or by time constraints since the grid spacing can be made smaller and smaller. This resolution, however, is not physically realisable because in far-field imaging experiments there is a fundamental limit on how separated two features must be before they can be resolved. This limit was first noted by Ernst Abbe and later refined to the expression [140]

$$\Delta x = 0.61 \frac{\lambda_0}{n \sin \theta}. \tag{2.7}$$

Abbe stated—in 1873—that two objects separated by less than Δx will not be resolvable and will appear to overlap in an image. The $n \sin \theta$ can be replaced with the numerical aperture (NA) quoted on objectives and a lower limit calculated for an imaging set-up. With a NA of 0.6 or 0.65 and λ_0 of either 532 nm (the laser used in experiment) or 580 nm (the peak of the RhB fluorescence spectrum) the minimum resolvable separation for the imaging system used in this work is ~550 nm. This is the theoretical lower limit and is increased in experiment if images are out of focus or elements in the imaging system are misaligned.

This characteristic of imaging systems also affects isolated features. Anything smaller than the right hand side of equation (2.7) is imaged as an Airy disk with a central spot width equal to equation (2.7). This broadening of the feature is accompanied by an apparent decrease of intensity since the power collected from the feature is now spread out over a larger area. This effect can make a focal spot appear wider and less intense in measurement if it is smaller than the diffraction limit of the set-up.

In the simulated intensity maps shown above, it can be seen that some of the features are beyond the resolution of the imaging set-up used for measurements. To demonstrate the broadening effect clearly, some simulated intensity maps were convolved with a Gaussian profile to convert them from 'infinitesimal resolution' to the resolution of the imaging system used in this thesis.

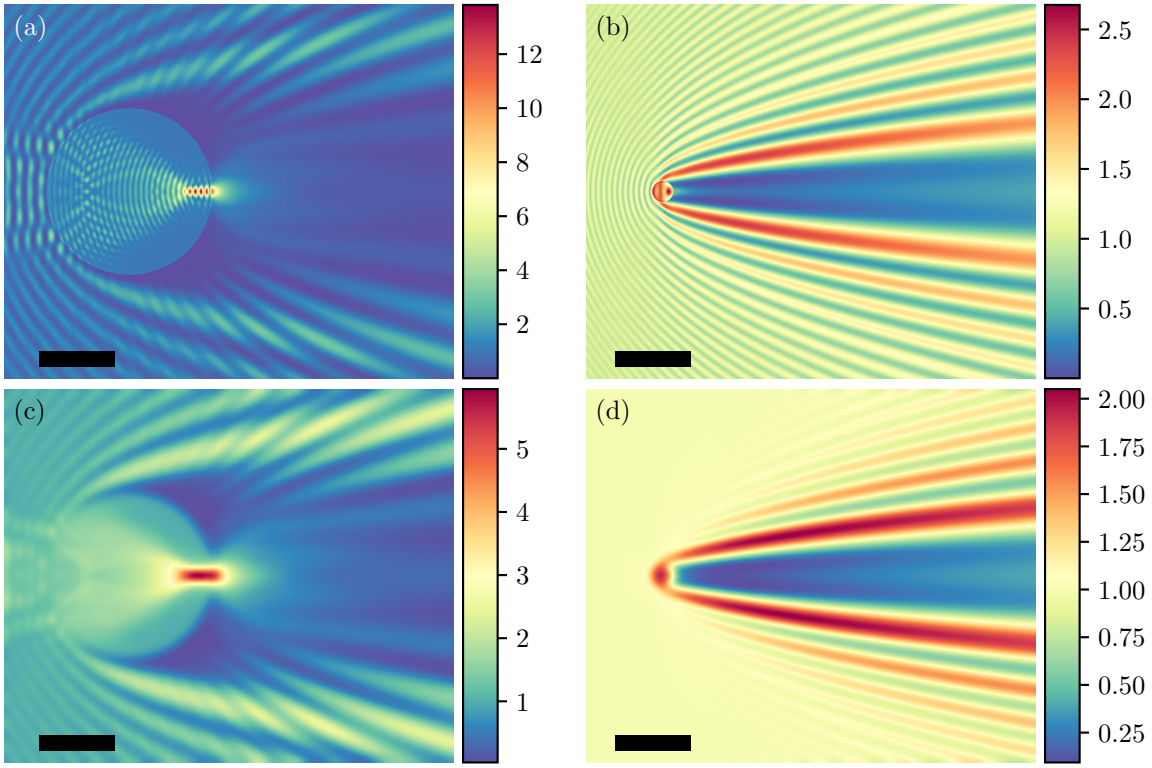

Figure 2.11 The effects of the blurring caused by an imaging system with finite resolution. (a) and (b) Analytically calculated intensity maps for a microdisk and a hole, respectively. (c) and (d) The intensity maps from (a) and (b) passed through a Gaussian filter of width 500 nm. Scale bar is 2 µm.

The intensity maps in figure 2.11 show how a simulated image might look when imaged in a diffraction limited set-up. (a) and (b) are intensity maps of the total field calculated analytically for cylinders of diameter 4 and 0.6 µm with $m = 2.05$ and 1.4, respectively. For these images, the resolution is only limited by the spacing between the points where the fields are calculated—the spacing was set to 15 nm in this case. The clearest measure of this resolution is the clarity of the $\lambda/2$ standing wave in (b) caused by the reflection of the

incident wave by the hole. This standing wave has a peak to peak separation of ~130 nm which is far beyond the resolution of the experimental imaging system. Figure 2.11(c) and (d) show the intensity maps from (a) and (b) after they are blurred to a resolution of 550 nm. This *blurring* was achieved by convolving the simulated intensity map with a Gaussian profile that had a FWHM of 550 nm. The profile was normalised so that it summed to one; this normalisation was used so that the total power in the original image and in the blurred image would be equal. The difference made by blurring the original images is clear with the focus of the microdisk broader and the *ripples* near to the hole completely smoothed out. The reduction of intensity can be seen from the change of scale on the colorbars. In (a) the microdisk focuses to a peak intensity ~14 but in (c) this is reduced to ~6. A similar but less drastic reduction can be seen for (b) and (d). The reason for the difference between the images can be most easily pictured when considering what would happen for a point source of light. In a simulation, this would appear as a single intense pixel surrounded by dark pixels. After convolving as above, the point source would appear as a Gaussian distribution of intensity with a FWHM of 550 nm (~37 pixels). As well as increasing the width of the spot, convolving reduces the peak intensity since the power from the point source is now spread over a larger area.

3 Mode beating in slab waveguides

The concept of a waveguide mode was covered in chapter 2, which included a discussion on multiple modes propagating simultaneously. In this chapter, a simple non-destructive experimental technique to characterise these modes in terms of their effective indexes and relative propagation losses is discussed. The technique, based on imaging the fluorescence of a thin dye-doped cladding layer, is applied to the slab waveguide described in chapter 2. Although the results presented here are for Si_3N_4 slab waveguides in the visible range, the technique could easily be generalised to characterise multi-mode wave propagation in different materials systems and any integrated optical devices. For example, the same method can be readily applied to rib waveguides and recently a similar method has proven useful for plasmonic waveguides [141].

3.1 Importance of non-destructive measurement

While a theoretical analysis can compute the number of modes (and their electric fields) supported by a given waveguide structure, the modes excited when coupling light into the waveguide in an experimental arrangement can vary. The incident angle and focal properties of the input beam determine which modes are excited; as the modes propagate, the roughness of the surfaces and different features (e.g. bends or tapers) of the waveguide induce scattering between modes. These complications mean that the actual distribution of energy among the modes propagating at a given time/position is not easily calculated. It is worth mentioning that even though the theoretical analysis gives an exact mode structure, when working in the visible spectrum of light even small changes of layer thickness or values of refractive index can move the cut-off frequency (see chapter 2) appreciably and increase/decrease the number of modes supported. With this in mind, a non-destructive method for experimentally determining the number of modes propagating in a waveguide and, in certain cases, the energy distribution among them is described in the current chapter.

Different techniques have been developed for measuring the modal characteristics of dielectric waveguides. Depending on what information is desired and the type of waveguide

under investigation (e.g., buried channel, slab, planar), certain techniques are more suitable than others. Interferometric techniques have been developed to measure refractive index profiles [142]; the prism coupler technique is used to quantify the number of modes and their effective indexes [143]; imaging the modes at the end-face of the waveguide can also return the refractive index profile [144]; near-field imaging techniques have been used to map the intensity in the waveguide and determine the effective indexes of modes [145, 146]. These methods were covered in detail in chapter 1. Generally, prism or grating out-coupling of the modes is used to determine the number of modes propagating in the waveguide at a specific, fixed position. These methods rely on momentum matching and, as each mode has a different propagation constant, the modes couple out at different angles. These methods can be cumbersome; the prisms used are usually quite large (at least compared to typical nanophotonics structures) while incorporating a grating into the waveguide structure is often not desirable as it irreversibly changes the waveguide structure.

3.2 Theory

The measurements in this chapter were made on waveguides consisting of the material layers described in section 2.1.1—a Si_3N_4 core of variable thickness on a SiO_2 substrate and a 100 nm thick polyvinyl acetate (PVA) film coated on the Si_3N_4. (A cross section of the waveguide is shown in figure 3.1(a).) To aid imaging the PVA film was doped with the fluorescent dye rhodamine B (RhB). Two thicknesses of core layer were tested: 284 nm (thickness measured by ellipsometry) and 400 nm (average thickness from manufacturer's measurements). Using the analytical methods outlined in chapter 2, the number of modes supported by the waveguides and the effective indexes of these modes were found. (With the materials used here, core thicknesses less than 200 nm would support only the fundamental TE and TM modes.) The electric field profiles of the modes were also found and were plotted to obtain the overlap of each field with the region containing the fluorescent dye-doped cladding—see figure 3.1(b).

As was briefly mentioned in chapter 2, each mode of the waveguide has a different field profile. The lower the order of the mode the more its field is confined to the core and for a given mode, the field permeates more into the cladding which has higher refractive index (in our case the substrate). The electric field of the three TE modes supported by the waveguide with a 400 nm thick core is shown in figure 3.1(b) with the field in the PVA-dye layer ($0.2\,\mu m \leq x \leq 0.3\,\mu m$) highlighted. The fields have been normalised by $k_m \int_{-\infty}^{+\infty} |E_{y,m}|^2 dx$ where k_m and $E_{y,m}$ are the propagation constant and the electric field of the m^{th} mode. This normalisation means each mode contains the same power so the size of the shaded region indicates how much fluorescence one mode would excite compared to the others if they contained the same power. The ratio of the portion of the field overlapping the dye to the total field is the amount available to excite the dye and is referred to later in the chapter as E_{exc}. From the plots, it can be seen for these modes that as the order of the

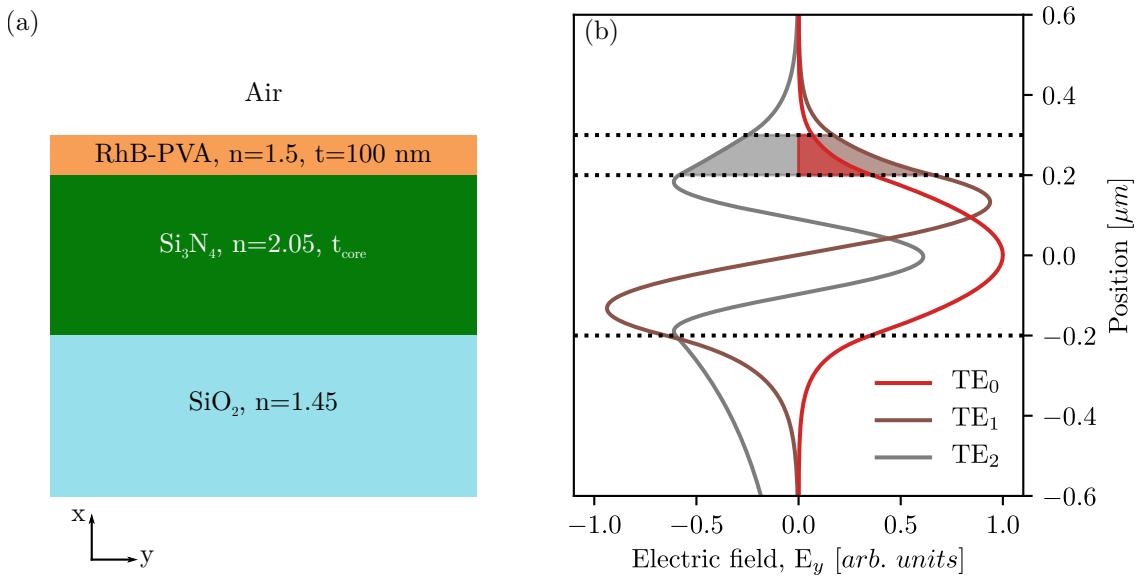

Figure 3.1 Electric field, E_y, profile of the three TE modes in the 400 nm thick core—the fields have been normalised such that each mode contains the same power. The highlighted region between $x = 0.2\,\mu$m and $x = 0.3\,\mu$m signifies the overlap of the field and the PVA-dye film. This overlap is the fraction of the field that can excite the dye.

mode increases, E_{exc} increases. (This might be the expected general case.) One exception among our samples is for the TM modes of the 284 nm thick core. In this case, the first order mode has a lower percentage of its field in the PVA-dye film than the fundamental mode has. This happens as the field decays more slowly into the substrate than the superstrate and while there is an increase of field in the film compared to the core, there is much more of an increase in the substrate. The percentages of the field overlap are given in table 3.1 along with the effective indexes of each mode.

Table 3.1 Calculated effective indexes and mode-dye overlap

t_{core} [nm]	Order	n_{eff}		Overlap [%]	
		TE	TM	TE	TM
400	0	1.985	1.968	5.04	5.68
	1	1.788	1.727	10.0	11.3
	2	1.472		12.3	
284	0	1.941	1.903	8.26	9.70
	1	1.616	1.530	14.7	7.84

From the analysis it was found that there are five modes (three TE and two TM) supported for a core thickness of 400 nm and four modes (two TE and two TM) supported

by a 284 nm thick core. Plots of the dispersion show that a 400 nm core is very close to the cut-off for the second order TM mode and the second order TE mode. Increasing the core layer thickness (with all other layers kept constant) to 403 nm the waveguide would allow the waveguide to support six modes in all, while decreasing it to 382 nm would allow the waveguide to support only four.

Mode beating

The experimental method described in this chapter relies on the interference between the different modes co-propagating in the waveguide. When two waves with parallel polarisation but different frequency propagate together they interfere and 'beat'. This beat is comprised of a quickly oscillating wave (with a frequency of the sum of the interfering waves) in a slowly oscillating envelope (with a frequency of their difference). Beats are commonly noticed in music, where two notes of similar pitch played together are heard as one slowly pulsing note. The same effect can happen in the case of light and a waveguide is an ideal structure for studying it, since the waves are well aligned over long distances. In this setting, it is a difference of spatial frequency which causes the interference. Once the propagation constants of the different modes of a waveguide have been found (see table 3.1, method in chapter 2), the way they interfere can be deduced. The two important components of this beat wave are its amplitude which can be used to find the amplitude of the individual modes and the frequency which is used to determine the difference in effective index of the individual modes.

For two modes (indexed by i and j) with field amplitudes $E_{i,j}$ and wavenumber $k_{i,j}$, the amplitude of the beat wave is expressed as $A_{\text{beat}} = \frac{(k_i+k_j)}{(\kappa_{i,\text{f}}+\kappa_{j,\text{f}})} E_i E_j$ and was found as follows. ($\kappa_\text{f} = \sqrt{k^2 - n_\text{f} k_0^2}$, see chapter 2.) The analysis here can be directly applied to the experimental data, since the maps of the fluorescent intensity are proportional to the electromagnetic power (P) of the coupled waveguide modes.

$$P = \iint_S \frac{1}{2} \Re \left\{ \left(\vec{E} \times \vec{H^*} \right) \cdot \vec{u}_z \right\} ds,$$

where $\Re$ denotes taking the real part of the term within the braces and $*$ denotes the complex conjugate. For a TE mode travelling in the z-direction with layer interfaces in the y-z plane (see figure 3.2 for the coordinate system), we have $\vec{E} = (0, E_y, 0)$, reducing the previous equation to

$$P = \int \frac{1}{2} \Re \left\{ -E_y H_x^* \right\} dx.$$

For a TE mode, $H_x = -\frac{k}{\omega \mu_0} E_y$ and the total E and H fields are the sum of the fields over the orders of modes. For a core thickness of 400 nm there are three TE modes (see table 3.1), so $m = 1, 2, 3$ and

$$E_y = \sum_m E_m, \qquad\qquad H_x = \sum_m H_m,$$

$$E_y = E_1 \exp(\mathrm{i}k_1 z) + E_2 \exp(\mathrm{i}k_2 z) + E_3 \exp(\mathrm{i}k_3 z)$$
$$H_x = -\frac{k_1}{\omega\mu_0} E_1 \exp(\mathrm{i}k_1 z) - \frac{k_2}{\omega\mu_0} E_2 \exp(\mathrm{i}k_2 z) - \frac{k_3}{\omega\mu_0} E_3 \exp(\mathrm{i}k_3 z).$$

Taking the product of the fields

$$\begin{aligned}
E_y H_x^* &= \Big[E_1 \exp(\mathrm{i}k_1 z) + E_2 \exp(\mathrm{i}k_2 z) + E_3 \exp(\mathrm{i}k_3 z)\Big] \frac{1}{\omega\mu_0} \Big[- k_1 E_1 \exp(-\mathrm{i}k_1 z) - \\
&\qquad k_2 E_2 \exp(-\mathrm{i}k_2 z) - k_3 E_3 \exp(-\mathrm{i}k_3 z)\Big] \\
&= -\frac{1}{\omega\mu_0} \Bigg[\Big(k_1 E_1^2 + k_2 E_2^2 + k_3 E_3^2\Big) + E_1 E_2 \Big(k_2 \exp[\mathrm{i}(k_1 - k_2) z] + k_1 \exp[\mathrm{i}(k_2 - k_1) z]\Big) \\
&\qquad\qquad + E_2 E_3 \Big(k_3 \exp[\mathrm{i}(k_2 - k_3) z] + k_2 \exp[\mathrm{i}(k_3 - k_2) z]\Big) \\
&\qquad\qquad + E_1 E_3 \Big(k_1 \exp[\mathrm{i}(k_3 - k_1) z] + k_3 \exp[\mathrm{i}(k_1 - k_3) z]\Big) \Bigg] \\
&= -\frac{1}{\omega\mu_0} \Bigg[\Big(k_1 E_1^2 + k_2 E_2^2 + k_3 E_3^2\Big) + E_1 E_2 \Big[\sigma_{1,2} \cos(\Delta_{1,2} z) + \mathrm{i}\Delta_{2,1} \sin(\Delta_{1,2} z)\Big] \\
&\qquad\qquad + E_2 E_3 \Big[\sigma_{2,3} \cos(\Delta_{2,3} z) + \mathrm{i}\Delta_{3,2} \sin(\Delta_{2,3} z)\Big] \\
&\qquad\qquad + E_1 E_3 \Big[\sigma_{1,3} \cos(\Delta_{3,1} z) + \mathrm{i}\Delta_{1,3} \sin(\Delta_{3,1} z)\Big] \Bigg],
\end{aligned}$$

where $\Delta_{i,j} = k_i - k_j$ and $\sigma_{i,j} = k_i + k_j$. Taking the real part and putting this into our expression for P, we have

$$\begin{aligned}
P = \frac{1}{2\omega\mu_0} \int \Big[\Big(k_1 E_1^2 + k_2 E_2^2 + k_3 E_3^2\Big) &+ E_1 E_2 \, \sigma_{1,2} \cos(\Delta_{1,2} z) \\
&+ E_2 E_3 \, \sigma_{2,3} \cos(\Delta_{2,3} z) \\
&+ E_1 E_3 \, \sigma_{1,3} \cos(\Delta_{3,1} z)\Big] dx.
\end{aligned}$$

Recalling that E_1, E_2, and E_3 are functions of x (as seen in figure 3.1(b)), the power is a function of x and z (this is shown in figure 3.2(c) for the 400 nm thick core). The limits for the integral are the upper and lower surfaces of the dye film as that is the portion of the E-field that excites the fluorescence which is imaged in experiment. The expression for the electric field in the dye film is given in equation (2.1) and all that needs to be remembered here is that it depends on x as $\exp(-\kappa_{m,\mathrm{f}} x)$, $\kappa_{m,\mathrm{f}} = \sqrt{k_m^2 - n_\mathrm{f} k_0^2}$. (Where $\kappa_{m,\mathrm{f}}$ is the field's decay constant in the film and k_m is the propagation constant of the mode of order m.) Substituting in and performing the integration we arrive at

$$\begin{aligned}
P = \frac{-1}{2\omega\mu_0} \Big[\left(\frac{k_1}{2\kappa_{1,\mathrm{f}}} E_1^2 + \frac{k_2}{2\kappa_{2,\mathrm{f}}} E_2^2 + \frac{k_3}{2\kappa_{3,\mathrm{f}}} E_3^2\right) &+ E_1 E_2 \, \frac{\sigma_{1,2}}{(\kappa_{1,\mathrm{f}} + \kappa_{2,\mathrm{f}})} \cos(\Delta_{2,1} z) \\
&+ E_2 E_3 \, \frac{\sigma_{2,3}}{(\kappa_{2,\mathrm{f}} + \kappa_{3,\mathrm{f}})} \cos(\Delta_{3,2} z) \\
&+ E_1 E_3 \, \frac{\sigma_{1,3}}{(\kappa_{3,\mathrm{f}} + \kappa_{1,\mathrm{f}})} \cos(\Delta_{1,3} z)\Big]. \qquad (3.1)
\end{aligned}$$

The negative sign just indicates that P decreases as x increases (i.e. if we put in our integration limits we would get a positive number). It can be seen that there is a 'D.C.' term and a term which oscillates with z (i.e. the beat). The amplitude of the beat is proportional to the product of the amplitudes of the underlying modes ($E_i E_j$) and to the ratio of their longitudinal wavevector components to their transverse ($^{\sigma_{i,j}}/_{(\kappa_{i,\mathrm{f}}+\kappa_{j,\mathrm{f}})}$).

The oscillating part of equation (3.1) has three separate components (one for each pair of waves) each with period $^{2\pi}/_{\Delta_{i,j}}$. As a spatial frequency, this can be related back to the effective indexes by

$$\begin{aligned}
\frac{\Delta_{i,j}}{2\pi} &= \frac{k_i - k_j}{2\pi} \\
f_{\mathrm{beat}} &= \frac{2\pi\left({}^{n_{\mathrm{eff},i}}/_{\lambda_0} - {}^{n_{\mathrm{eff},j}}/_{\lambda_0}\right)}{2\pi} \\
f_{\mathrm{beat}} &= \frac{n_{\mathrm{eff},i} - n_{\mathrm{eff},j}}{\lambda_0}. \qquad (3.2)
\end{aligned}$$

Thus, the beat frequencies depend linearly on the difference between the effective indexes of the modes. Because of this simple relationship, a Fourier transform of the intensity profile along the direction of propagation (z) provides three values for f_{beat}, which can then be used to calculate $n_{\mathrm{eff},i}$ using equation (3.2).

To visualise the mode beating, some simulated intensity surfaces are shown in figure 3.2. These intensity maps were made by propagating the three TE modes of the 400 nm thick core together. A top-view (looking down onto the Si_3N_4 surface) and a side-view (the layers of the waveguide stacked vertically) are given. (The scale in the side-view is different in the vertical and horizontal directions—the scale bar marks 5 µm in the horizontal direction but the total vertical scale is 2 µm.)

The intensity patterns in figure 3.2 are constant over time as a result of the fixed relative phase between the modes when they are coupled to. Points of high intensity are in red while low intensity are blue and the evanescent decay of the intensity outside the core of the waveguide (decaying more slowly into the substrate) can be seen. The top-view (b) is the type of image taken in experiment (see e.g. figure 3.6) and has variation in only the z-direction. The side-view displays in more detail how the modes interfere and might also make clear the need to determine the overlap percentages given in table 3.1. It can be seen that an intensity profile taken along z will depend on its x coordinate (it would not simply be shifted left or right but will have a different structure). Since the wavenumber of the modes doesn't change with x, the factor which changes the intensity structure is the modes' relative amplitudes. This was confirmed by Fourier transforms of the simulated intensity taken for different x coordinates.

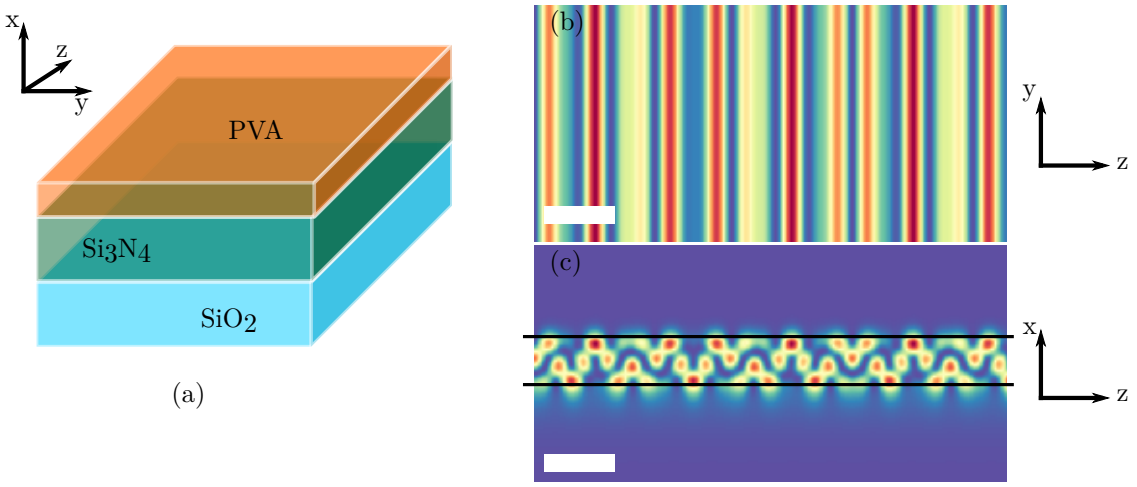

Figure 3.2 Intensity surfaces for multi-mode propagation in a slab waveguide. (a) The layers and coordinate system for the waveguide being studied. (b) Top-view (at Si_3N_4-PVA interface) with modes propagating to the right. (c) Side-view as modes propagate to the right with the black lines marking the boundaries of the core. Scale bar is 3 µm.

3.3 Experiment

3.3.1 Fabrication and set-up

To simultaneously excite multiple modes in the waveguide, end-fire coupling was used. End-fire coupling is the method of coupling light into a waveguide by focusing a beam onto the end-face of the waveguide. The efficiency of coupling to a specific mode is given by the overlap of the profile of the focused beam and that of the mode [71]. To produce a flat edge for end-fire coupling a number of separate slots were etched through the Si_3N_4 layer using UV lithography (to define an etch mask) and an inductively coupled plasma (ICP) etch with Ar and CHF_3. After these slots were created, a cladding layer (5% w/w PVA, 10^{-4} M RhB in water) was spin-coated onto the Si_3N_4, to a thickness of ~100 nm. The refractive index of this dye-doped layer was measured as 1.5 using ellipsometry. The light source for these experiments was a 4.5 mW, 532 nm wavelength (low polarisation ratio) diode laser. A neutral density filter of optical density 1.0 was included to reduce photobleaching. The power coupled into the waveguide was sufficiently low to avoid any non-linear effects in the dye. For most of the experiments discussed here a film polariser (>99% extinction) was used for polarisation specific coupling. A demonstration that the method works for unpolarised input and that the result is a simple superposition of the two orthogonal polarisations without any inter-polarisation interference (as exepected from the Fresnel-Arago laws) is given towards the end of the chapter. A 40x, 0.6 NA (numerical aperture) microscope objective was used for the imaging, along with a monochrome CCD camera. The camera is a 1024-by-768 (width-by-height) array of square pixels, each of width 4.65 µm. With this magnification, the effective pixel size was 0.11 µm which corresponds to a maximum

sampling rate of ~4.5 µm^{-1} ($f/2$). This sampling rate was greater than the beat frequency defined in equation (3.2) (f_{beat} sets the lower limit for the sampling rate in experiment). In the fourier transform (FT), the frequency resolution (for a fixed sampling rate) is determined by the number of sampling points (in our case, half the number of pixels in one row on the CCD). The frequency resolution was equivalent to a resolution of ~0.005 in refractive index. Although this is not outstanding in terms of refractive index measurements, it is achievable with standard, low cost lab equipment. Higher resolution could be achieved by using a camera with more pixels per row or by decreasing the magnification, for instance. (Decreasing the magnification decreases the maximum sampling rate while keeping the number of sampling points constant thereby reducing the spacing between sampling points.) To calibrate the set-up, a ruled grating (Horiba Analytics, 400 lines/mm) was imaged. The FT returned a frequency of 398 mm^{-1} which was deemed an acceptable value and the data taken in the following sections was normalised by this value.

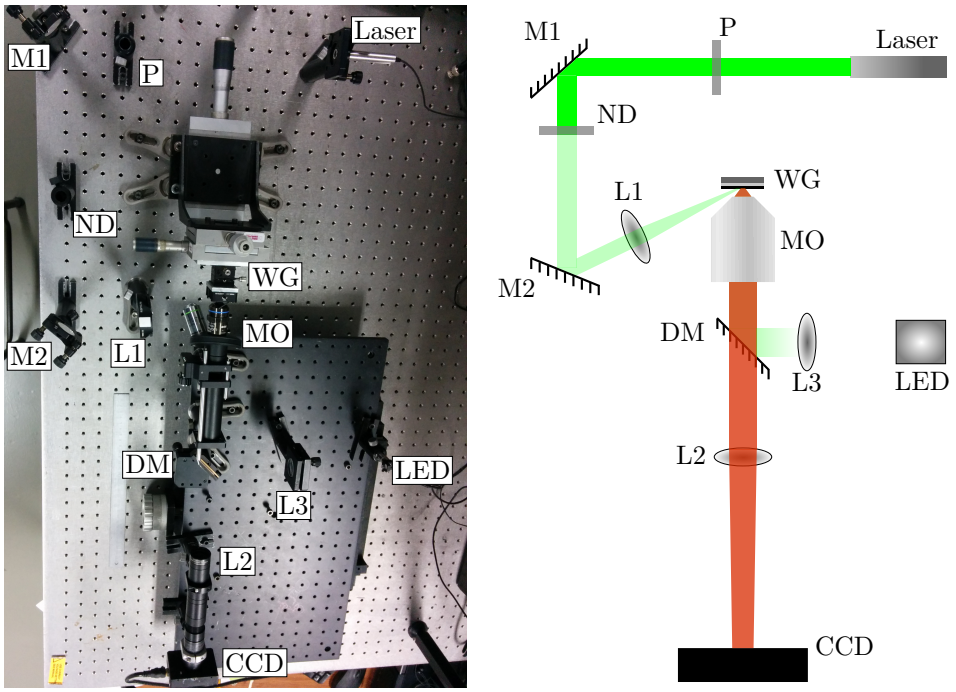

Figure 3.3 Experimental set-up for exciting and imaging modes of a waveguide. The green line shows the path of the laser through a polariser (P), a neutral density filter (ND) and focused (L1) onto the waveguide (WG). The fluorescence (red line) was collected by the microscope objective (MO) and imaged (L2) onto a CCD camera after any scattered laser light had been filtered out with a dichroic mirror (DM). The LED and lens (L3) provided brightfield illumination of the sample.

A diagram of the experimental set-up is shown in figure 3.3. The laser was end-fire coupled to the waveguides in order to excite multiple modes. The angle of incidence to the waveguide end-face was ~10° and a cylindrical lens was used for focusing. With the end-fire method, the coupling efficiency for each mode is proportional to the spatial overlap of the

input beam on the mode [71]. The cylindrical lens provided a broad input with uniform intensity across the vertical range of the camera images. This resulted in each row of pixels in every image being available as a set of data for FTs which meant signal-to-noise could be reduced by averaging over the FTs.

The microscope arm of the set-up (photograph in figure 3.3) was built on a translation stage. This meant that everything necessary for coupling could remain fixed while the imaging apparatus was free to move. This was important for the measurements related to propagation loss discussed later in this chapter.

Thinning Si_3N_4 layer

The original wafers (as received from Si-Mat) had a 400 nm thick Si_3N_4 layer. To produce a second sample with a thinner core (which would therefore have a different mode structure to the original samples) the wafers were etched. The etching process that was used was developed by a previous student of the group and was known to produce smooth surfaces. The etch was a reactive ion etch using SF_6 and CHF_3 and it was timed to remove ~100 nm of Si_3N_4. A comparison of the surface of the silicon nitride films before and after etching is given in figure 3.4.

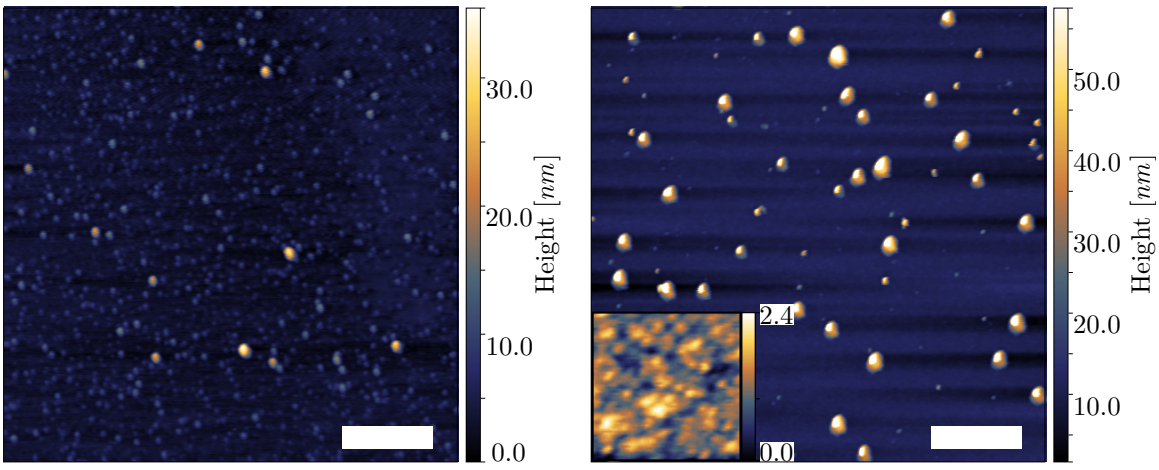

Figure 3.4 AFM scans of Si_3N_4 surfaces. (a) 5 µm × 5 µm scan of an original, unetched sample. (b) Similar scan of the same sample after etching; the inset image is a magnified view of a 400 nm × 400 nm region of the scan. The scale bar is 1 µm.

After etching, the surface roughness of the Si_3N_4 was measured using atomic force microscopy (AFM) and the film thickness was measured using ellipsometry. Figure 3.4(a) shows a 5 µm × 5 µm AFM scan of one of the samples before it was etched. Although there are some particles on the surface, the average roughness (the RMS roughness) was measured as less than 1 nm which can be expected for a film grown by LPCVD. The images in figure 3.4(b) are scans of the sample after etching. The high regions on the scan were most likely caused by contaminants on the surface during etching but the width of these

regions was overestimated as an artefact of the AFM scan. Overall the surface was still smooth (the inset image shows a 400 nm × 400 nm region) and the average surface roughness was measured as ~2 nm.

An ellipsometer was used to measure the thickness of the Si_3N_4 films after etching. (A J. A. Woollam, alpha-SE ellipsometer was used.) The tool measures reflectivity over a range of wavelengths and angles and can calculate the film thickness from these measurements. Using the software (CompleteEase) provided with the tool the thickness of the films after etching was calculated as 284 nm.

Rhodamine B

As mentioned earlier, a fluorescent dye was used in experiment to improve the imaging of the intensity at the surface of the Si_3N_4. Without using a fluorescent dye, imaging the intensity in the waveguide relies on scattered light. Scattering relies on surface roughness or sharp changes of refractive index and thus images can be dominated by particles (e.g. dust) or scratches or other imperfections on the surface of the Si_3N_4. (Imaging the scattering from pristine samples would produce similar intensity maps to the fluorescence images shown below, however, an incoherent light source would need to be used as well as a suitably high intensity. Using a coherent light source produces artefacts in the imaging.) In later chapters, the light scattered by focusing elements is imaged; the elements produce large intensities that can be imaged reliably.

By coating a fluorescent dye on the Si_3N_4, the reliance on imperfections needed for scattered images is removed and the emission from the dye is imaged. Fluorescence imaging relies on the absorption and re-emission of light by fluorophores—in this case molecules of RhB. The molecules absorb incident photons at one wavelength, promoting electrons to an excited state and as the electrons return to the ground state, they emit photons. The emitted photons are typically of longer wavelength due to the loss of vibrational and/or rotational energy as the electrons relax to the ground state and this shift in wavelength is known as the Stokes shift [147]. The Stokes shift allows for the separation of the incident and emitted light through the use of filters in the set-up thus images can be made solely of the fluorescence. Quenching and photobleaching—the reduction in fluorescence emission—of fluorophores can happen as the molecules become reactive in the excited state and change their molecular structure; however, these effects can be diminished by using low intensity excitation and short exposure times. The concentration of the dye is uniform over the surface so an image of the fluorescence maps the intensity in the waveguide. RhB was the fluorescent dye used in experiment because it could be easily dissolved/dispersed in a PVA solution and coated on Si_3N_4 and because of its optical properties some of which are shown in figure 3.5.

Figure 3.5 shows the absorption and emission spectra for RhB in solution with PVA. The spectra were normalised separately to have maximum values of 1. The wavelength of the laser (532 nm) is marked by the dotted line. In experiment, a dichroic filter is used to

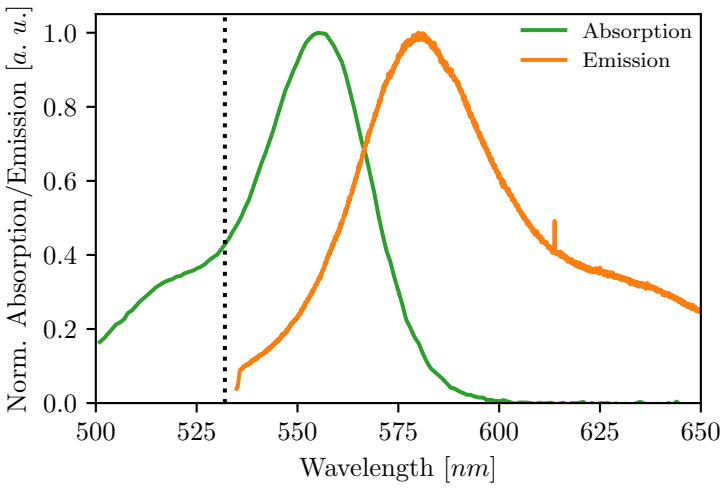

Figure 3.5 Normalised absorption and emission spectra of rhodamine B in a PVA solution. The dotted line indicates the wavelength of the laser used in experiment (532 nm). A filter, blocking wavelengths below 535 nm, was used when taking the emission spectrum.

remove any laser light from the images. This filter has its maximum reflectivity centred on 535 nm and drops below 50% reflectivity ~570 nm. This filter blocks a portion of the fluorescence but transmits enough for imaging. The emission peaks at ~580 nm which is the value that was used in calculations for the resolution of the experimental fluorescence images, however, the finite width of the emission spectrum worsens the resolution.

3.3.2 Linearly polarised, single input angle

Once light was coupled into the waveguide an image (figure 3.6(a, b)) was taken, with a dichroic mirror used to remove the green input laser, and the intensity profile (figure 3.6(c, d)) along the direction of propagation (left-to-right) was recorded. The low frequency oscillations in intensity are stable in space and time, and are due to the interference of the different waveguide modes, while any overall decay is mostly due to the absorption of the dye.

Figure 3.6(a, b) show false-colour representations of the optical images taken after the laser had been coupled to the waveguide under TM and TE polarisation, respectively (images are normalised to their own maximum value). The intensity peaks and troughs can be clearly seen, and comparing the images the TE polarised case appears to have more fine structure. For clarity, the images shown have been cropped to an area of 20 µm x 8 µm (the original images are 110 µm x 80 µm). The intensity profiles in figure 3.6(c, d) show the periodic beating pattern produced by the interference of the different modes. For a core thickness of 284 nm (circles), in both TM and TE cases, the intensity seems to vary like a single sine wave. This is the typical result for beating of two waves and suggests that, as theoretically predicted, there are only two modes supported. For the thicker core (crosses), however, in TE polarisation it is clear that the mode behaviour is more intricate.

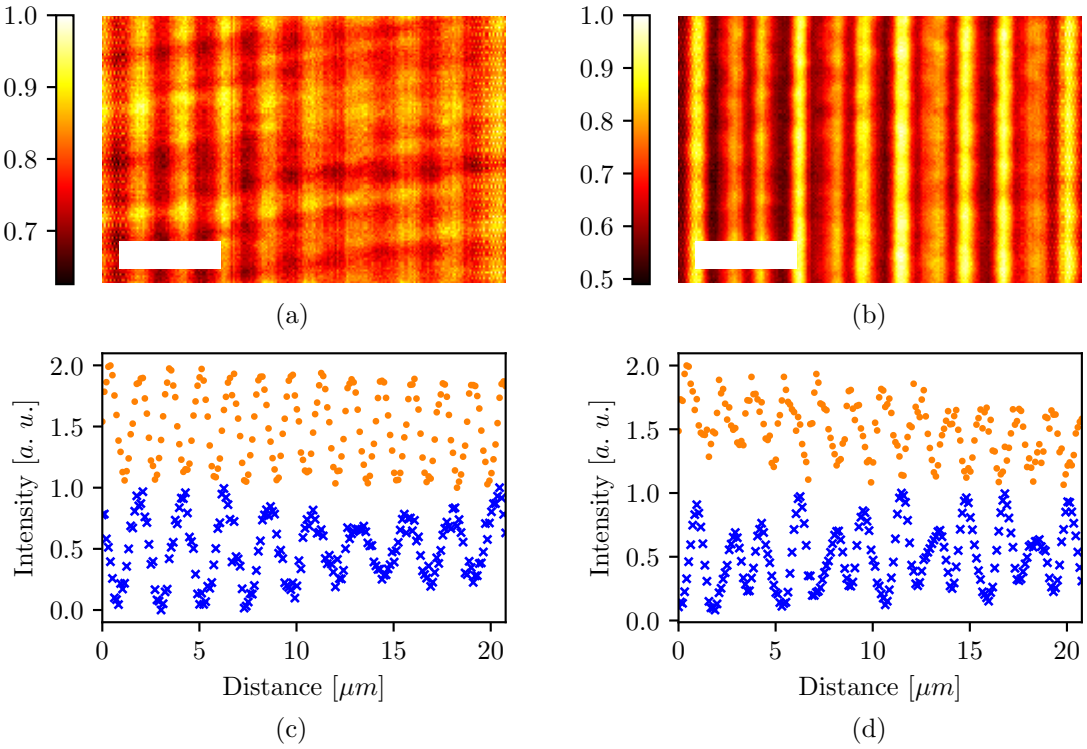

Figure 3.6 Fluorescence from a slab waveguide. (a, b) Colourmap images of the intensity of fluorescence from the dye layer coated on a slab waveguide when light is end-fire coupled (scale bar is 5 µm). The image (a) is from the 400 nm thick core with TM polarisation. The plot in (c) shows the intensity for both the 400 nm (crosses) and 284 nm (circles) thick cores. (b) and (d) show the same for TE polarisation.

Quantitative results cannot be gathered simply by eye from the images. These intensity profiles were taken for every row of pixels (768) and put through a FT using NumPy's fast Fourier transform [148]. The FTs were then averaged to produce the plots in figure 3.7.

The peaks in the Fourier spectra in figure 3.7 are the beat frequencies, f_{beat}, caused by the interference between the modes. The number of peaks, N_p, in a given spectra depends on the number of modes, m, propagating in the waveguide and is given by $N_p = m(m-1)/2$. The magnitude of a peak in the FT is directly proportional to its amplitude in the spatial domain and so the relative magnitude of the peaks can be used to compare the power coupled into each mode. That each peak is the result of a combination of two modes, and the factor of E_{exc}, need to be taken into account.

The Fourier spectra in figure 3.7 have been normalised individually to the highest peak in their curve and are plotted for frequencies up to 1.0 µm. This value covers the range of possible frequencies predicted by theory and, in experiment, no peaks were found at higher frequencies. For TE polarisation in the 400 nm thick core (plotted in (b)) there are three peaks as a result of three modes interfering. When the thinner core sample was measured, still with TE polarisation, (plotted in (d)) there is only a single peak from the interference

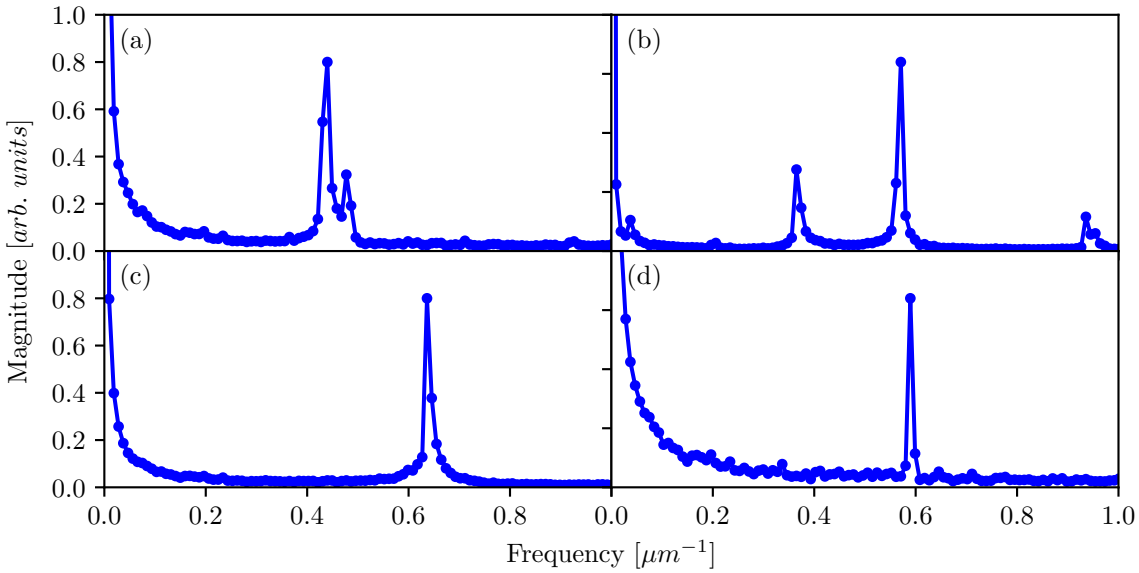

Figure 3.7 Beat frequencies in slab waveguide. Plots of FT of the intensity profiles for a 400 nm thick core in (a) TM polarisation and (b) TE polarisation, and a 284 nm thick core in (c) TM polarisation and (d) TE polarisation. The peaks are at the beat frequencies caused by the interference of modes propagating in the waveguide.

of two modes. The peak has also shifted to a higher frequency indicating the increased gap between the modes' effective indexes. For TM polarisation there is only a single peak in each curve and the frequency shift of the peak is the evidence of a change of thickness.

From the Fourier spectra the beat frequencies were found and, using (3), converted to effective index differences. The beat frequency was chosen as the frequency at which the magnitude of the FT peaked. The finite width of the peaks is mainly due to the finite resolution of the imaging system. (The decay of the oscillations caused by the dye absorption will also broaden the peaks, however, it is expected this effect is weaker than the imaging resolution.) Table 3.2 displays the beat frequencies and effective index spacings for both core thicknesses and both polarisations alongside the theoretically calculated values of effective index difference, for comparison. There is good agreement between theoretical and experimental values, with the theoretical values consistently larger than those found experimentally, suggesting perhaps that some value (e.g. film thickness, refractive index) is slightly different from the one used in theory calculations.

To determine if there was preferential coupling for a specific mode, the amplitudes of the peaks in figure 3.7(b) were compared. The lowest frequency peak, caused by the beating of modes TE_0 and TE_1, has an amplitude of 0.345. The lowest frequency peak will always be caused by the beat of the lowest order modes because they are always the closest in effective index. This can be seen as the propagation angle ($\propto n_{\text{eff}}$) needing to decrease by greater and greater amounts for the phase-matching, 'round trip' to be a whole number of wavelengths. The amplitude of the peak caused by the beating of TE_1 and TE_2 is 0.800, and by TE_0 and TE_2 is 0.145, giving a ratio of 0.43:1.0:0.18. From this, the amplitudes of

Table 3.2 Beat frequencies and effective index differences for modes in slab waveguide.

		f_{beat} (μm^{-1})	Δn_{eff}	Calculated
400 nm	TE	0.365, 0.571, 0.936	0.194, 0.304, 0.498	0.197, 0.316, 0.513
	TM	0.440	0.234	0.241
284 nm	TE	0.590	0.314	0.325
	TM	0.636	0.339	0.373

the individual modes were found and are in the ratio 0.17:1.0:0.46 for TE_0:TE_1:TE_2. (The relationship of a mode's amplitude to the amplitude of a beat was derived in section 3.2.) This ratio is for the fields exciting the dye. Normalising by the percentage of a mode's field in the dye layer (table 3.1) and converting to power in the mode, a ratio of 0.13:1.0:0.03 was found. This strong coupling to the first order mode may change by varying the angle of incidence of coupling. To expand on this measurement and determine how the power in each mode relative to the others varied with propagation distance the experiment described below was performed.

3.3.3 Propagation length

The measurements discussed above were taken close to the "in-coupling" end of the waveguide. For comparison, images were taken at different positions along the waveguide (~0.25 mm separations). As before, a laser was coupled in with TE polarisation. The microscope was then moved along the waveguide, away from the in-coupling region. Images similar to those in figure 3.6(a, b) were taken at successive distances along the waveguide and the FT of the intensity was taken for each of the different images. Three of the resulting Fourier spectra, for images taken ~1 mm apart, are shown in figure 3.8. The data is presented on a log scale so that the higher frequency peaks remain clear. The scatter plot compares, also on log scale, the relative power of each mode when normalised by the sum of the powers in the three modes. The fitted lines are of the form $10^{-\alpha d}$ with α representing decay length for the mode. The total power in the waveguide is found by averaging the intensity over a consistent portion of each image, and can be seen in figure 3.8.

The FT taken near the beginning of the waveguide—the dashed line in figure 3.8(a)—shows three peaks resulting from interference between the three modes. The peak at 0.57 μm^{-1} is the strongest. Moving along the direction of propagation by 1 mm (dotted line) the relative magnitudes of the peaks has changed so that the peaks caused by interference of the second order mode with the other two have diminished. Moving further along the waveguide (solid line) the second and third peaks have become weaker still. Monitoring the change in amplitude of the Fourier peaks as a function of distance we can extract the relative losses in each mode. The scatter plot in figure 3.8(b) shows the propagation losses of the individual modes as well as the normalised relative power in the waveguide. The first

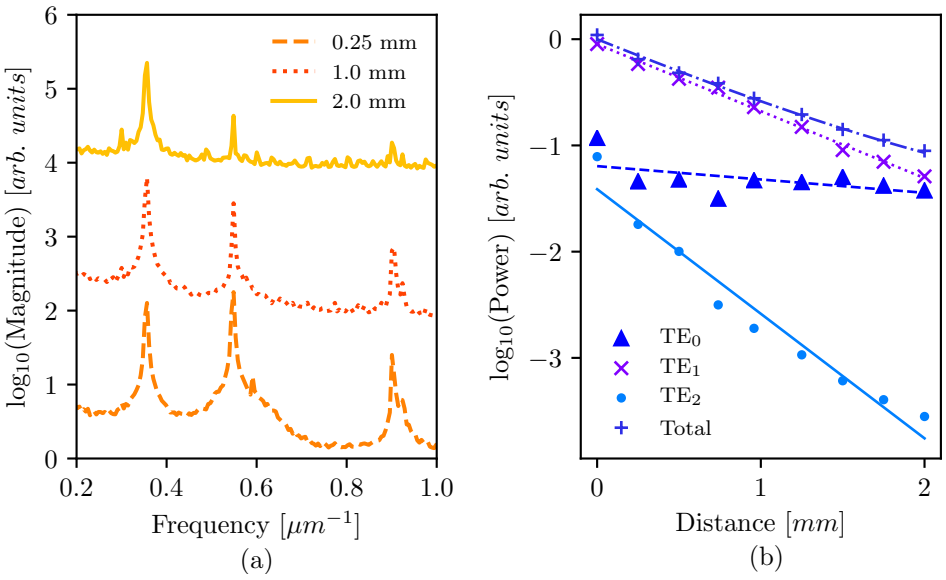

Figure 3.8 Relative propagation losses. (a) Fourier transform taken at different positions along the length of the waveguide with the peaks relying on the second order mode becoming weaker with distance. (b) Plot of the power in each mode relative to the power in the waveguide.

order mode is coupled to most strongly while the fundamental and second orders contain significantly less of the propagating power in the beginning. Due to their greater overlap with the dye layer, the TE_1 and TE_2 modes lose more power exciting the dye. After a short distance the TE_2 mode has diminished to a power noticeably lower than the TE_0 mode while at around 2 mm distance the TE_1 has similar power to TE_0. The total power at each position is then used to determine the loss of the different modes. To find these losses, the logarithm of the power was plotted against propagation distance (see figure 3.8). It can be seen that the power in the TE_1 mode reduces to about one-tenth of its initial value after 2 mm corresponding to losses of ~50 $\mathrm{dB\,cm^{-1}}$. Fitting the plots in figure 3.8(b), the slope of the fitted line is equal to the propagation loss of the mode and (after converting units) losses of 12.6 $\mathrm{dB\,cm^{-1}}$, 63.0 $\mathrm{dB\,cm^{-1}}$ and 117 $\mathrm{dB\,cm^{-1}}$ for TE_0, TE_1 and TE_2 were found. These losses are quite high compared to reported measurements of propagation loss in Si_3N_4 waveguides [111, 126]. These losses can be partly attributed to absorption by the dye. For comparison with analytical calculations, a suitable value of 0.001 as the imaginary component of the dye's refractive index (suitable for this concentration of dye) results in losses of 11.5 $\mathrm{dB\,cm^{-1}}$, 54.7 $\mathrm{dB\,cm^{-1}}$ and 123.6 $\mathrm{dB\,cm^{-1}}$. While there are more accurate measurements of single mode propagation loss, e.g. cut-back method, this provides a non-destructive measure of the loss for co-propagating modes relative to one another.

3.3.4 Circularly polarised, single input angle

To broaden the scope of the method, measurements of mode beating in the waveguide with circularly polarised input were made. Like before, the experiment was set up as shown in figure 3.3 but with the addition of a quarter-wave plate. The wave plate (with fast axis at 45° to the beam's polarisation) was inserted between the linear polariser and mirror (M2). This ensured equal amounts of TE and TM polarisation were incident on the waveguide and suggested all the modes supported by the waveguide would be coupled to and propagate simultaneously through the waveguide. As the field in the waveguide is a superposition of the TE and TM modes (the field is generally elliptically polarised) any interference effects can be seen as a superposition of TE modes interfering and TM modes interfering. This arises from the orthogonality of the polarisations (Fresnel-Arago laws) and means that the resulting intensity patterns are effectively those of the TE case overlaid with those of the TM case (i.e. there are no additional interference peaks in the FT) and contain separable information about the TE and TM modes.

As before, the fluorescence images (figure 3.9(a) and (b)) show the interference caused by the beating of the modes propagating in the waveguide. By eye it is difficult to identify any differences from the linearly polarised cases shown earlier (see figure 3.6(a) and (b)) and it is in the FTs that the expected results are verified. The intensity profiles from these images were put through a FT as described for previous measurements and then compared with the earlier results. Figure 3.9(c) and (d) plot the FT for circularly polarised input (solid line) for the 284 nm and 400 nm thick cores, respectively; in both cases, there are more peaks than in the linearly polarised measurements. For ease of comparison, the TE and TM cases are overlaid as dotted and dashed lines, respectively. It is clear that the solid line is a simple combination of the broken lines demonstrating, as expected, that there is no interference between the TE and TM modes since there are no new peaks. This also shows that a measurement with unpolarised input is enough to determine mode spacings when there are a small number of modes. However, as the number of modes propagating increases, the likelihood for peaks (of separate polarisations) to overlap increases making it more reliable to use polarised input.

A note on the FT magnitudes in the circularly polarised case. Each of the curves was normalised by a different value since the aim was only to show that no additional peaks arise when using circularly polarised input. However, quantitative results can be found by examining the solid curve alone. Comparing the contributions of TE and TM to the solid curve in figure 3.9(c), it can be seen that the peak for TE interference is stronger (~3× the TM peak) while in (d) the peak for TM interference is strongest (~2× the TE peaks). Since equal amounts of TE and TM polarised light were incident on the waveguide for the two thicknesses (with the angle of incidence unchanged) it suggests that this is not a preferential excitation of the dye by either polarisation and is more likely a preferential coupling depending on the mode's properties. This led to experiments with varying incident angle described below.

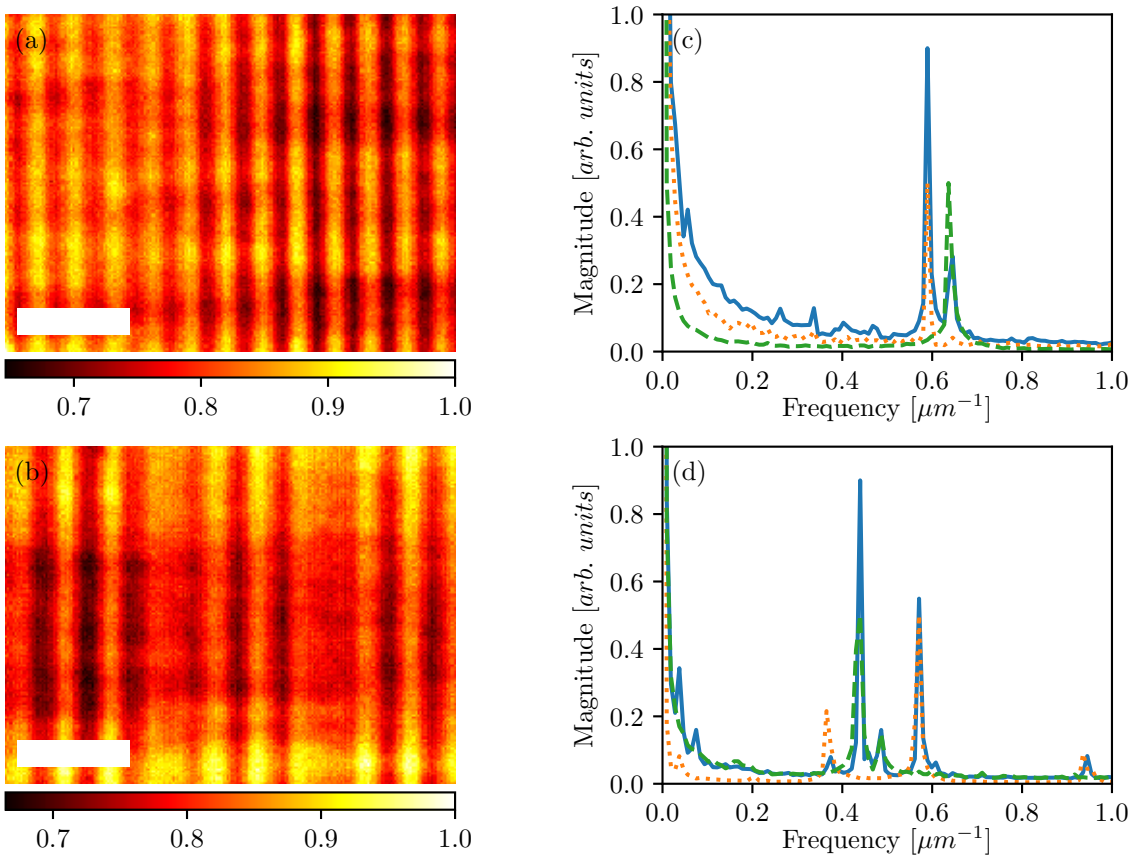

Figure 3.9 Images and FTs for circularly polarised input. (a) Fluorescence heatmap produced when circularly polarised light is coupled into a 284 nm thick core (scale bar is 5 µm). (c) Plot of FTs comparing circularly polarised (taken from (a)) to linearly polarised (from earlier measurements). The solid curve is for circular polarisation while the dashed and dotted are for TE and TM, respectively. (b) and (d) show the same measurements for a 400 nm thick core.

3.3.5 Varied angle coupling

To determine if there was any control over mode specific coupling a run of measurements was performed where the input angle of the beam to the waveguide was varied. With the set-up as shown in figure 3.3 the mirror M2 was moved ("vertically" in the figure) to change the incident angle of the beam; lens L1 was then repositioned to focus the beam. For this experiment only the 400 nm thick core was used. Considering error in the measurement of the incident angle and the small spread introduced by the focusing lens meant that nominal values of 10°, 18° and 23° were taken. The range of input angles available was limited at lower angles by the beam spreading (due to its finite width) over the superstrate of the waveguide and exciting fluorescence; at larger angles the microscope objective would block the beam reaching the waveguide. For these measurements linearly polarised input was again used and the results are shown in figure 3.10.

The plots in figure 3.10 seem to indicate that the coupling does not vary greatly with

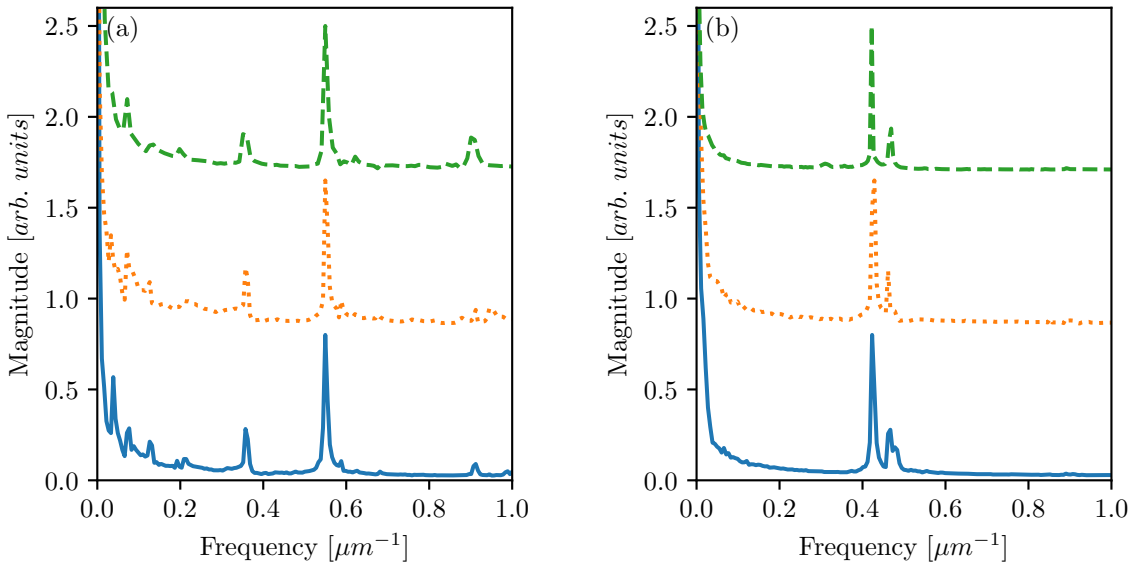

Figure 3.10 Mode coupling with input angle. (a) Graph of FT with TE polarisation for different input angles: 23° (solid), 18° (dotted) and 10° (dashed). (b) The same for TM polarisation. The curves have been offset from each other for clarity.

input angle. Each curve has been normalised to its highest peak so relative peak heights should be compared rather than absolute values. The TE polarised case is plotted in (a) and shows that there is not a large change over the range of angles as, similar to earlier measurements, the '2-3' peak is the strongest for each angle. However, it can be seen that the '1-2' and '1-3' peaks vary relative to each other over the three curves. It might be expected that over this range of angles the TE_1 mode would be coupled to moreso than the fundamental TE mode—reflections from the substrate and base Si wafer would alter the field at the waveguide end-face. To couple more strongly to the fundamental mode it might be necessary to move to lower input angles.

3.4 Conclusions

An experimental method for determining the difference between the effective indexes of different modes propagating simultaneously in a dielectric slab waveguide was demonstrated. It was shown that copropagating modes in a waveguide interfere because of the different optical path lengths arising from the modes' different effective indexes. The interference produces a standing wave—a corrugated intensity profile that is constant over time. Although beats in waves are generally travelling waves, the fixed relative phase between the modes at input is what causes the standing wave. The period of the standing wave is controlled by the effective index difference of the modes interfering and a desired profile could be achieved by varying the wavelength of light used. The ability to control the electric field profile along a planar optical structure in this way could prove useful in optical trapping and manipulation [125].

Since the intensity profile is constant in time it can be imaged and information of the underlying mode structure can then be extracted from the images. By imaging the fluorescence from a dye-doped PVA film spin coated on the core of the waveguide, the intensity in the waveguide was spatially mapped. Using a Fourier transform the intensity profiles were converted to spatial frequencies which were used to calculate the effective index difference between the modes. The experimentally determined values matched well with those analytically calculated—in all but one case the difference was <5%. The deviation between the theoretically and experimentally calculated values is most likely due to the thickness of the dye-doped PVA film varying between samples.

Aspects of mode propagation and coupling were also measured. The propagation losses of the different order TE modes were measured and showed that the lower the order of the mode the lower the loss. This would be expected as losses would be dominated by surface scattering (and in this set-up dye absorption) and the higher order modes have a greater fraction of their fields near the surfaces (and outside the core layer). The variation of mode excitation with input angle was also looked at, though over the range of angles considered was not found to vary greatly.

The advantages of this method lie in its ease of application and analysis, using inexpensive equipment. The non-destructive nature of the method is also worth noting as the dye layer can be easily removed after testing. Also, the dye layer is not absolutely necessary but was used here to improve imaging the intensity at the surface of the waveguide core. Images of the scattered light would also contain the same information, provided the surface was uniform with a small surface roughness. The method can be extended to rib waveguides, specifically in cases of bends and tapering, where different modes are affected differently. Ideally, this would be done with controlled input coupling.

When orthogonally polarised modes (i.e. TE and TM) propagate simultaneously, the resultant field is elliptically polarised in space. In time, however, the polarisation of the field depends on the position; in general, the beam is elliptically polarised but at positions where the TE and TM modes are in-phase, the resultant field is linearly polarised. (This is different from the general free space case where a polarisation state is the same in both time and space.) Because of this effect, the polarisation state of the radiated field depends on the position at which the waveguide is terminated and will also vary between linearly and elliptically polarised. The effect of the radiated intensity varying with termination position was previously demonstrated and measured by Gut [149].

4 Rectangular waveguide structures

In the previous chapter, it was shown that information about the propagating modes can be attained from simply imaging the intensity at one surface of a slab waveguide. To demonstrate how this measurement could be used in other systems, different waveguide structures were fabricated. In this chapter, the propagation of light in rectangular waveguides, around bends and along tapers is studied. As in the previous chapter, the interference of modes can be seen but in these structures a greater number of modes is supported and their effective index differences are often minuscule, making quantitative measurements challenging. However, the effects of different perturbations on the modes are clear and a few cases are shown.

4.1 Introduction

The use of dielectric waveguides in integrated optics (IO) was covered in depth in chapter 1. For IO circuits to be compact, bends in the waveguides connecting the elements are a necessity and thus have been the subject of much research. Low-loss bends with small bend radii have been demonstrated in SOI platforms (~0.01 dB per bend for a 2 µm bend radius [150]) and unconventional structures have been proposed to achieve tight bending on other platforms, e.g. incorporating plasmonic elements into the bend [151]. However, these structures are generally designed and tested for single mode waveguides. The propagation of higher order modes is often not considered but for IO circuits to be optimised multiple modes of a waveguide need to be used.

To theoretically study waveguide bends, analyses such as the beam propagation method and transformation optics (TO) have been used [152, 153]. Using TO a 90° bend (radius ~80 µm) which supported three modes with negligible intermodal coupling was designed and experimentally measured. TO can be used to predict suitable designs for many structures but they can require elaborate fabrication.

Measurements of waveguide bend performance generally rely on just transmission measurements; the insertion losses are measured for similar systems with an increasing number

of bends and from the total losses the bend losses can be deduced. Direct imaging of the bends, when performed, is usually carried out by scanning the optical near field [92, 154, 155]. These technniques (NSOM and PSTM) provide high resolution of the intensity as the modes propagate through the waveguide but they can be cumbersome. Far field optical measurements are less common but can visualise the same information (with reduced resolution) [83]. These measurements can be used to determine how different modes are perturbed by a bend in the waveguide core (or any structural change to the waveguide core).

Rectangular waveguides and bends and tapers in rectangular waveguides are investigated through far field imaging in the following sections. The structures presented support multiple modes and, in some cases, information can be extracted from the interference of the modes. The tapered waveguides are studied as simple focusing elements and far field images show clearly how effective different tapers can be for focusing light to a spot. Numerical simulations are given for certain cases to support experimental observations and also to provide insight into the processes of the individual modes (in contrast to the multi-mode experimental images).

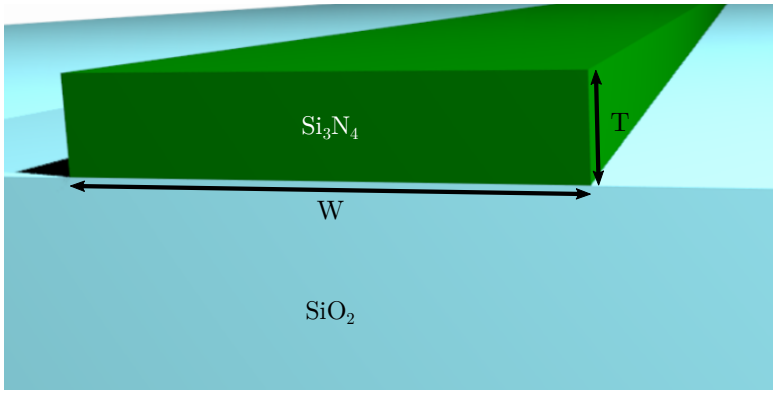

Figure 4.1 Cross section of a rectangular waveguide. The thickness (T) and the width (W) of the core vary between samples. The core, substrate and other layers (not shown here) are the same as in the previous chapter.

The geometry of the waveguides used in this chapter is shown in figure 4.1. The width of the core was kept in the range 1–10 µm and thicknesses of 180 nm and 400 nm were used. The materials of each layer were the same as in the previous chapter. The structures presented in this chapter were fabricated using electron beam lithography (EBL) and an inductively coupled plasma (ICP) etch. A negative tone resist (nLOF) was used in EBL to define the etch mask. The methods used for fabrication were presented by a previous student of the group [156]. Optical and scanning electron microscopy (SEM) images of the different waveguide structures (bends, tapers) are shown in later sections. As before, a film of RhB doped PVA was coated over the surface to improve imaging measurements.

4.2 Modal interference in rectangular waveguides

The interference of slab waveguide modes was studied in the previous chapter and it was shown that the intensity pattern produced by simultaneously propagating modes contains information about the individual modes. In rectangular waveguides the same effects occur and so similar information can be extracted. However, rectangular waveguides support many more modes than a slab waveguide of similar thickness; the 'extra' modes are closer in effective index which makes definitive measurements more difficult. As an example, rectangular waveguides with different core widths were measured.

The end-fire method was used to couple light ($\lambda = 532\,\text{nm}$) into the waveguides. The fluorescence of the PVA-RhB film was imaged using the set-up shown in figure 3.3 with a dichroic mirror preventing laser light from reaching the CCD camera. With the optical elements used the resolution was ~600 nm and the effective pixel size was ~105 nm. Experimental images of a set of waveguides with different widths are shown in figure 4.2. Similarly to the modes of a slab waveguide, rectangular waveguides have an order relating to the number of nodes in the electromagnetic field profiles. Since rectangular waveguide modes can have nodes in both transverse directions, the modes have a double subscript, i.e., TE_{ij} and TM_{ij}, where i is the order in the smaller dimension (in this case the thickness) and j is the order in the larger (the width). As stated in chapter 2, rectangular waveguide modes are not purely TE or TM but for widths $\gtrsim 1\,\mu\text{m}$ they are well approximated as TE and TM.

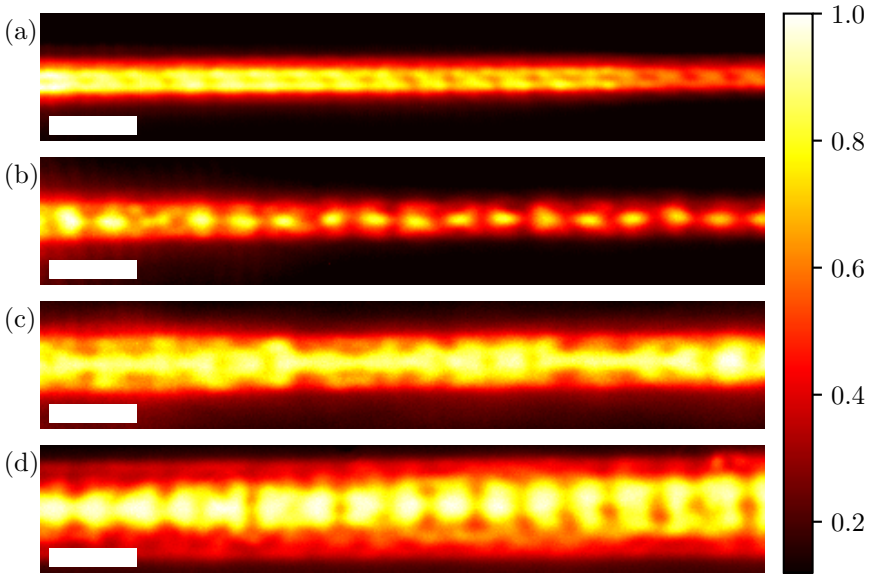

Figure 4.2 Experimental intensity maps of light propagating in rectangular waveguides. The width of the core is (a) 1 µm, (b) 2 µm, (c) 3 µm and (d) 5 µm. The scale bar is 5 µm.

The images in figure 4.2 experimentally map the intensity along waveguides of different core widths. (For these images the input was TE polarised). The thickness of the core

is 400 nm and the width is varied from 1 µm to 5 µm. The intensity varies both across and along the direction of propagation (left to right). The greater propagation loss in the waveguides with smaller cores is due to a larger fraction of the power in these waveguides being outside the core thus being absorbed by the dye.

As the width of the waveguide increases, the number of modes supported by the waveguide increases and if these modes are excited, the intensity pattern becomes more intricate. The variation of intensity can be separated into oscillations due to different order modes in the thickness and a changing profile due to different order modes in the width. The modes of different order in the thickness have effective index differences similar to those in the previous chapter while the modes of different order in the width have much smaller effective index differences. As in the previous chapter, the Fourier transform (FT) of the intensity along the waveguide was calculated using NumPy the results of which are shown in figure 4.3.

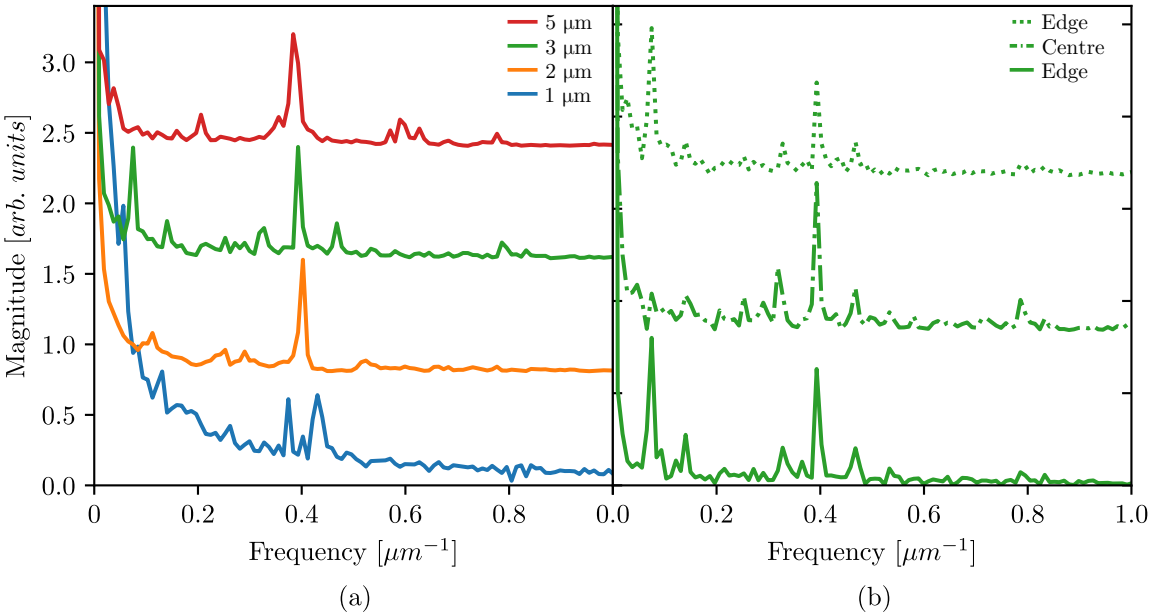

Figure 4.3 Fourier transforms of the intensity profiles along waveguides of different core width. (a) Fourier transforms of the waveguides shown in figure 4.2. (b) Fourier transforms taken at different positions of the 2 µm core waveguide.

The curves in figure 4.3(a) are the FTs of the waveguides shown in figure 4.2. For each waveguide, a FT was taken along each row of pixels of the core and the average of these FTs is plotted. Each FT has a peak near 0.4 μm^{-1} and the peak is shifted towards lower frequencies as the width of the waveguide increases. This peak is a result of the interference between the TE_{0j} and TE_{1j} modes. The splitting of the peak in the FT for the 1 µm core is from excitation of TE and TM modes; for a core of this width, the modes have electric field components along both axes and are not distinctly TE or TM. The modes of the waveguides were found theoretically using the finite-difference eigenmode solver in Lumerical's MODE solutions (described in chapter 2). The wider waveguides support tens

of modes in the width which are not all listed here, instead the lower order TE modes of each waveguide are listed in table 4.1. It can be seen that the effective index difference between the modes increases as the width of the core decreases. This corresponds to the experimentally measured increase in the beat frequency with decreasing core width. One other correlation between simulations and the experimental measurements is the reduction in the number of peaks in the FT as the width of the core is decreased, as fewer modes are supported. Ultimately, the number of modes supported by the waveguide made quantitative measurements of the modes quite difficult.

Table 4.1 Numerically calculated effective indexes (n_{eff}) of the low order $\text{TE}_{i,j}$ modes of a rectangular waveguide. The thickness of the waveguide core was 400 nm and the width (w_{core}) varied from 1 µm to 5 µm.

w_{core} [µm]	n_{eff}			
	Order (i)\Order (j)	0	1	2
5	0	1.985	1.983	1.979
	1	1.787	1.785	1.781
	2	1.472		
3	0	1.984	1.973	1.960
	1	1.785	1.775	1.758
	2	1.469		
2	0	1.981	1.969	1.948
	1	1.783	1.770	1.747
	2	1.467		
1	0	1.970	1.923	1.846
	1	1.771	1.720	1.634

Averaging the FTs across the waveguide core can improve the signal-to-noise ratio of the data but it removes the dependence of position. In figure 4.3(b), the FT taken for different rows of the same waveguide core are plotted. A FT was taken for a row of pixels near to the top edge of the core of the waveguide shown in figure 4.2(c)—the 3 µm wide core—as well as along the centre and along the bottom edge of the core. Each of the FTs contains the peak at 0.4 µm, however, there are differences between the FT for the centre and those for the edges. The clearest difference is the peak at ~0.08 μm^{-1} which is missing in the FT for the centre. This low frequency interference is from modes of different order in the width (i.e. TE_{0j} and $\text{TE}_{0j'}$. Another, less striking, difference is the emergence of a peak at 0.8 μm^{-1} in the FT for the centre. This peak would correspond to modes with a large effective index difference (likely TE_{0j} and $\text{TE}_{2j'}$). As before, these measurements were inhibited by the number and density (in effective index) of the modes supported by these waveguides. While

increasing the resolution and magnification would be an improvement, the measurement would perhaps be best suited to low index contrast waveguides which support only a few modes even for relatively large cores.

4.3 Bends

As mentioned earlier, waveguide bends are necessary components for IO circuits and they have been studied theoretically and with near-field scanning optical microscopy (NSOM) imaging. Direct imaging generally provides the greatest insight into light propagation through a structure; even though transmission measurements (where just the power at the input and output are recorded) can determine the loss of a structure, they do not contain any information on how the modes are perturbed. Here, a number of waveguide bends with different bend radius are examined through the intensity mapping technique used for rectangular waveguides, above. Microscope images of a group of bends fabricated by EBL and ICP etching are shown in figure 4.4.

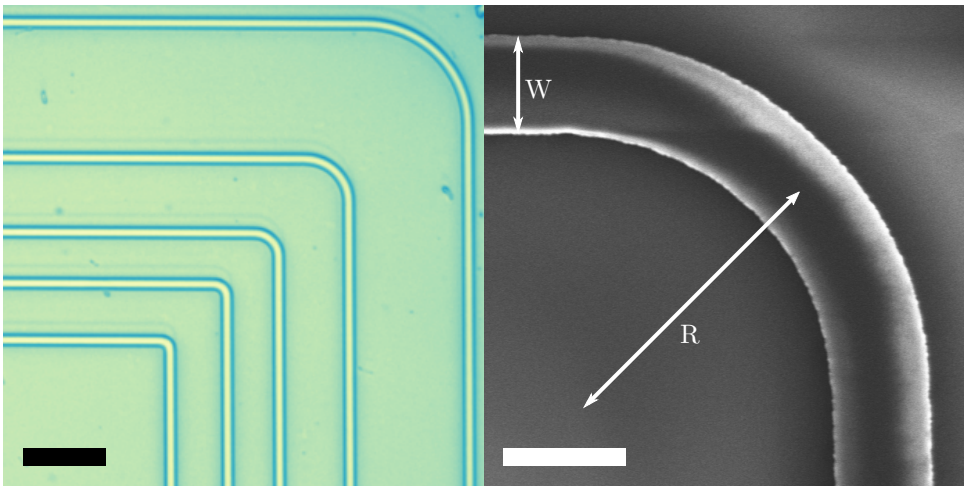

Figure 4.4 Microscope images of bends in dielectric waveguides. (a) Optical image of a set of bends with radius of curvature 1–25 µm and a core width of 2 µm. (The scale bar is 20 µm.) (b) SEM image of a bend of radius (R) 5 µm and width (W) 2 µm. (The scale bar is 2 µm.)

The image in figure 4.4(a) is of a set of waveguide bends, each with a core thickness of 400 nm and a width of 2 µm. The radii of curvature of the bends are 1, 2, 5, 10 and 25 µm. These are sharp bends for dielectric waveguides with a core refractive index ~2 but were chosen as they would demonstrate very clearly the effects of changing the radius of curvature. In figure 4.4(b), an SEM image of the 5 µm bend from (a) is shown. The width (W) of the core and the radius of curvature (R) of the bend are marked. The radius of curvature is chosen as the average of the inner and outer radii of the core. Measurements of the bends were made using the same method described above.

4.3.1 Varying bend radius

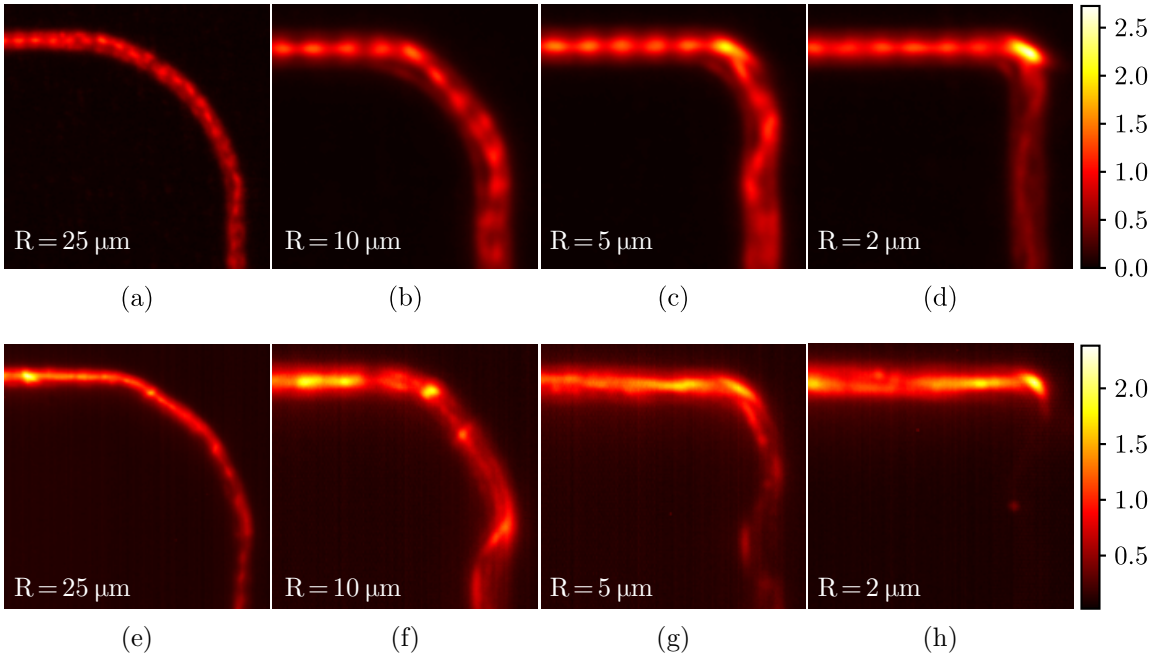

Figure 4.5 Experimental intensity maps of bends in 2 µm wide waveguide cores. The radius of the bends range from 2 µm to 25 µm. The images shown in (a)–(d) are of waveguides with core thickness 400 nm; those in (e)–(f) have a thickness of 180 nm. The intensity is normalised to the intensity in the core before the bend.

Experimental measured intensity maps of modes propagating around bends in a waveguide core are shown in figure 4.5. The width of the core is 2 µm and the bend radius (R) varies from 2–25 µm. The thickness of the core is 400 nm for figure 4.5(a)–(d) and 180 nm for (e)–(f). Light was coupled into the waveguides by the end-fire method, exciting multiple modes. The modes propagate from the top-left corner to the bottom-right. For each image the intensity is normalised such that the intensity at the beginning of the bend is 1. This was done so that the power lost over each bend could be compared.

Although there are multiple modes propagating before the bend in both the 400 nm core and the 180 nm core, the overall effect of the bend on the individual modes is clearer for the thicker core. In figure 4.5(a)–(d), the input to the bends is symmetric across the core and makes a steady beating pattern before the bend. As the modes traverse the bend it can be seen that this symmetry is lost as the changing refractive index profile (i.e. the bend) induces intermodal coupling. (The magnitude of this intermodal coupling is different for each mode and a simulated intensity map for individual modes traversing a bend is shown in figure 4.6.) The effect of intermodal coupling is least strong in the 25 µm bend, though it is still evident; the 10 µm and 5 µm radius bends demonstrate it more clearly, while the 2 µm bend is too sharp and acts almost as a mirror. The intensity maps for the same core width in the 180 nm thick sample match each other well with the paths traced by the modes

overlapping for the different thicknesses (apart from the increased loss for the thinner core which is expected). In an effort to distinguish the modes from each other, the propagation of individual modes around a waveguide bend were simulated.

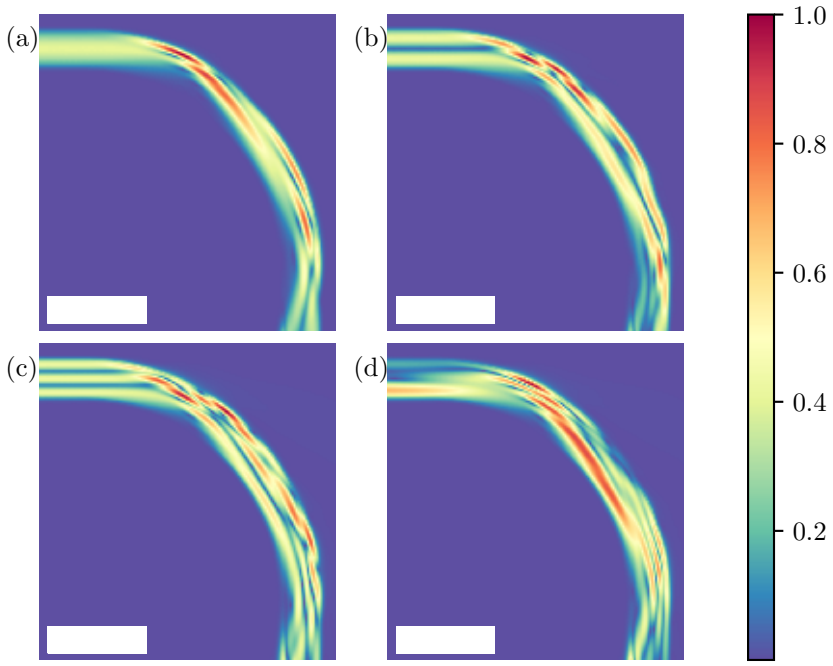

Figure 4.6 FDTD simulated intensity maps for different order modes in a waveguide bend with a radius of 10 µm. The width of the core is 2 µm and the thickness is 180 nm. The TE_{00}, TE_{01} and TE_{02} are the input mode in (a), (b) and (c), respectively. (d) The intensity when TE_{00}, TE_{01} and TE_{02} are input simultaneously. The images are normalised such that the input power is constant. The scale bar is 5 µm.

In figure 4.6, intensity maps simulated for the TE_{00}, TE_{01} and TE_{02} modes as the input to a bend of radius 10 µm are shown. The thickness of the core was 180 nm. The images in (a)–(c) are intensity maps when only a single mode is input, while in (d) the simultaneous propagation of all three modes is simulated. (In these images the intensity is normalised such that the input power is constant; this was chosen to help comparison between the single mode and multi-mode simulation.) The simulations show clearly how the power from a single mode input is redistributed into other modes as it traverses the bend. Although the intensity distribution around the bend is quite similar for the different modes, the output from the bend is not. It is the output from the bend that ultimately shows the intermodal coupling, and this new distribution of modes becomes the input for the next section of the waveguide. The intensity map for multi-mode propagation in figure 4.6(d) is shown for comparison with the experimental images in figure 4.5(f). In the experimental measurement it is expected that more than three modes were propagating before the bend but there is a reasonable overlap of the experimental intensity map and the simulated intensity map for the fundamental TE mode.

Using single mode coupling the effect of a bend on the individual modes could be more clearly demonstrated in experiment. While the effects of a bend on the modes of a waveguide can be clearly seen in the experimental images in figure 4.5, investigating each mode separately would simplify the analysis of how the bend perturbs a given mode.

4.4 Tapers

Tapering the width of the core of a waveguide provides a simple method of mode focusing. Similarly to the bend, if the taper angle is too sharp then the sudden change of refractive index profile will cause scattering of the modes. Using a small taper angle to avoid this is termed *adiabatic* tapering since it maintains the power within a single mode in the core as the width of the waveguide gradually decreases. As the aim of this project was to demonstrate a micrometre scale focusing element, the tapers here are kept relatively short and the shorter ones exhibit the effects of non-adiabatic tapering. A set of tapers fabricated by EBL and ICP etching are shown in the optical microscope image in figure 4.7(a). The lengths of the tapers are 5 µm, 10 µm, 20 µm and 50 µm. The width of the core is 5 µm and the thickness is 400 nm. An SEM image of the 5 µm long taper is shown in figure 4.7(b); it can be seen that the taper does not narrow to a point but has a slightly rounded end. Other tapers might have flattened ends with widths of tens of nanometres and although it will be seen that the finite tip radius was not an issue for this taper, for more gradual tapers the definition/resolution of the end-point is important.

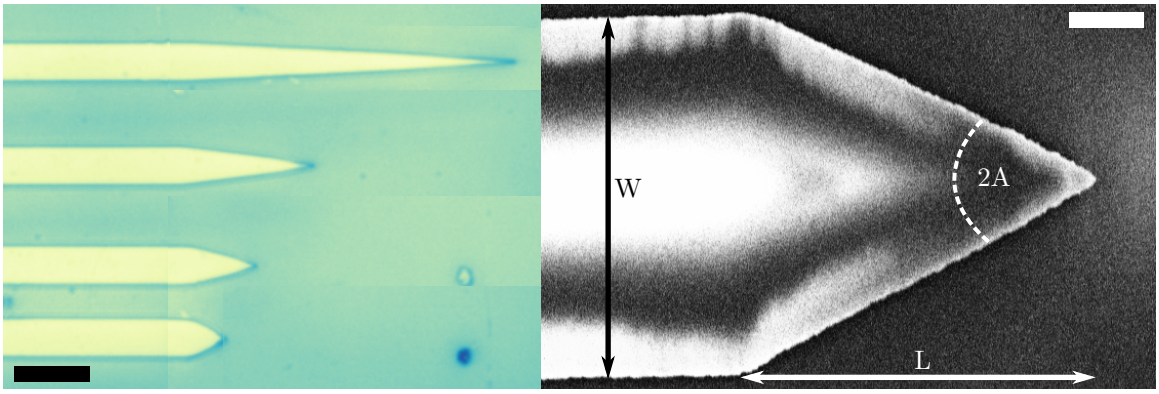

(a) (b)

Figure 4.7 Microscope images of waveguide tapers. (a) Optical image of a group of four tapers of varying length and constant initial width. The scale bar is 10 µm. (b) SEM image of a taper with a length (L) of 5 µm and an initial width (W) of 5 µm. The taper angle (A) is also marked. The scale bar is 1 µm.

4.4.1 Varying taper angle

To demonstrate the focusing characteristics of tapers, a set of measurements which studied the effects of varying the taper angle is described. For these measurements, the tapers that were shown in figure 4.7(a) were used (as well as one longer taper, 100 µm). Again, light was coupled into the waveguide by end-fire and the fluorescence of the RhB dye was imaged onto a CCD camera. The experimental images are shown in figure 4.8.

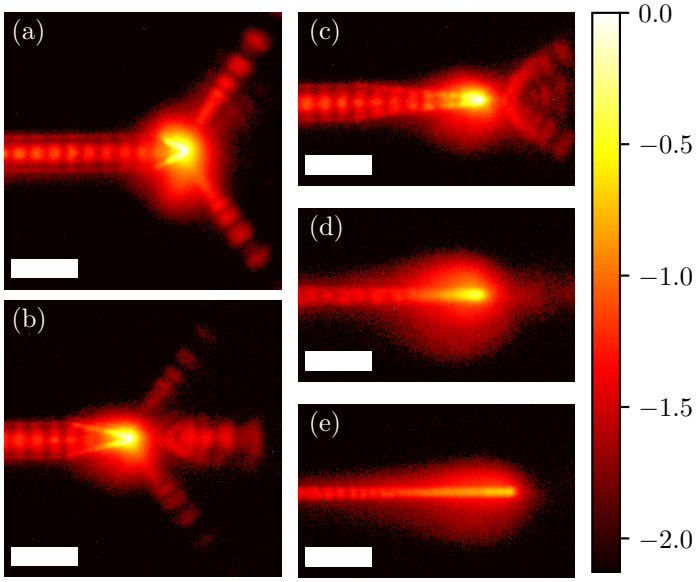

Figure 4.8 Experimental intensity maps of waveguide tapers. The length of the taper is 5 µm, 10 µm, 20 µm, 50 µm, 100 µm in (a)–(e), respectively. (Only the end-points of the tapers are shown in (d) and (e). The intensity is plotted on a log scale and each image is normalised separately. The scale bar is 10 µm.

The intensity maps in figure 4.8 show how the propagating modes of a waveguide are focused by tapers of different taper angle. The intensities have been plotted on a log scale so that all of the information is visible. In figure 4.8(a) and (b), the effects of tapering the waveguide core too sharply can be seen; light is scattered at high angles out from the core before reaching the end of the taper. The 5 µm long taper in (a) radiates only at large angles (~60°) to the waveguide axis while the 10 µm taper radiates a noticeable amount directly forward. The longer tapers in figure 4.8(c)–(e) (20 µm, 50 µm and 100 µm, respectively) do not exhibit any high angle scattering. Although there is light radiating from the taper in (c), the modes have been focused to the end of the taper. As expected focusing/confinement of the modes was achieved best by the longest tapers. For the tapers in (d) and (e), there is no noticeable scattering or radiation out of the waveguide; there is some loss due to absorption by the fluorescent dye. As the width of the core decreases below the size of the wavelength in the core (~260 nm) the modes become less confined to the core and more of the power is in the cladding material. While the tapers in (d) and (e) exhibit efficient mode focusing their size does not match with the design parameters imposed earlier.

To verify that the high angle scattering in figure 4.8(a) and (b) is due solely to the sharp tapering and not the result of sidewall roughness or high order modes being present, these tapers were simulated.

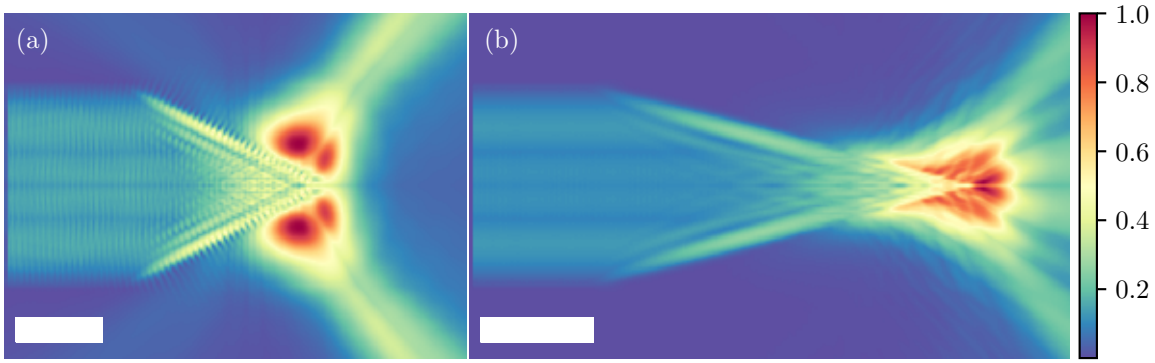

Figure 4.9 Simulated intensity maps of waveguide tapers for TE_{00}, TE_{01} and TE_{02} modes as the input. (a) 5 µm long taper with a starting width of 5 µm. (a) 10 µm long taper with a starting width of 5 µm. The scale bar is 3 µm. The intensities were normalised separately.

The inputs for the simulations were the TE_{00}, TE_{01} and TE_{02} modes and the intensity maps in figure 4.9 shows the combination of these modes. Due to the resolution of the simulations, the diffraction of the modes by the tapers can be seen. The 5 µm long taper in figure 4.9(a) shows excellent agreement with the experimental image; the modes are scattered out of the waveguide at high angles before reaching the end of the taper. The simulated intensity for the 10 µm taper in (b) shows that the modes do reach the end of the taper before being radiated both directly forward and at an angle to the waveguide axis. This matches some of what was seen in experiment for the 10 µm taper and the scattering at higher angles may have been produced by higher order modes. The simulations reinforce the expectation that micrometre scale tapers cause undesirable diffraction and as such do not focus waveguide modes sufficiently well.

4.5 Conclusions

In this chapter, the application of fluorescence imaging to understand multi-mode propagation in rectangular waveguides was discussed. In particular, waveguides of different width, waveguide bends and focusing tapers were investigated.

It was shown that fluorescence imaging is a viable method for examining propagation in rectangular waveguides, and the effective index differences and losses of individual modes could be extracted for narrow waveguides. With wider waveguides, however, it was not possible to quantify each of the modes individually due to the large number of modes supported by the waveguide. It is suggested that these measurements would be best suited to low index contrast waveguides which do not support many guided modes even at large core sizes. Fourier transforms of the mode distributions at different points along the waveguide

allow losses of the different modes in the system to be examined.

Waveguide bends are essential elements in IO, but are difficult to design for multi-mode waveguides due to differing levels of loss in each mode at the bend. This leads to a redistribution of energy in the waveguide after the bend and beating in the spatial intensity profile similar to that observed in the slab waveguides. This is a serious problem for multiplexing schemes such as spatial division multiplexing. Therefore advanced designs requiring grey-scale lithography have been proposed to maintain the intensity distribution on bends [152]. In this work, the issue was clearly demonstrated in intensity maps of the waveguide before and after the bend for a range of bending radii.

Finally, dielectric tapers were investigated as focusing elements. The fluorescence imaging allows the portion of light that is radiated into the surrounding medium to be measured and could theoretically be used to measure the light reflected in the waveguide core at the taper. As expected the sharper angle tapers radiate more light and at sharp angles to the direction of propagation. This method could be used to aid in design of focusing and mode converting tapers and help check for adiabatic tapering.

5 Microdisks as Planar Photonic Elements

As a result of their impressive light focusing characteristics, dielectric microdisks have been the subject of intensive study both computationally [157–159] and experimentally [29, 160, 161]. Generally, these studies use the microdisk as a stand-alone element and the illuminating beam is approximated as a plane wave. In this arrangement, microdisks have proven to be useful in many applications, such as nano-particle sensing, trapping/manipulation and more [26, 162–164]. In this chapter, the microdisk is studied as an integrated optical element; illumination of the microdisk from a waveguide with core material identical to the microdisk is examined. The illumination is split into two cases: a rectangular waveguide (its width similar to the diameter of the microdisk) and a slab waveguide (width $\gg$ diameter). The effect of varying the microdisk diameter, with respect to the waveguide is also discussed.

Beyond the microdisk, other dielectric structures for focusing light have been studied and are suitable for coupling light to a plasmonic element. One way of confining the field within a waveguide is by tapering the width of the waveguide. If the taper angle is small enough this method has negligible loss and can form focal spots smaller than a wavelength [165]. A reflective element which could be integrated has also demonstrated suitable focusing capabilities, with an NA of 0.45 [18]. Solid immersion lenses (SILs) have demonstrated deeply subwavelength focusing and have been investigated through simulation and experiment as planar integrated optical elements in the form of the PSIL and PSIM (planar solid immersion lens and mirror) which also produce focal spots a fraction of a wavelength [19, 20, 166]. These structures, along with other coupling elements, were covered in chapter 1. In spite of their suitable focusing capabilities, these elements are relatively large and it is the aim of this chapter to demonstrate a focusing element in the micrometre size regime—that is an element with both physical size and focal length of a few microns.

5.1 Theory

The general theory for light scattering by a microdisk has been covered in chapter 2.

5.1.1 Microdisk

A microdisk focusing element, as the name suggests, is a cylindrical structure which has a height small compared to its diameter which is typically a few microns. As a refractive element it gathers light similarly to a lens and its focusing capability depends on the incident wavelength, the diameter, the refractive index of the disk and the refractive index of the medium surrounding the disk. However, on this size scale the microdisk also causes non-negligible diffraction and gathers light from beyond its physical limits to a single focus. This combination of refraction and diffraction means that very high intensity (compared to background/incident intensity) focal spots can be produced. Whether the focus is within the disk or beyond depends mostly on the refractive index contrast, m, of the disk to the background medium ($m = {}^{n_{\text{disk}}}/_{n_{\text{background}}}$). A contrast of about 1.7 or higher is needed for the focus to form inside the disk. In this work two different regimes are studied—in the first the background medium is air, so $m = 2.05$ (the refractive index of the Si_3N_4 microdisk), and in the second the background medium is PVA, so $m = 1.4$. An example of the difference these parameters make is depicted in figure 5.1 in which the intensity of the total field (incident plus scattered) for different diameter cylinders is plotted. (The calculations are for infinitely tall cylinders and the methods for these calculations are described in chapter 2.)

The motivation to use a microdisk as a focusing/coupling element in planar waveguide structures came from previous work within the group which showed the remarkable performance of a microdisk [20]. The capabilities of the microdisk as a stand-alone lens have been well studied and it has been shown that suitably designed microdisks can form sub-wavelength focal spots, photonic nanojets and other phenomena. The basis for that work came from studies at the beginning of the last century concerned with light scattering by cylinders having diameters similar to the incident wavelength of light (most popularly from Mie whose name was given to this light scattering size regime). An analytical solution for the scattered field was found for the case of a plane wave incident on a cylinder and this is usually the starting point for quickly simulating different diameters and materials.

Figure 5.1 shows two different cylinder diameters—3 µm in (a) and (c) and 6 µm in (b) and (d)—with two different m—2.05 in (a) and (b) and 1.37 in (c) and (d). The effect of changing m is clear, (c) and (d) focus to a spot outside the disk, and in this geometry (infinitely tall cylinder, infinitely wide input beam) the larger diameters gather more light. The important characteristics of a focusing/coupling element are the full width at half maximum (FWHM) of the focal spot it produces (in transverse and longitudinal directions) and its light gathering efficiency (the ratio of the amount of light incident on the element to the amount of light contained within its focus). As a 2D case these simulations provided a rough approximation of what might be seen in experiment but 3D simulations were also performed and are discussed in the following section.

Generally, the width of the incident beam is much larger than the disk diameter and so it can be approximated as an infinitely wide plane wave. Under these illumination

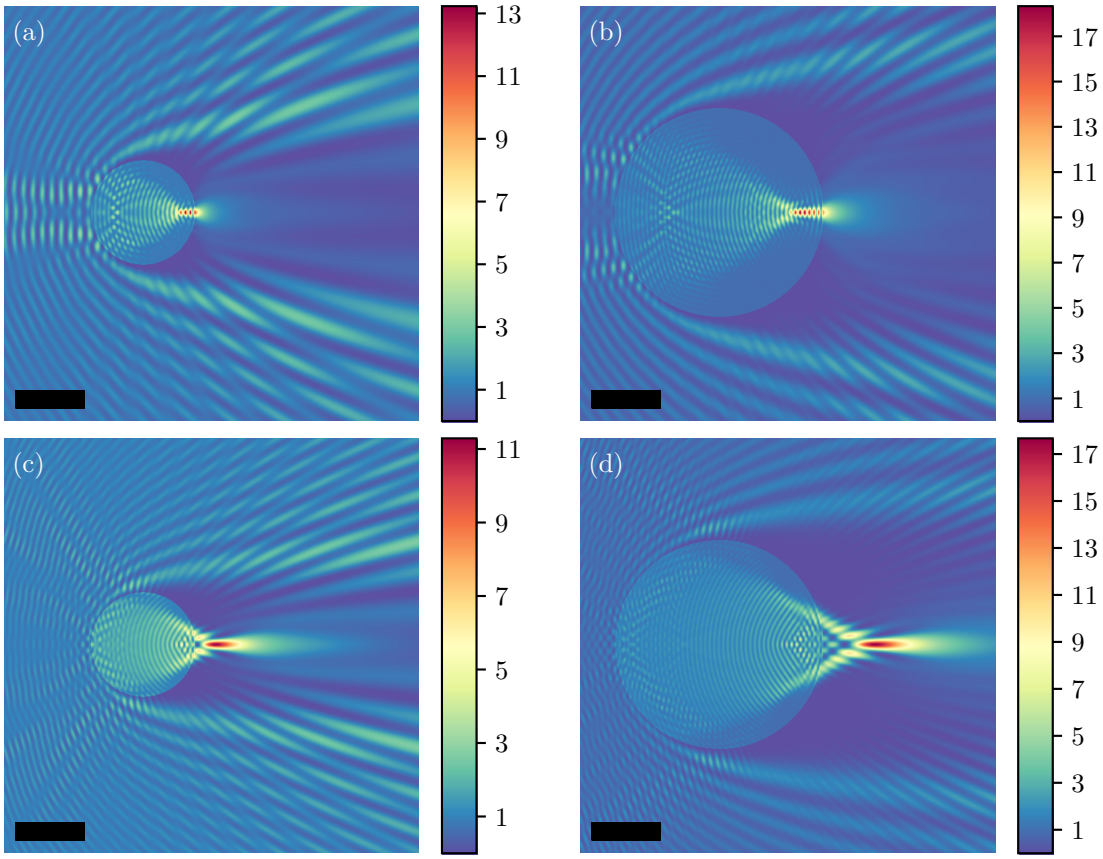

Figure 5.1 Total intensity resulting from a TM polarised plane wave (electric field along the cylinder axis) incident on cylinders of infinite height with refractive index 2.05. (a) Cylinder diameter is 3 µm and the surrounding medium has refractive index 1.00. (b) Diameter of 6 µm in same surounding medium. (c) and (d) show the same cylinders as (a) and (b), respectively, but in a surrounding medium of refractive index 1.5. Scale bar is 2 µm.

conditions the amount of light the disk can gather is proportional to its size and a larger disk will contain more optical power in its focus compared to a smaller disk. As an analogy to geometrical optics the numerical aperture of the focusing element increases with the diameter of the disk, so a tighter focus should also be formed. However, if the width of the incident beam is decreased to a few microns, it is not expected that increasing the diameter indefinitely would improve the focusing capabilities. This can be seen plainly when, for a large enough diameter, the disk will be effectively flat across the entire width of the beam. As such, there is expected to be an optimum ratio of width to disk diameter for a beam of finite width—one where the disk can gather a large proportion of the beam but is still curved enough to strongly refract the beam and form a sharp focus. To examine these regimes—infinite and finite beam width—in a planar photonics capacity two experiments were conducted. The first used light exiting a slab waveguide as the illumination for a set of microdisks of varying diameter while the second used a rectangular strip waveguide of fixed width (6 µm) to illuminate individual microdisks.

A drawing of the waveguides displaying the important parameters is shown in figure 5.2. The materials are the same as in previous chapters, however, the thickness of the Si_3N_4 core layer is 180 nm. At this thickness, the waveguide supports only the fundamental TE and TM modes. (The notation of TE and TM matches the notation for the illumination of the microdisk, i.e. a TE waveguide mode, with its electric field along the y axis illuminates the disk with its electric field transverse to the cylinder axis.) A 100 nm thick film of rhodamine B (RhB) doped poly-vinyl acetate (PVA) was coated over the structures for some experiments. The variable parameter of core width and disk diameter are also marked on the main image; the inset shows a slab waveguide with the difference to the main image being the very large core width.

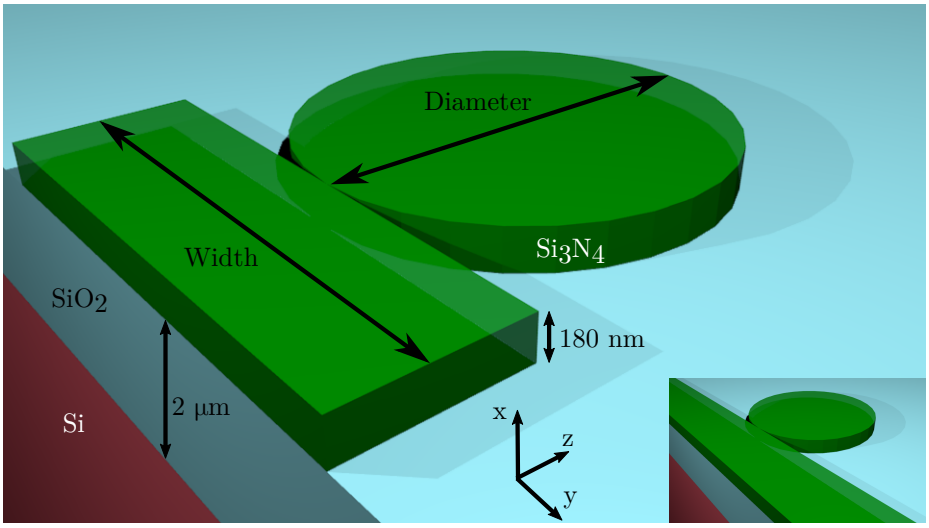

Figure 5.2 Schematic of the waveguide-disk combination used in the experiments in this chapter. (Some experiments include a layer of RhB doped PVA coated on top.) The inset shows the slab waveguide. The slab waveguide has a width of ~1 cm and the rectangular waveguides have a width of 6 µm.

5.1.2 3D simulations

With a simplified version of what to expect from the microdisks (from figure 5.1), the simulations were extended to full three dimensional numerical simulations. Finite difference time domain (FDTD) simulations were used to model how a disk of finite height affects a beam of light radiating from a waveguide. (The software used for these simulations was Lumerical's FDTD solutions.) Compared to the Mie scattering solutions shown earlier, the FDTD simulations provide control over the shape and width of the beam incident on the disk and account for divergence along the direction of the cylinder axis. A number of simulations for disks of varying diameter and waveguides of different width are shown in figure 5.3.

In the images in figure 5.3, the intensity of the electromagnetic field is mapped for structures similar to those shown in figure 5.2 with and without a PVA-RhB cladding.

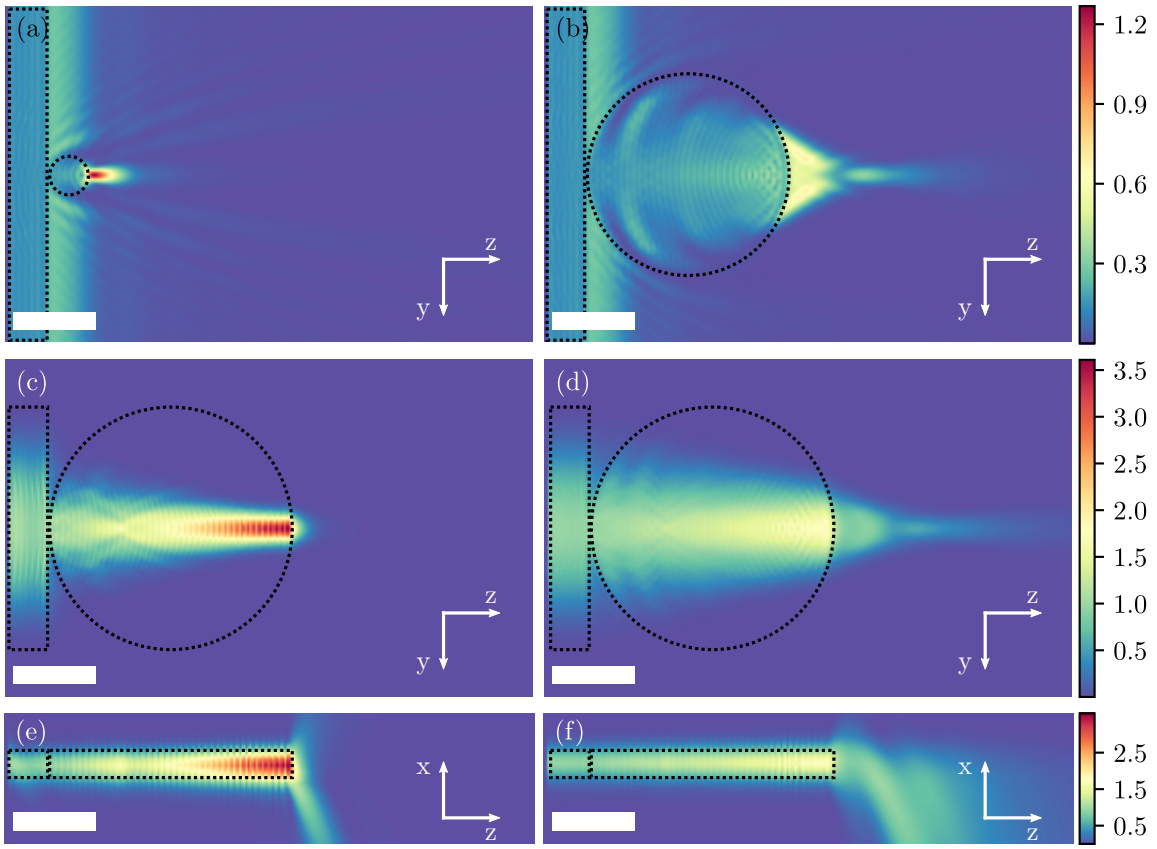

Figure 5.3 FDTD simulations of microdisks illuminated by waveguides. (a) and (b) A slab waveguide illuminating a 1 µm and a 5 µm diameter disk with PVA as the surrounding medium. (c) and (d) A 6 µm wide waveguide rectangular waveguide illuminating a disk of 6 µm diameter with air and PVA as the surrounding medium, respectively. (e) and (f) Cross sections through the centre of the disk for (c) and (d). Scale bar is 2 µm. The dashed lines signify the edges of the waveguide and the disk.

Each simulation is normalised such that the peak incident intensity in the core is 1. This normalisation makes it easier to compare the cases of different cladding material. The intensity maps in (a) and (b) are taken at constant height along the upper surface of the Si_3N_4 layer; this height was chosen as it should compare well with the power exciting fluorescence in the dye. For both (a) and (b) there is a layer of PVA cladding and the dashed circle signifies the edge of the microdisk. A slab waveguide mode is the input light source for the disks which have diameters of (a) 1 µm and (b) 5 µm. Comparing between the two simulations the 1 µm diameter disk produces the higher intensity focus, contrary to the 2D simulations shown earlier. (Reasons for this are given below.) Another important contrast between the images is the position of the focus relative to the disk. For the larger disk, the focus is ~2 µm beyond the disk while the smaller disk focuses light just beyond its surface. The separation of the focus from the disk and the information seen in the intensity maps (e) and (f) explain why the 3D simulations are inconsistent with the 2D ones.

The intensity maps in figure 5.3(c) and (d) show a 6 µm disk illuminated by a rectangular waveguide of the same width when the cladding is (c) air and (d) PVA. (These maps are taken through the centre of the Si_3N_4 layer.) The important aspect to note here is how the microdisk cladded by PVA gathers light from a wider area than the air clad disk. This is manifested as more of the disk being illuminated in (d) than in (c). The advantage of the air cladding is that the focus forms within the microdisk meaning it doesn't suffer from the divergence after the disk. For the PVA cladding the highest intensity is just inside the right hand edge disk even though the focus is formed outside. With intricate fabrication, an element combining the benefits of these geometries to improve on both could be made.

To see why the disk in (d) gathers more light than (c) and why the disk in (a) forms a higher intensity focus than (b) a different viewpoint is required. Figure 5.3(f) is a side on view of the same simulation showed in (d), cutting through the centre of the disk which is again outlined. (The horizontal to vertical scale is 1:4 to make the image distinguishable.) From this viewpoint it is clear that once light reaches the end of the disk it diverges quite quickly in the surrounding media. The divergence is what reduces the intensity of the focus (compared to 2D) since all of the light that was gathered has been spread out in this other dimension. As the focus for the 1 µm disk is so much nearer to the disk it suffers less from the divergence which is one reason for it having a higher intensity than the larger disk. Since the divergence only happens as the light beam enters the medium of lower refractive index it is presumed that placing a secondary element or target close to the surface of the disk would capture more of the light and increase the intensity of the larger disk's focus. It may also be possible to reshape the disk—to elongate it on one side such that it encompasses (or very nearly encompasses) the focus. Although this would alter some diffractive effects of the disk it might be more advantageous for reducing the loss to divergence.

The divergence of the beam after it exits the Si_3N_4 layer also affects the light gathering of the microdisk,and a comparison of what happens for a cladding of air and one of PVA is shown in figure 5.3(e) and (f), respectively. When the cladding is air, the beam splits upon exiting the Si_3N_4 with the majority of the power propagating into the higher index SiO_2 substrate. This rapid divergence is due to the width of the beam being smaller than the wavelength as it enters air (beam width ~220 nm $< \lambda/2$). The amount of power continuing directly forward after exiting the Si_3N_4 is very small meaning that a significant separation of waveguide and microdisk will have very weak coupling. When the film is added there is a marked difference in the power radiating from the waveguide end-face; the decay of intensity along the forward direction is much slower providing a better coupling at a given separation when compared to the air cladding. (Some light travelling upward—the positive x direction—is reflected at the PVA-air interface.) As is expected, the reflection at the waveguide end-face is weaker in the case of a PVA cladding because of the smaller refractive index contrast. These aspects make the PVA cladding a better option for coupling light from the waveguide to the microdisk (in terms of total power).

Returning briefly to the unexpected results in comparing (a) and (b) it is important to

state that larger disks have a greater average waveguide-disk separation than smaller disks. This results in larger disks being relatively less illuminated for the infinite beam width case and thus producing weaker focal spots.

Some of the focusing characteristics of the microdisks are listed in table 5.1. The reflected power (R) as a percentage of the incident power, the width of the focus and the peak intensity (I_{peak}) of the focus normalised to the incident intensity are given. (For rectangular waveguides, I_0 is the intensity in the centre of the core. For slab waveguides, R is unreliable as the incident power depends on the size of the simulation region chosen, however, it provides some comparison between different cylinders.) In table 5.1 it can be seen that the reflected power is lower when the PVA film is included. This is important for applications where the light source is butt coupled to the waveguide and light reflecting back into the source could cause damage. I_{peak} generally decreases with increasing diameter apart from the slab with air cladding case. The width of the focus increases with increasing diameter. It should be noted that although I_{peak} is low for the larger disks when PVA is used, there is higher intensity closer to the disk but the beam is considerably wider than at the focus.

Table 5.1 Simulated focal spot width, peak focal intensity and reflected power for disks of different diameter illuminated from a slab or rectangular waveguide (6 µm in width) cladded by air or a PVA film.

Waveguide	D_{disk} [µm]	FWHM [nm]		I_{peak} [I_0]		R [%P_0]	
		Air	PVA	Air	PVA	Air	PVA
Slab	1	222	240	4.008	2.515	6.34	1.37
	2	242	256	4.643	2.569	7.01	1.55
	3	296	298	4.683	2.525	5.91	1.68
	4	337	383	4.712	1.954	7.65	1.60
	5	388	335	5.207	1.138	5.58	1.47
	6	435	362	4.653	1.015	8.21	1.65
	7	468	381	5.199	0.759	5.34	1.94
Rectangular	1	222	243	4.251	2.457	7.43	2.37
	2	246	260	4.670	2.322	9.87	2.60
	3	306	318	4.569	2.093	5.79	2.98
	4	376	441	4.161	1.535	11.75	2.46
	5	443	414	4.390	0.686	4.75	1.57
	6	527	510	3.585	0.540	13.02	2.20
	7	586	677	3.810	0.430	4.09	3.12

5.2 Experiment

Set-up

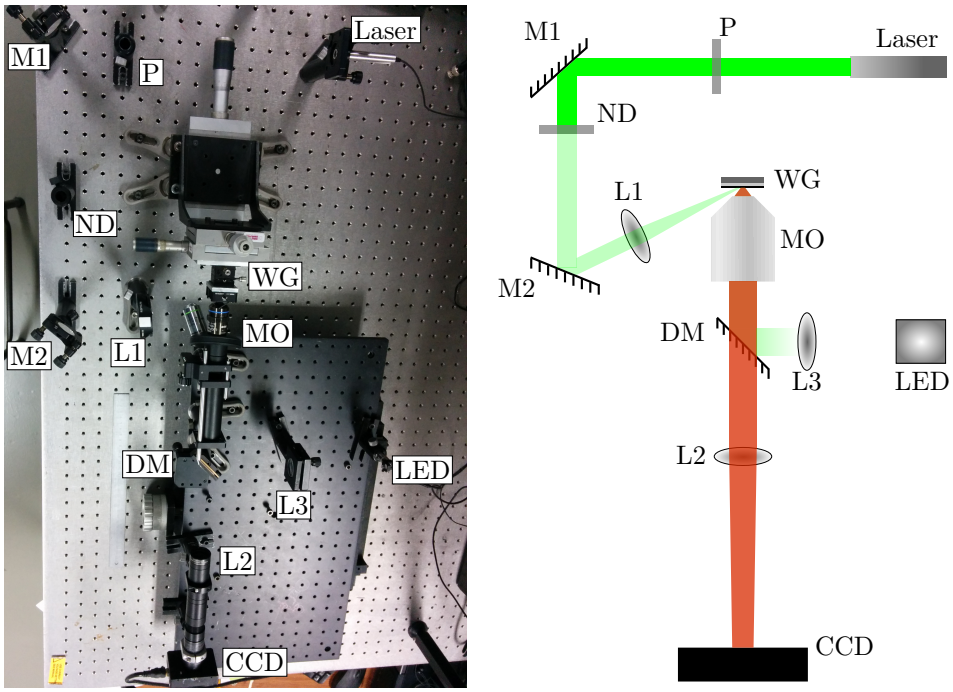

Figure 5.4 Experimental set-up for imaging light scattering and fluorescence of microdisks illuminated by waveguides. The green line shows the path of the laser through a polariser (P), neutral density filter (ND) and focused (L1) onto the waveguide (WG). The fluorescence, the red line, was collected by the microscope objective (MO) and imaged (L2) onto a CCD camera after any scattered laser light had been filtered out with a dichroic mirror (DM)—when imaging the scattered light, DM was removed. The LED and lens (L3) provided brightfield illumination of the sample.

The experimental set-up for the measurements covered in this chapter is the same as in figure 3.3 but is shown again in figure 5.4 as a reminder. For each measurement, the laser was coupled into the waveguide under TE or TM polarisation and the microdisk elements were illuminated by light radiating from the end-face. The scattering and fluorescence around the elements were then imaged onto the CCD camera to be analysed. For most of the images shown in this chapter, a microscope objective with a numerical aperture of 0.65 was used giving the set-up a theoretical resolution of ~530 nm for scattered light images (when the wavelength is that of the laser, 532 nm) and ~600 nm for fluorescence images (when the wavelengths are the RhB emission spectrum, ~580 nm). The fluorescence was imaged separately by the inclusion of the dichroic mirror which excludes green light (the laser) from reaching the camera.

Fabrication

All the structures presented in this chapter were fabricated using electron beam lithography (EBL), to define a mask, and inductively coupled plasma (ICP) etching. Although EBL is a time-consuming and not readily scalable process, this fabrication could be converted to ultra-violet lithography as the minimum feature size is >0.5 µm allowing for fast, large-scale production of these designs.

To make the etch mask for the sets of microdisks, a positive tone resist (Microchem Corp PMMA 950K A6) was spin coated onto the Si_3N_4 and left on a hotplate at 180 °C for three minutes and then the area around the would-be disks was exposed using an electron beam in a scanning electron microscope (SEM). The exposed area was removed by developing the sample in a solution of MIBK and IPA (concentrations 1:3, respectively) and the remaining PMMA formed a mask for etching. An ICP etch with Ar and CHF_3 was used to remove the exposed Si_3N_4, leaving behind a trench containing five microdisks of varying diameters. The trench itself is 90 µm x 40 µm, with the length of the trench beyond the disk found to be long enough that back reflections are not an issue. A number of these trenches were fabricated on a single chip and one of them is shown in figure 5.5. The diameters of the disks in each trench were designed to be 2 µm–6 µm in intervals of 1 µm but, as a result of fabrication variances (e.g. beam current, dose, alignment), there was some fluctuation in the size of the final structures. A spacing of 15 µm was left between each disk to avoid interference between adjacent ones. Post-fabrication, the diameters of the disks were measured and it was found that over the entire range of samples the fabricated diameter varied from the intended by ± 400 nm. To take account of this, disks' diameters are rounded to the nearest 0.5 µm when they're being compared. Images taken with an optical microscope and an AFM are shown in figure 5.5. The lighter colour corresponds to areas where the Si_3N_4 remains while in the darker areas it has been etched away.

The different micrographs shown in figure 5.5 give a representation of a typical fabricated sample. The optical image in (a) covers an entire array of microdisks which came out very close to the designed sizes (diameters ranging from 2 µm to 6 µm in steps of 1 µm). From this optical image the disks appear circular and uniform but they seem to overlap with the waveguide—there is no clear separation between the end of the waveguide and the edge of the disks. The resolution of this optical image, however, is around ~500 nm so it is not a definitive check and it was decided to examine the disks with a more precise measurement.

AFM was chosen as it can achieve finer resolution than the optical images. Two scans (along perpendicular directions) of a disk designed to have a 3 µm diameter are shown in figure 5.5 (b) and (c). (In both images the AFM tip is scanned along the x direction, as labelled.) Perpendicular scans were made to account for some virtual artefacts that appeared in the scans—such as the surfaces being curved transverse to the direction of scanning. From these images it can be seen that the surfaces are quite smooth while the sidewalls are somewhat rough; it is also clear that there is some distinction between the end of the waveguide and the beginning of the disk. To find quantitative values, line profiles

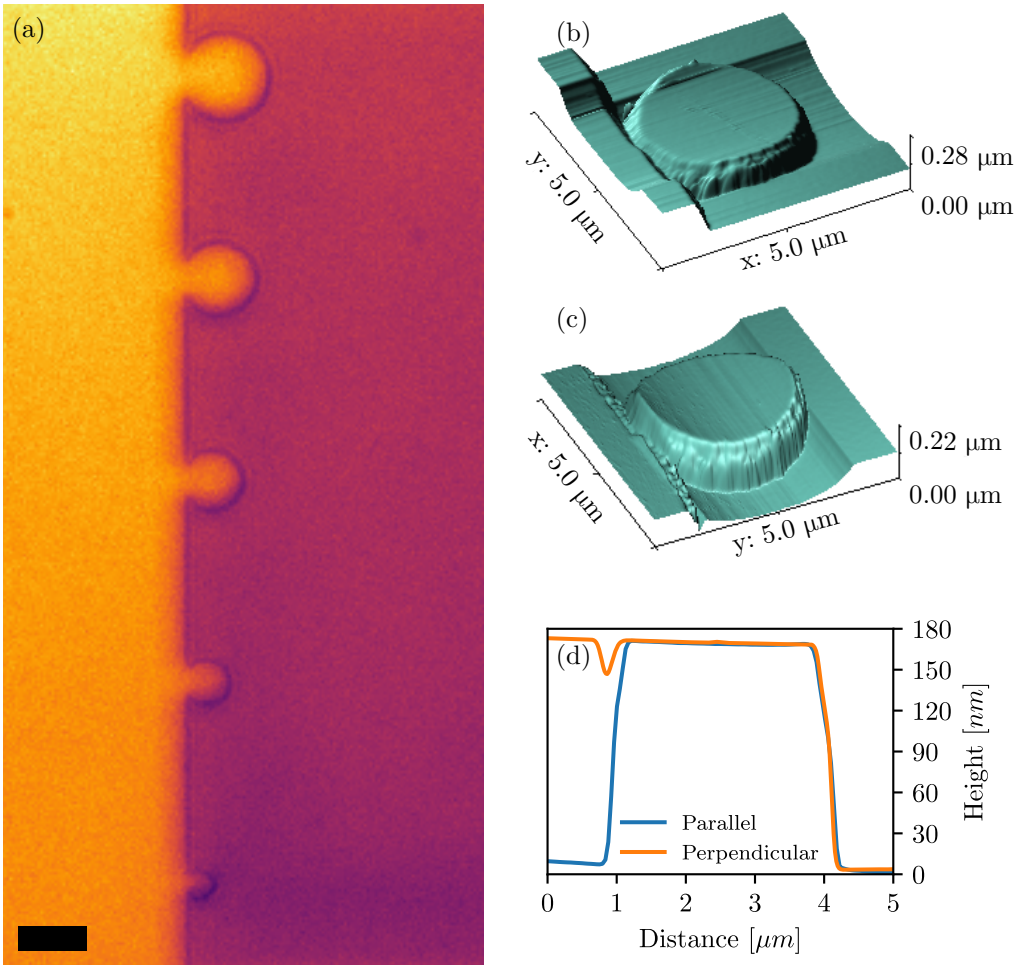

Figure 5.5 Microscope images of a sample of disks. (a) An optical micrograph of one set of disks (false coloured) ranging in diameter from 2–6 µm in 1 µm steps from the bottom to the top of the image. The scale bar is 5 µm. (b), (c) AFM measurements of a 3 µm disk scanned in perpendicular directions. (d) Graph of the AFM height taken through the centre of the disk from (b) and (c), perpendicular and parallel respectively.

were taken along the scan direction of these graphs.

In figure 5.5(d) the height of the AFM scan is plotted against the distance, x, running through the centre of the microdisk both "Perpendicular" (taken from (b)) and "Parallel" (taken from (c)) to the end-face of the waveguide. The diameters measured in either direction match well with each other and with the designed value. It can be seen (from the 'parallel' curve) that the sidewalls of the disk are not perfectly vertical so stating one diameter is not exact. The diameter at the top of the disk was measured as 2.78 µm while at the bottom it was 3.32 µm giving an average diameter of 3.05 µm (assuming linear sidewalls). The curve labelled 'perpendicular' shows that the disk and waveguide are connected although a notch ~30 nm in depth divides them. (This curve shows the smallest separation between disk and waveguide; a profile taken parallel to this one ~0.5 µm away, shows complete separation of the waveguide and disk.) Of course, some variation across samples is

expected but these measurements are intended to display typical values.

5.2.1 Illumination from slab waveguide

Light propagation in slab waveguides has already been covered in chapter 3 and here it is merely restated that a beam propagating along a slab is confined in one direction, allowed to diverge in another and propagates along the third. As seen earlier in figure 5.2 (inset) the beam was confined along the direction of the cylinder axis. As described in chapter 3, light was coupled into the waveguide by the end-fire method and a cylindrical lens was used to keep the beam width large and effectively a plane wave across the set of microdisks. Unlike chapter 3, the thickness of the waveguide core (180 nm) was sufficiently small to support only the fundamental TE and TM modes. This is an important restriction on the incident wave; if the input to the disk was multi-mode the resulting focal spot would be a linear combination of the focus for each of the separate modes and so wouldn't be as narrow or as well defined as in the case of only the fundamental mode being incident. Single mode propagation is generally desired for measurements of focusing elements and in certain planar photonic applications. The effective index of the TE mode was 1.84 (1.86 when using a PVA film) and that of the TM was 1.71 (1.77).

Scattering

The first measurements made on the microdisks were taken with no PVA cladding. In this configuration, only scattering images could be obtained. Images of the scattered light contain a great deal of information about the electric field [156], however, it is difficult to compare absolute intensities across different samples. Scattering relies on surface roughness or other discontinuities to divert light into the microscope collection so similar powers within the waveguide core do not always correspond to similar intensities in the image. In an effort to compare intensities, an appropriate method of normalising images is given. An example image of the scattering for TE polarisation is shown in figure 5.6(a) along with the intensity cross section for the 3 µm diameter disk (second from the bottom; the diameters of the disks increase ascendingly). Some statistics on the disks, averaged over the entire set of samples, are gathered and listed in table 5.2.

The image in figure 5.6(a) is a false colour representation of the scattered intensity caused by microdisks illuminated from a slab waveguide. The propagation direction is left-to-right and the broken, vertical 'streak' is light scattered by the end-face of the waveguide. For this sample, the disk with a diameter of 3 µm produced the highest intensity focal spot, however, judging by the variation of scattered intensity along the end of the waveguide it is assumed that the incident intensity was not constant across all the disks. While a wide input beam was used to try and provide constant power across all of the disks, any defects in or on the waveguide would cause the beam to diffract and result in an unknown profile to the intensity across the disks. To take account of this variation of incident power, the most reliable way to compare peak intensities for different disks was to normalise by the

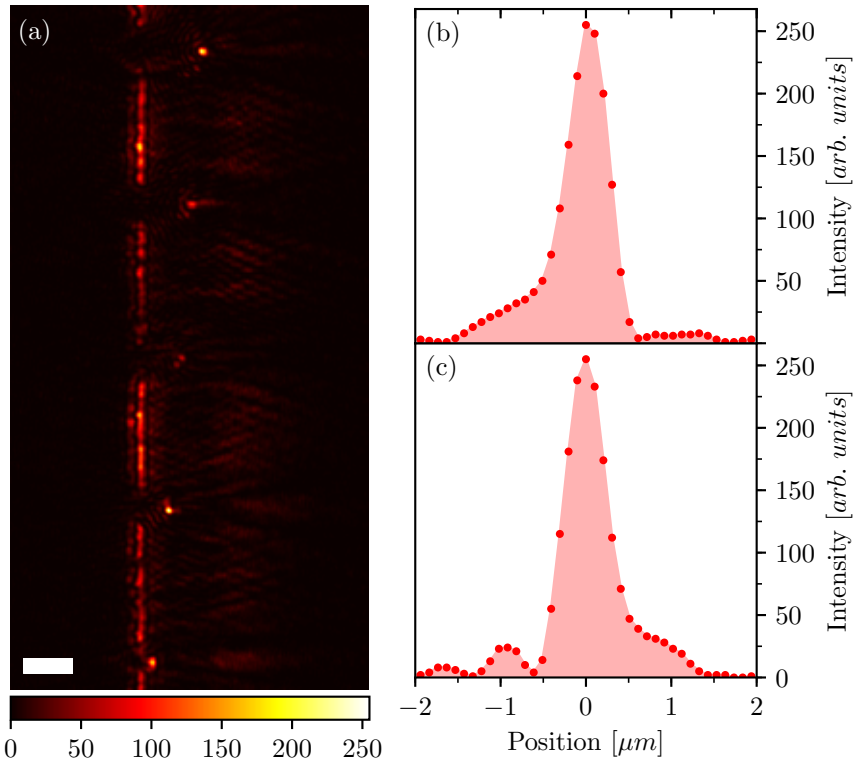

Figure 5.6 Light scattered by microdisks illuminated by a slab waveguide. (a) An intensity map displaying the scattered intensity for one array of disks; the scale bar is 5 µm. Cross sections of the intensity through the focus for the 3 µm diameter disk (second from bottom) are plotted in (b) and (c), across and along the direction of propagation, respectively.

scattering from the end-face close to the disk. The normalisation consisted of averaging the intensity over a distance of the radius of each disk either side of it. It is presumed that this end-face scattering was directly proportional to the power incident on the disk and so it is a suitable normalisation. (There is some dependence on the random surface roughness as well though it was assumed that over the number of samples this factor becomes insignificant.) This average was used as the incident power and divided into the focal intensity of the corresponding disk to give a 'light gathering efficiency' (see table 5.2). For the sample shown in figure 5.6, the 3 µm and 6 µm disk had similar gathering efficiencies while the 2 µm disk's was less than half theirs. From table 5.2, a general trend of the gathering efficiency increasing with diameter is seen. This behaviour is expected since a larger disk has a greater area over which it can gather light and was replicated in 3D simulations (see I_{peak} in table 5.1).

Having compared the gathering efficiencies of the microdisks, the focal spot sizes were considered. For a background of air, the focus is expected to form within the microdisk but close to the edge. (3D simulations showed that the focus formed ~200 nm before the edge of the disk.) The scattering from the disk edge gives a good indication of the focal spot and the FWHM of this scattering spot is used to compare the focusing of the disks. Cross

Table 5.2 Experimentally measured widths of the focal spots for microdisks illuminated by a slab waveguide mode. "Diff. lim'd"—diffraction limited.

Disk diameter [µm]	Mean FWHM (best) [µm]	Gathering efficiency (st. dev.) [a. u.]
2	0.65 (diff. lim'd)	3.27 (0.40)
3	0.61 (diff. lim'd)	5.97 (2.66)
4	0.62 (diff. lim'd)	4.97 (1.42)
5	0.68 (diff. lim'd)	6.88 (3.53)
6	0.67 (diff. lim'd)	10.00 (3.92)

sections of the scattered intensity taken through the centre of the focus of the 3 µm disk are plotted in figure 5.6(b) and (c). These plots demonstrate how tightly the microdisk can focus in the transverse (b) and longitudinal (c) directions and they verify (along with the images) that the focal intensity is much greater than any surrounding scattered intensity. From the curves, the FWHM is determined to be 570 nm and is believed to be diffraction limited by the imaging system. (The value of 530 nm stated earlier is a theoretical lower limit and it is expected that the real diffraction limit of the imaging set-up is greater than this.) Again, it was seen in simulations that this disk would focus below the diffraction limit of this imaging set-up (see FWHM in table 5.1). The transverse FWHMs of the other focal spots in this and the remaining samples were measured and are averaged in table 5.2 along with the minimum spot size. It was found that the disks regularly focused to/below the diffraction limit of the set-up.

A note on simulation-experiment comparison: light gathering efficiency increases with diameter as expected—even though larger disks are, on average, farther separated from the waveguide end-face than smaller disks, they have a greater area below a certain separation. This is what increases the light gathering efficiency. However, as larger disks collect over a smaller fraction, they collect over a smaller range of angles and therefore do not focus to spots as narrow as smaller disks. Since simulations produce focal spots below the diffraction limit of the set-up any variation cannot be verified but suggest that as a coupling element the diameter of the disk is important to create the spot power and size which would maximise coupling over the extent of the next element.

As covered earlier, changing the refractive index ratio of the microdisk to the surrounding medium changes where the focus forms. To investigate the case of the focus forming outside the disk, a layer of PVA-RhB was coated over the surface of the waveguide. This *superstrate* had a refractive index of ~1.5 giving a ratio of 1.37 which was enough to move the focus outside the disk. Doping the PVA with RhB produced a fuller image of the power distribution incident on the disks as well as making the focus visible—when it is moved outside the disk it has only air/PVA to scatter off.

Fluorescence

Using fluorophores to image the focusing caused by the microdisks provides different information to the images of the scattered light (as discussed in chapter 3). As well as moving the position of the focus, the superstrate also reduces the rapid divergence of the light radiated from the waveguide end-face which is seen in simulations, meaning that the disk can gather more light. The same sample of disks used in the previous section were studied with this fluorescent layer added and an example of each diameter is shown in figure 5.7.

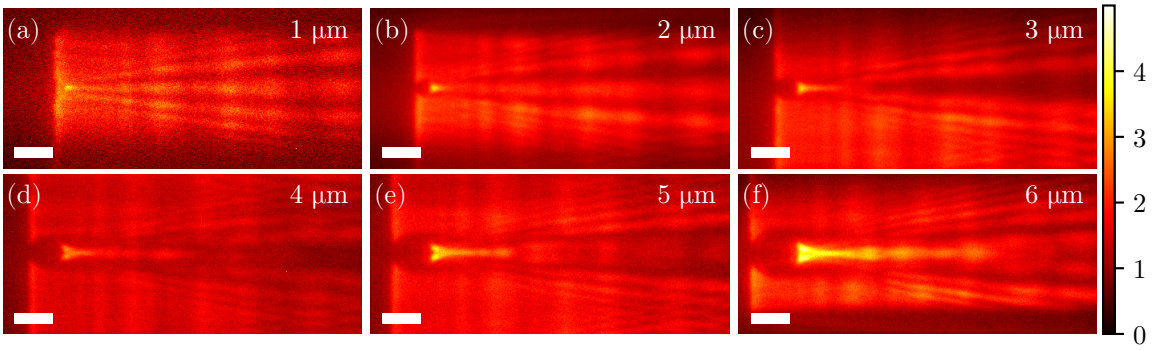

Figure 5.7 Light focusing by microdisks illuminated by a slab waveguide. Microdisks ranging from 1 µm to 6 µm in steps of 1 µm are shown in (a)–(f), respectively. Focusing, photonic jets and side lobes are visible for different diameters of disk. Scale bar is 5 µm.

The images in figure 5.7 are intensity maps showing, on a linear scale, the focusing of light radiated from a slab waveguide by microdisks of varying diameter. The diameter of the microdisks ranges from 1 µm (figure 5.7(a)) to 6 µm (5.7(f)) in steps of 1 µm. The flat, vertical line immediately before the disk marks the end-face of the waveguide. To display the images on a consistent scale, each one is normalised to the power incident on the disk. The incident power is deemed proportional to the fluorescence over an area of the waveguide before the disk. The value of average fluorescence for an area proportional to the disk diameter was set to one for each image. In theory, the field available to excite fluorescence could be related to the field in the core and an estimate of the incident to focal power could be made. (A similar method is used in chapter 3.)

A number of interesting optical effects can be seen in the images in figure 5.7. The first thing to note is the focus formed by each disk. As suggested by simulations, the smaller disks (figure 5.7(a) and (b)) produce higher intensity focal spots than the larger disks. For the larger disks, (d)–(f), it can be clearly seen that the focus is beyond the disk and that the beam exiting the disk is still quite wide. The simulations in section 5.1.2 show that once light exits the Si_3N_4 it diverges quite quickly (in the plane out of the page) meaning that some of the power is lost from the focus by having it so far beyond the end of the disk. Even with this divergence it can be seen that a region of (relatively) high intensity is maintained along the 'centre' long beyond the focus. This photonic jet is apparent, to varying degrees, for the different diameters. The intensity profile through the centre of the

disk along the direction of propagation is plotted in figure 5.8.

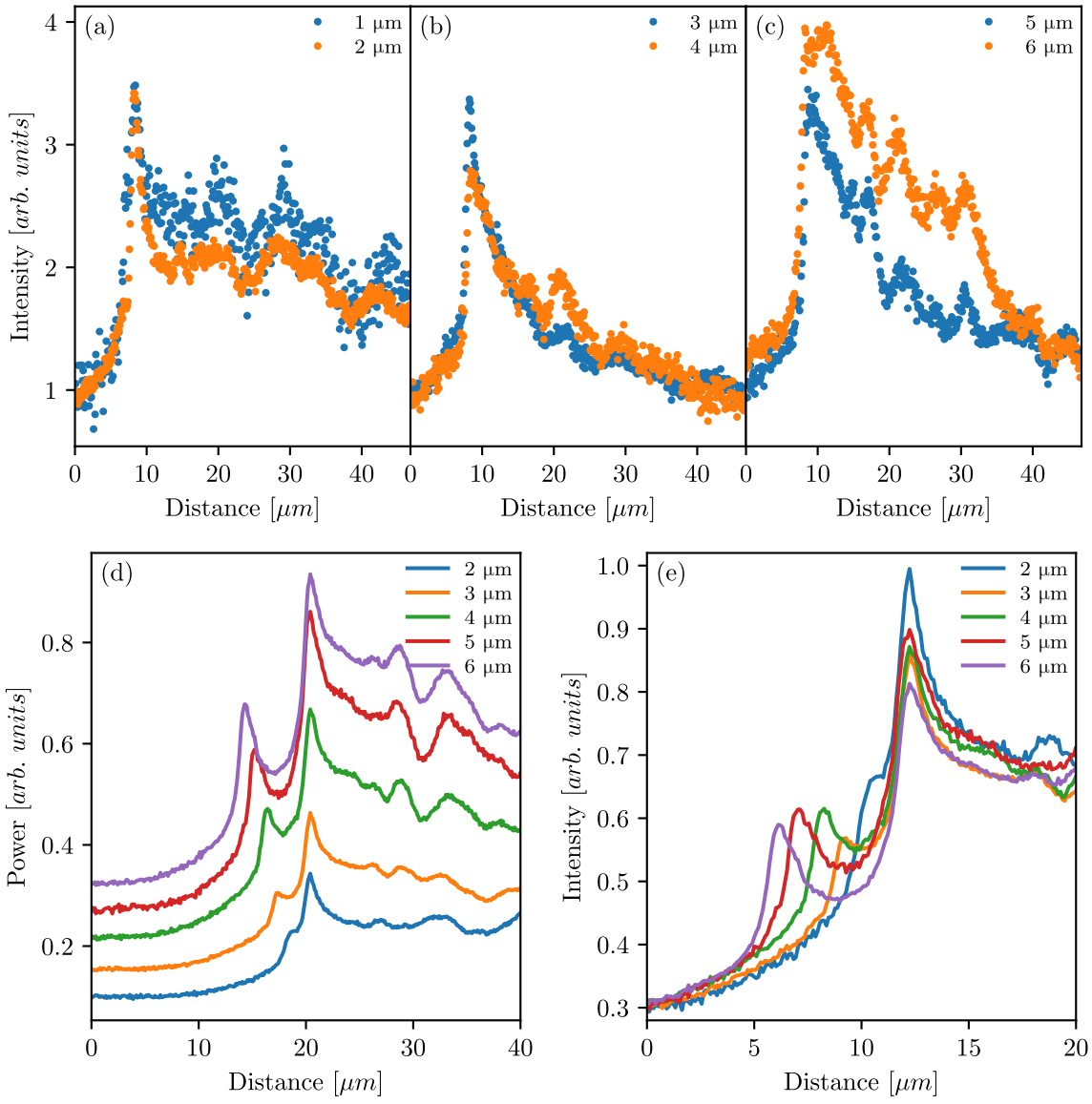

Figure 5.8 Cross sections of the intensity comparing the light gathering ability of the disks and the falloff beyond them. (a)–(c) Intensity through the centre of the disks shown in figure 5.7; disks with similar features have been grouped. (d) Power entering and gathered by disks of different diameters averaged over samples. (e) Intensity for same.

From the images in figure 5.7, there appear to be distinct cases for the intensity beyond the disk and these cases have been separated into three pairs of curves plotted in the graphs in figure 5.8. Figure 5.8(a) plots the 1 µm and 2 µm diameter disks, both following a similar trend—the intensity decreases quickly after the focus but then levels off at over half the peak intensity and diminishes very slowly over tens of microns. The 3 µm and 4 µm diameter disks, plotted in (b), produce slightly different effects—the intensity initially decreases more slowly but continues to falloff at this rate and eventually falls below the intensity of the

smaller disks. The largest disks, plotted in (c), appear to have two 'stages' separated by a sudden drop in intensity. The decay rate in the initial stage is slower than for the smaller disks but the sudden drop brings the intensity to a level to the 3 µm and 4 µm disks. The divergence angle of the central beam of the 1 µm disk is 6.3°. 2D simulations were performed and replicated/verified these characteristics. (3D simulations over such a large region used prohibitive amounts of computing power.) The plots (d) and (e) compare the light gathering efficiency for the different disks. The data for these was attained by taking cross sections similar to those in (a)–(c) but along each row over the entire diameter of the disk. Averaging these cross sections for each disk and normalising such that the *input* to each disk was equal it can be seen how efficiently the different disks gather the light incident on them (plotted in (e)). To produce a plot for total light gathering, the normalised curves are multiplied by the diameter of the disk (plotted in (d)). From (d) it is apparent that increasing the diameter of the disk increases the amount of light that is collected (the height of the peaks increases); this, of course, is expected since the larger disks have more light incident on them (this can be seen in the graph as the *Power* at $Distance = 0$ increases with disk diameter). The first peak/kink in the curves marks the end of the waveguide. Although the curves show that the incident power increases with disk diameter if a constant input beam width was chosen the incident power would be constant over disk diameters and the power beyond the first kink would remain the same for each of the curves. This would show the largest disk to be an improvement on the others and the idea is studied explicitly in the section below. A comparison with the increase in fluorescence produced by removing the microdisk and simply terminating the waveguide with a flat edge is not shown although it was seen when taking similar intensity profiles through a flat edge that there was an increase of $\sim 2.8 \pm 0.2$ from *input* to peak. From the curves in figure 5.7(e) it can be seen that there is about the same increase as the flat edge suggesting that a large amount of the light has been gathered and also (since there has been some focusing) that the intensity at the edge of the disk should be greater than that at a flat edge. This may be seen in the images in figure 5.7. Also from (e) it is clear that the smallest disk gathers light most efficiently while the largest is the least efficient. This has been explained earlier as the larger disk having a greater average separation from the waveguide and so it is only able to gather a smaller fraction of the light incident on it. This suggests that above a certain diameter there is no benefit to having a microdisk and that optimisation of disk diameter would need to be done for different input wavelengths.

These different cases could find use in varying planar photonics applications aside from light focusing elements. The low divergence, central beams in figure 5.7(a) and (b) appear ideal for coupling between structures as the slowly changing beam width means that separation would not be severely strict. The intensity in (c) is along the lines of a beam splitter with two symmetric output 'arms' for symmetric input. The depth of focus in (f) (corresponding to the plateau in intensity clear in figure 5.8(c)) is also a desirable aspect of a focusing element as it provides some margin for error in fabrication or alignment of

different structures.

5.2.2 Illumination from rectangular waveguide

Illumination from a rectangular waveguide is expected to be a more common integrated optical scenario as rectangular waveguides are more frequently used than slab waveguides. In this arrangement, the ratio of the disk's diameter to the waveguide's width is important. As the waveguide's width defines the beam width illuminating the disk, there is a finite amount of light that a disk can collect and in contrast to the previous section, the light gathering efficiency is related to the total power in the waveguide and not just the power directly incident on the disk. As in the previous section, it was necessary to have a reliable method for normalising different disks.

Structures

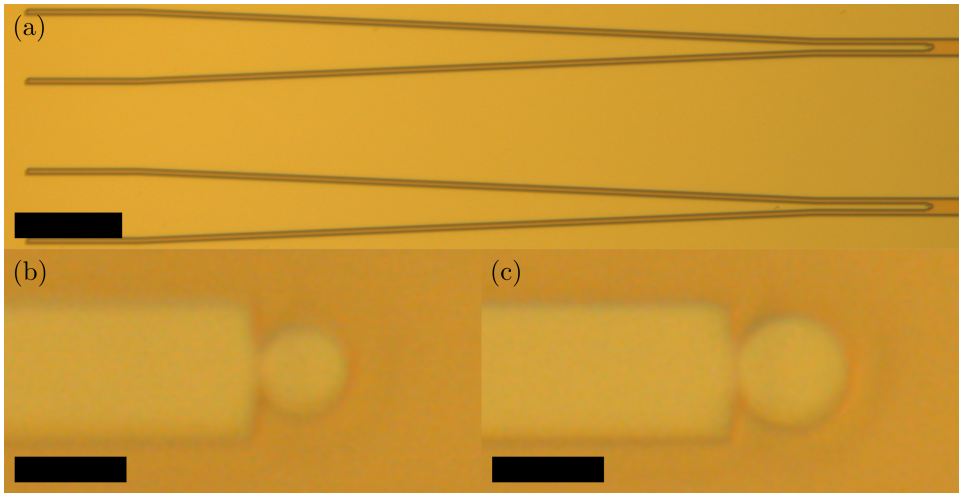

Figure 5.9 Optical microscope images of structures for illuminating a microdisk with a rectangular strip waveguide. (a) Full-view of structures showing the initial, tapered and final waveguide regions (scale bar is 100 µm). (b), (c) Magnified views of waveguide end and disk of 3 µm, 5 µm (scale bar is 5 µm).

In this experiment, rectangular waveguides of constant width were used to illuminate microdisks of varying diameter. The width of each waveguide was 6 µm and the diameter of the disks varied from 2–7 µm. For this experiment it was important that only a single mode was propagating in the waveguide and incident on the disk. To achieve single mode propagation, the structures shown in figure 5.9 were fabricated. These waveguides are initially 60 µm wide and the gradually taper (over ~700 µm) to the 6 µm final width and the disk. The complete structure can be seen in figure 5.9(a) where the darker regions mark the edge of the waveguide where the Si_3N_4 has been etched away. The images in (b) and (c) show the end of two waveguides with disks of diameter 3 µm and 5 µm, respectively. AFM

measurements, similar to those described in section 5.2, were made to check the diameter of the disk and the separation from the waveguide, with similar results found.

The slow tapering of the waveguides shown in figure 5.9 was used to convert the initial coupled mode to a narrower waveguide without exciting higher order modes. The fundamental mode of the final waveguide has an intensity profile similar to a Gaussian centred on the disk and FWHM about half the width of the waveguide (i.e. ~3 µm). (An idea of the profile can be seen in the simulations in figure 5.3(e) and (f).) This profile contrasts with those from the previous section as there is less light available away from the centre of the disk.

Measurements

The experimental method and set-up for the measurements in this section were similar to those described in the previous one. Light was end-fire coupled into a slab waveguide using a spherical lens and this mode propagated into the 60 µm wide rectangular waveguide shown in figure 5.9. The lens was chosen such that the beam width was narrower than 60 µm at the beginning of the rectangular waveguide and scattering images of the slab-to-rectangular interface suggest this was achieved. (Because there was negligible scattering from the sidewalls.) It was then assumed that this mode was converted to the fundamental mode of the 6 µm wide waveguide. The light scattered by the microdisks was imaged to extract focal spot sizes and light gathering efficiencies. Some of these images are displayed in figure 5.10.

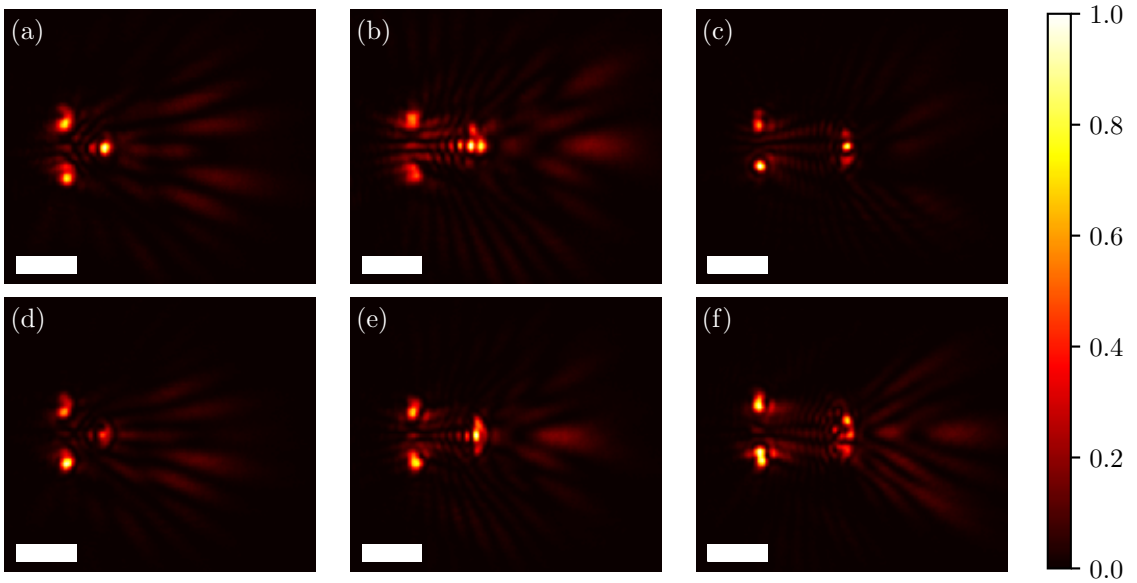

Figure 5.10 Light scattering images of microdisks illuminated by rectangular strip waveguides. (a)–(c) Intensity maps for TE polarised input and disk diameters 3 µm, 5 µm and 7 µm, respectively. (d)–(f) show the same for TM polarisation. Scale bar is 5 µm

The intensity maps in figure 5.10 show the light scattered by disks of different diameter

for different input polarisations. (Each image has been normalised to its own highest value so that more information is visible). The images in (a)–(c) used TE polarised input for disks of 3 µm, 5 µm and 7 µm, respectively; those in (d)–(f) show the same disks but with TM polarised input. Although comparing intensities across different images requires suitable normalisation, certain information can be extracted from the images as they are shown—such as the focal spot size. The FWHM of the spots were consistently larger than predicted by simulations; the narrowest focus was formed by a 3 µm disk and was ~700 nm. Typically, the FWHM of the focal spots was ~800 nm ± 50 nm for each diameter. This is believed to be due to higher order modes propagating in the waveguide and work is ongoing to get fundamental mode illumination of the disk.

To attempt to compare focus intensities across these images, the scattering from the sidewalls is used to normalise them. The sidewall roughness from waveguide to waveguide is consistent and so the scattering from waveguide to waveguide should be proportional to the power propagating along it. Due to the disparity of the EM field at the waveguide walls between TE and TM modes, this normalisation is not used to compare the different polarisation cases. Early work shows that the smallest disk collects more light, however, the scattered intensity at the sidewalls was very low in these images and similar to spot size measurements further work needs to be done before reliable results are realised.

5.3 Conclusions

Light focusing by dielectric microdisks illuminated by the light radiating from the end-face of a waveguide was studied through simulation and experiment. Two different regimes were investigated: in the first, the material surrounding the disk was air and light incident on the disk was brought to a focus within it; in the second, the material outside the disk was PVA ($n_{PVA} \sim 1.5$) and the focus formed outside it. The waveguides used with the disks varied between a slab—where the incident beam is much wider than the disk—and a rectangular strip—incident beam width similar to disk diameter. The disk had the same height and was made of the same material as the core of the waveguide.

Analytical calculations were used as preliminary simulations but were found to overlook important factors. 3D FDTD simulations were used to model the focusing elements more precisely. In the 3D simulations it could be seen that light radiated from the waveguide diverges quickly, especially when the background material was air; this divergence is a result of the thickness of the core layer being much smaller the wavelength. This divergence affected the light gathering efficiency of the disks in both regimes and when the focus was formed outside the disk, it reduced the peak intensity of the focus. For disk diameters in the range 2–7 µm illuminated from a slab waveguide, simulations showed that a 1 µm diameter disk produced the tightest focus and a 5 µm produced the maximum intesity when the cladding material was air (1 µm and 2 µm, respectively, when a 100 nm PVA film was the cladding). For the same range of disks illuminated from a rectangular waveguide, a 1 µm

disk produced the tightest focus and 2 µm produced the maximum intesity in air (1 µm for both with PVA). Focal widths $< {}^{\lambda_0}/_2$ with peak intensities $> 4\times$ the incident intensity were produced in simulations.

In experiment, the imaging set-up limited measurement of the focal spot widths, however, the focusing effect was clearly demonstrated. Scattered light images showed the focusing for a background material of air and with a slab, the average FWHM of the focal spots was ~640 nm for each diameter of disk (in the best case, each disk focused below the diffraction limit of the set-up); in this configuration, the light gathering efficiency of the disks was found to increase with diameter. When PVA was the background material, the gathered power was found to increase with diameter, however the gathering efficiency was shown to decrease as the disk diameter increased. This regime also showed narrow, slow diverging focuses (known as *photonic jets*) forming outside the disk.

For the case of illumination from a rectangular waveguide, only preliminary measurements of the scattered light were made. The images show that focusing was achieved, however, from the intensity distributions it is likely that multiple modes were propagating rather than just the fundamental mode. Further work in this configuration would need single mode propagation for the microdisks to focus to minimum spot sizes.

Ultimately, the microdisks studied in this chapter might find use in coupling light between different elements in photonic integrated circuits or as an on-chip planar lens for sub-wavelength focusing. Dielectric elements have been suggested for coupling to plasmonic focusing elements in heat assisted magnetic recording systems. In this configuration, photonic jets could be used for on-chip sensing applications—there is large backscattering when a particle passes through the photonic jet—as well as for optical data storage [163, 167, 168].

6 Fresnel Zone Plates

In the previous chapter, a focusing element illuminated by the light radiating from the end-face of a waveguide was studied. It was found that the rapid divergence of light between the waveguide and the element reduced the gathering efficiency of the element. To overcome this drawback, a focusing element which is contained within the waveguide core was designed and measured and is presented in this chapter. The element consists of a number of holes milled or etched into the waveguide core which scatter the propagating waveguide mode. By deliberately positioning the holes, their scattered fields constructively interfere to form a high intensity focus. The elements were designed to focus the incident waveguide mode to a point on or near the end-face of the waveguide to make it accessible to other components. The design, simulation and measurement of these focusing elements, referred to here as a Fresnel zone plate, is discussed in this chapter.

6.1 Background

Traditionally, free space focusing optics could neglect diffractive effects because the size of the elements is so much larger than the wavelength of light. Recently, however, the topic of diffractive optics has seen a surge of interest and diffractive focusing has been well studied both theoretically and experimentally on these size scales [169, 170]. Diffractive focusing elements often find use in specialised cases such as for focusing x-rays because most materials are opaque to radiation at those frequencies and refractive index values are close to 1 [171]. On scales comparable with the wavelength, refractive effects are less dominant and diffraction of an incident light beam can be used to form a focus. With the increase in computing power now available, micron scale elements can be designed through numerical optimisation methods, e.g. a scattering based lens in a silicon waveguide at a wavelength of 1550 nm has recently been demonstrated [172]. Similar photonic crystal lenses which introduce large arrays of holes (typically 100–200 nm) into the waveguide core and Fresnel lenses and overlaid Fresnel lenses, where a Fresnel lens is lithographically defined on top of the waveguide core thus altering the effective index in the core to cause focusing, have

been investigated as planar photonic focusing elements [173–179]. (In the case of these Fresnel lenses, each of the individual structures making up the lens are ~10 µm in size.) An example of a diffractive focusing element is the Fresnel zone plate which, along with the Rayleigh-Wood zone plate, was the inspiration for the structure presented in this chapter.

A Fresnel zone plate (FZP) is a focusing element which works by diffracting an incident beam of light to cause constructive interference at a specified location. A basic FZP is designed as a sheet consisting of concentric transparent and opaque rings (see figure 6.1). The sheet is transparent at the centre and the opaque rings have inner and outer diameters such that they block any light which, at the focus, would be out-of-phase with light travelling through the centre. This means that all the light arriving at the focus is in-phase and constructively interferes. One drawback of this design is that simply blocking light with opaque material reduces the collection efficiency. Alterations can be made to improve the efficiency: in the case of the Rayleigh-Wood zone plate, the opaque regions are replaced with a material which adjusts the optical path length such that light from these regions will be in-phase with light travelling from the transparent regions. The focusing element studied in this chapter was originally designed on a similar principle. Cylindrical holes were made in the core of a waveguide to block parts of the propagating mode; the positions and diameters of the holes were defined by same the design as a FZP. Ultimately for the structures presented in this chapter, the design was based on how the individual holes scatter light—the design process is explained in a later section—but the focusing elements are still referred to as FZPs.

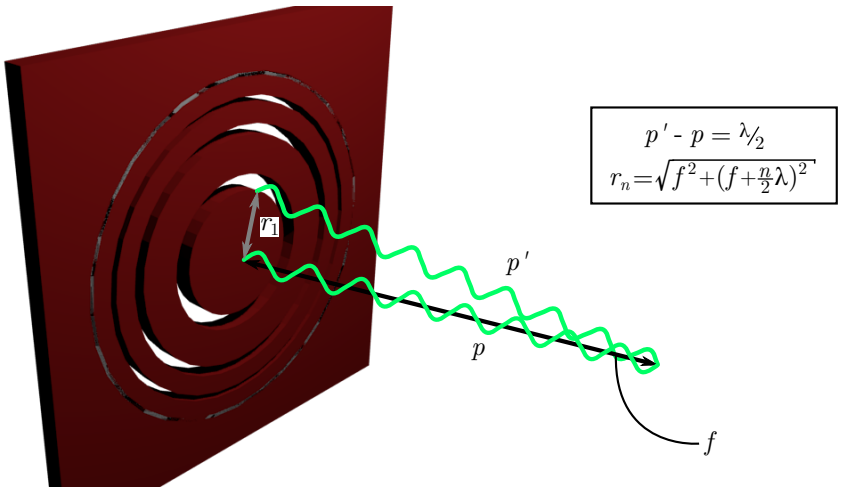

Figure 6.1 Fresnel zone plate consisting of transparent rings in a sheet of opaque material. The distance from the centre to the outer edge of the n^{th} ring (r_n) depends on the desired focal length f and the wavelength λ.

The focusing elements are made up of sub-micron cylindrical holes and have focal lengths of several microns. As discussed in previous chapters, on this size scale the approximations of geometrical optics or dipole scattering cannot be used and Maxwell's equations have to be explicitly solved (see chapter 2). As with the microdisk, the starting point for designing a

suitable FZP was the plane wave scattering solutions for the Mie regime. Although the codes are for a single, infinitely tall scatterer they provide a useful, quickly solved base for more precise simulations later. Over the following sections the methods for designing, fabricating and measuring the FZPs as an integrated optics structure are discussed. Similar to the later measurements of the microdisks, a RhB doped PVA cladding was spin-coated on the Si_3N_4 layer to aid imaging. Using a cladding of PVA provides some control over the refractive index contrast which is an important parameter for scattering (as explained in chapter 2). By changing the thickness of the cladding, the effective index of the waveguide mode would change thereby changing the refractive index contrast of the hole to the background.

6.2 Design and Simulation

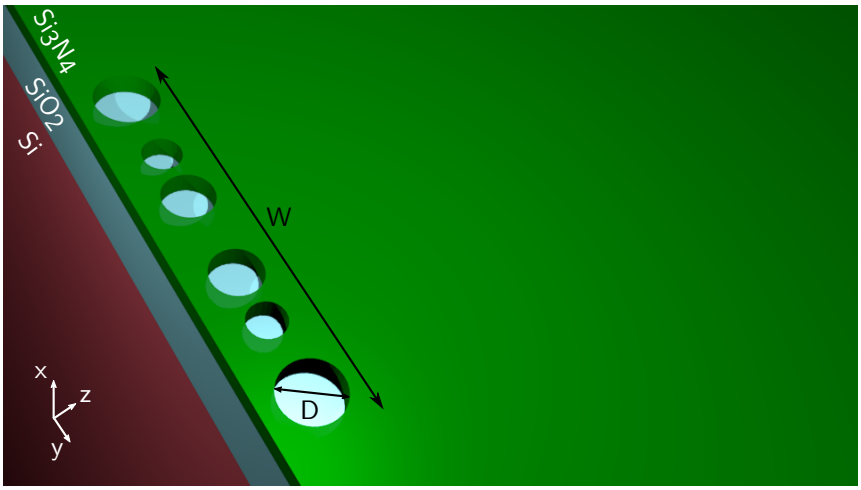

Figure 6.2 Schematic of focusing/coupling element. An example of how holes of varying diameter (D) in the waveguide core can be arranged in a certain width (W) to make a light focusing element. (As in other chapters, light travels along the z direction.)

The material geometry (shown in figure 6.2) for these experiments was the same as in the previous chapter—a 180 nm thick Si_3N_4 layer on 2 µm SiO_2 on a Si base wafer. (The wavelength of light used in experiment was 532 nm.) Holes in the Si_3N_4 core layer were made by milling or etching (described later). For imaging, a dye doped PVA layer (not shown) was spin coated on the Si_3N_4. The widths of the elements were typically 6–10 µm and the diameters of the holes were between 300 nm and 900 nm. For the geometry shown in figure 6.2 the waveguide mode propagates along the z direction. The method used to decide the size and position of the holes is explained below.

6.2.1 Individual inclusions

The theory relating to light scattering by an infinite cylinder was covered in chapter 2; here, it is shown how the scattered field (and as a consequence the total field) varies with the size

of the cylinder. For the work in this chapter, the cylinder has a lower refractive index than the background medium in which it is contained. The focusing element consists of an array of cylinders and to design an efficient element, it is important to know the light scattering of these substructures. The amplitude and the phase of the scattered electric field for three cylinders with different diameters are plotted in figure 6.3.

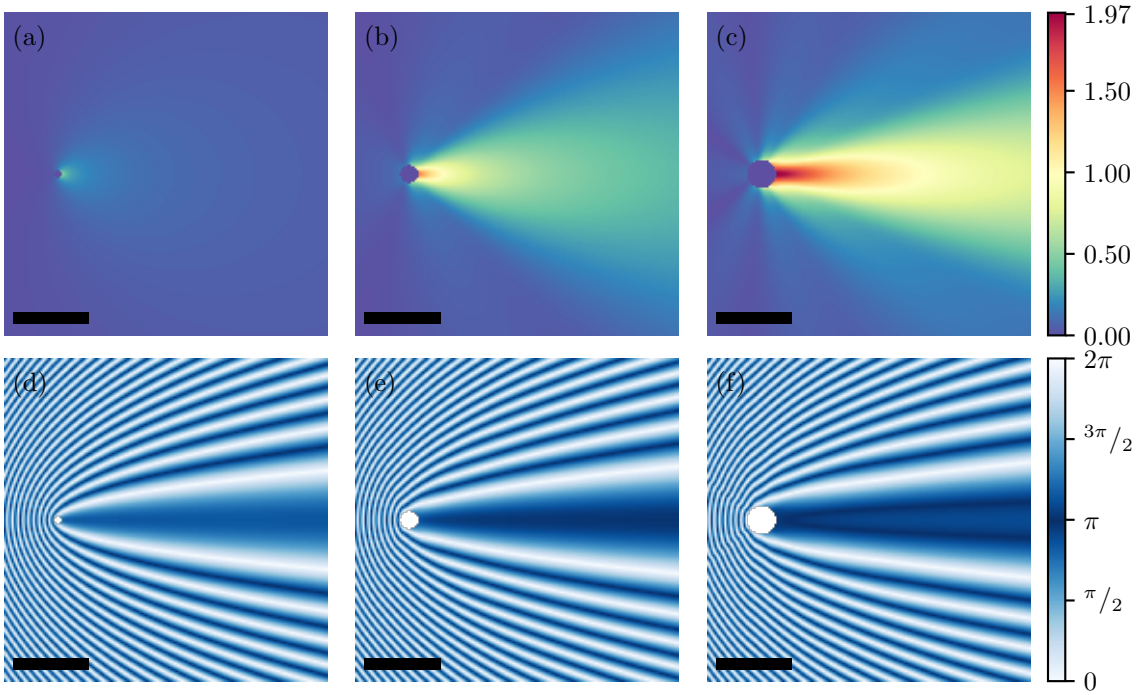

Figure 6.3 Light scattering by infinite cylinders of varying diameter. The background medium has refractive index 1.77 (the effective index of the TM mode) and the cylinder has an index of 1.5. (a) The amplitude of the scattered electric field when a plane wave is incident from the left on a 200 nm diameter cylinder; (d) the phase difference of the scattered and incident electric fields for the same cylinder. (b), (e) and (c), (f) show the same for cylinders of 500 nm and 800 nm, respectively. The scale bar is 2 µm.

The images in figure 6.3(a)–(c) are plots of the theoretically calculated amplitude of the scattered electric field for cylinders of diameter 200 nm, 500 nm and 800 nm for TM polarised input. The data are plotted on the same amplitude scale for ease of comparison across the diameters and are normalised such that the incident intensity is 1. The background medium has the refractive index of the fundamental TM mode (TE calculations aren't shown here) of the waveguide described above and the cylinder was given the refractive index of PVA (1.5) under the assumption that the PVA coating would seep into the holes. (Calculations were also performed for an air cylinder in case the PVA simply coated over the top of the hole; to avoid repetition the calculations are not shown here.) As might be expected, the largest cylinder has the strongest scattered field and it is evident that these cylinders scatter light mostly in the forward direction with only a small fraction of the incident light reflected back. The angular spread of the forward scattering is also important as, for an

effective focusing element, light should be gathered over the full extent of the incident beam (expected to be ~5–10 µm). To do this, the width of the focusing element matches the width of the beam and holes placed on the outer edges of the element then need to scatter light at higher angles than those placed near the centre. It can be seen that the 800 nm diameter (in figure 6.3(c)) produces a number of scattering lobes of moderate intensity and the 500 nm diameter in (b) produces some low intensity lobes at very high angles (at almost right angles to the incident beam) which would be utilised. For the 200 nm diameter cylinder (a) the scattering is weak and almost constant for forward angles below 60° where it begins to drop off quickly. As might be expected, the scattering is symmetric about the horizontal axis. This suggests that half the light incident on the cylinder is lost to the undesired side (i.e. away from the would-be focus) while even on the desired side power is lost to other diffraction orders. Although these images show where the scattered field is strong, it is also important to know how the scattered field interferes with the incident field.

The plots in figure 6.3(d)–(f) map the phase difference of the scattered and incident electric fields when a plane wave is incident (travelling from left to right) on cylinders of diameters 200 nm, 500 nm and 800 nm, respectively. The plots show the phase difference (modulo 2π) between the scattered field and the incident field—a difference of 0 or 2π produces constructive interference and a difference of π causes destructive interference. (The symmetry of the colourmap does not intend to suggest that a phase difference of $^{\pi}/_{2}$ is the same as a difference of $^{3\pi}/_{2}$ but only that these phase differences would cause the same reduction of intensity of the interfering fields.) The plots are used to find the lateral positions where the scattered field is in-phase with the incident field a chosen distance (i.e. the focal length) after the cylinder. In these calculations, the incident field is the same regardless of the diameter of cylinder. This means that when the scattered field is in-phase with the incident field in its own plot, it is in-phase with the incident field in another plot and the phase can be compared cylinder-to-cylinder. The first contrast to notice is in the forward scattering where the larger diameters are more out of phase with the incident field at low angles compared to the smallest diameter. There is also a slight change in the position of the diffraction orders for the different diameters (this is clearer to see in the intensity profile plotted in figure 6.4(b)). As a result, the positions of constructive and destructive interference of the scattered field with the incident field are different for each cylinder. Combining the scattered field amplitudes with these phase maps the arrangement of the cylinders to scatter light to the focus was determined; this becomes clearer in figures containing the total intensity in the following section.

6.2.2 Designing focusing element

When designing the focusing element the first parameter that was set was the focal length. An example element, with the focal length chosen to be 5 µm, is described here. Two element widths—this is the distance separating the outer edges of the outermost cylinders (see figure 6.2)—were set before design as well, 6 µm and 10 µm. To design a lens, the starting point

was to calculate the total intensity (combined incident and scattered fields, see chapter 2) for a range of diameters 100 nm–1 µm. The lower limit was set as a reliable fabrication constraint and the upper limit was chosen to reduce the overall size of the element.

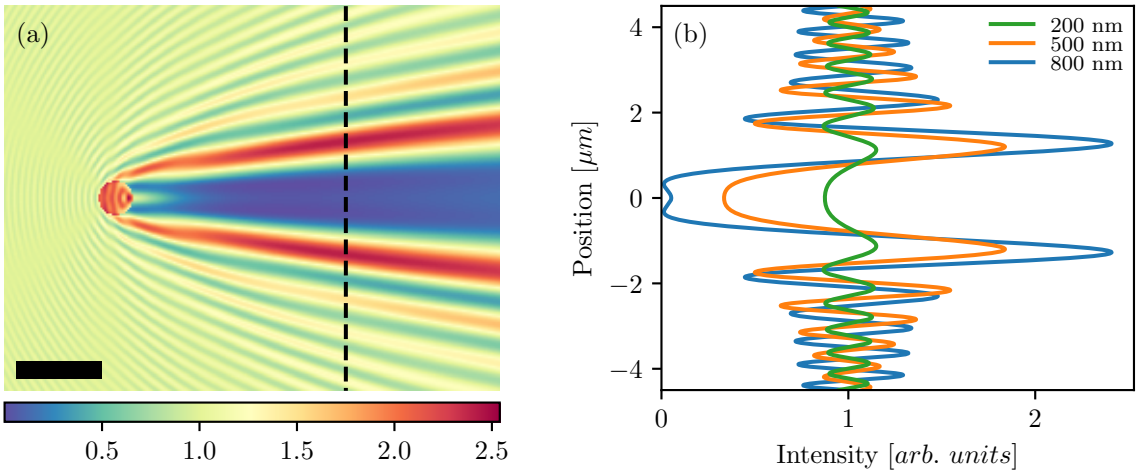

Figure 6.4 Total intensity for a plane wave incident on a cylinder of diameter 800 nm. (a) Map of the intensity showing how the incident plane wave interferes with the scattered field to produce diffraction orders. The scale bar is 2 µm. (b) Intensity profile taken 5 µm after the cylinder centre (marked by the dashed line in (a)) for cylinder diameters of 200 nm, 500 nm and 800 nm.

The total intensity for an 800 nm diameter cylinder is plotted in figure 6.4(a); the parameters for the calculations were the same as in the previous section. From the image, it is evident that if this hole was used in an element it would need to be placed near to the centre since the highest intensity is at small angles from the direction of propagation. Intensity maps similar to this were plotted for the range of diameters and then, for each diameter, a cross section of the total intensity was taken 5 µm beyond the cylinder (marked by the dashed vertical line in figure 6.4(a)). These intensity profiles (see figure 6.4(b)) contain the diffraction orders from the cylinders and are the guides for the positioning of the cylinders in the final focusing element.

In figure 6.4(b), the total intensity is plotted at a distance 5 µm to the right of the cylinder centre for three different cylinder diameters (200 nm, 500 nm and 800 nm). The position as well as the strength of the peaks varies with diameter and it is these two values which influence the design of the element. For these cross sections, it can be seen that the 800 nm diameter cylinder produces a much stronger first order peak. In the focusing element, this diameter would be used for the cylinder nearest the centre. The strongest second order peak is produced by the 500 nm cylinder and so it would be placed second from the centre. The cylinders are then offset laterally from the centre of the element by the position of the peak, i.e. 1.6 µm for the 800 nm diameter cylinder and 2.2 µm for the 500 nm one. The design continued like this until the maximum width of the focusing element was reached. Two constraints during the design was that adjacent cylinders should

have space between them and for a given cylinder the ratio of the peak contributing to the focus compared to any non-contributing peaks should be significant. For instance, in figure 6.4(b) it can be seen that the second order peaks for the 800 nm and the 500 nm are almost equal but that the first order peak is much larger for the larger diameter. This makes the smaller diameter an even better option as it would reduce side peaks in the final element. The final arrays generally consisted of four or six cylinders placed symmetrically about the horizontal axis. To justify the use of the Mie scattering codes, the total intensity calculated with it and that calculated with FDTD software (Lumerical FDTD Solutions) were compared. This comparison is shown in the following section.

6.2.3 3D Simulations

With a first approximation of the diameters of holes that should be used and the position to place them from the analytical simulations, the complete FZPs made up of these holes were simulated in Lumerical's FDTD Solutions (chapter 2 covers the FDTD method and simulation set-up). In the analytical simulations above, all the materials outside the cylinder were approximated as a single material with an effective index of the waveguide mode (TE_0 or TM_0). The FDTD simulations can handle a full description of the outside materials and, considering the finite height of the waveguide core (and the cylinder), they take into account the light that is scattered out of the waveguide. To verify that the analytical approximations produced accurate solutions some of the intensity maps calculated with FDTD are shown in figure 6.5.

The images in figure 6.5(a)–(c) show the total intensity when the fundamental TM mode of the waveguide described earlier in the chapter is incident on a PVA filled hole in the Si_3N_4 core. The images show the intensity in the Si_3N_4 core layer (the top row) and a cross section through the centre of the holes (the bottom row of (a)–(c)). (The side view images have been scaled so that horizontal:vertical is 4:1 to make the different features more easily visible.) The images are normalised such that the peak incident intensity in the Si_3N_4 core layer is equal to 1. The *criss-cross patterned* fluctuation in intensity is an artefact of the simulation set-up which is covered in chapter 2 (section 2.2).

In general terms, the intensity maps calculated using FDTD have a similar profile to the analytical solutions, arising from the interference of the incident mode and the scattered light. It can be seen that the 200 nm diameter hole in figure 6.5(a) produces the weakest scattering—as was the case in the analytical computations—and that increasing the diameter of the hole increases the strength of the scattering. Comparing the intensity maps in figure 6.5(c) and figure 6.4(a) which are both for a diameter of 800 nm, the maximum intensity is lower in the FDTD simulation. One reason for this is the loss of light that is scattered out of the waveguide core which is not accounted for in the analytical calculation. These scattering losses can be seen in the images in the bottom row of figure 6.5(a)–(c). Due to the finite thickness of the Si_3N_4 core and the finite beam width of the incident mode, the mode is diffracted with some power lost to the substrate and cladding. A direct comparison

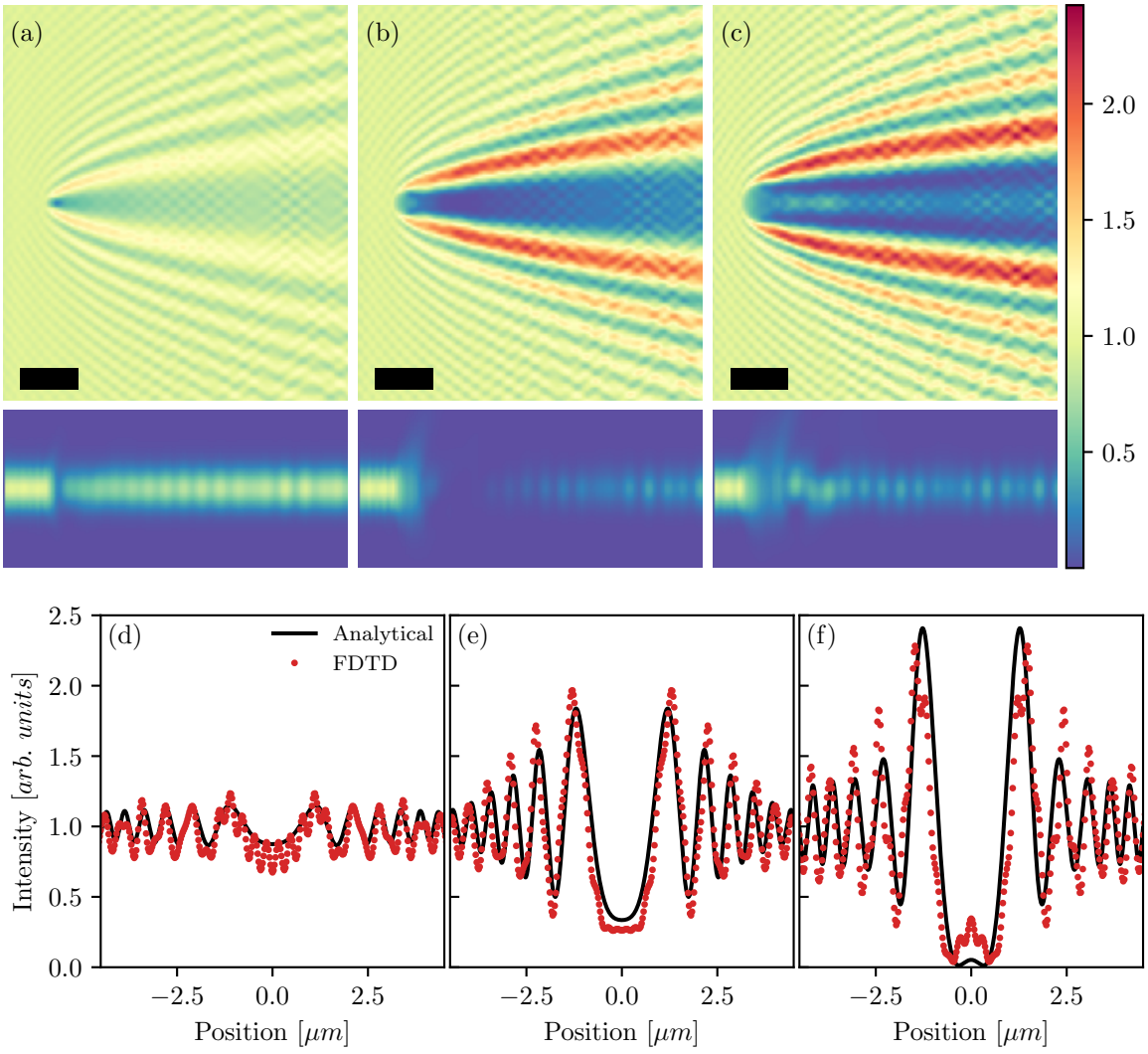

Figure 6.5 FDTD simulations of light scattering by cylindrical holes in the core of a slab waveguide. The diameters of the cylinders are (a) 200 nm, (b) 500 nm and (c) 800 nm and the TM_0 mode is incident. In the top row the intensity in the Si_3N_4 core layer is plotted and in the bottom row a cross section through the centre of the hole is shown. The scale bar is 2 µm. (d)–(f) Comparison of the intensity calculated by analytical and FDTD methods for the holes in (a)–(c), respectively.

of the intensities calculated analytically and by FDTD is given in figure 6.5(d)–(f).

From the plots in figure 6.5(d)–(f) it can be seen how the total intensity 5 µm beyond the hole varies with y position. The plots are for the same diameters of cylinder as shown in (a)–(c) and compare the analytical calculations (solid lines) to the FDTD (circles). There is a good overlap of the intensities calculated by the two methods and the differences in the shape of the profile is due to the 'artefacts' mentioned above while the loss by scattering out of the waveguide also affects the amplitude of the peaks. From the good agreement of the methods, it was decided that it would be acceptable to design the focusing elements using the analytical calculations. Some simulations of the FZPs for different focal lengths are shown in figure 6.6.

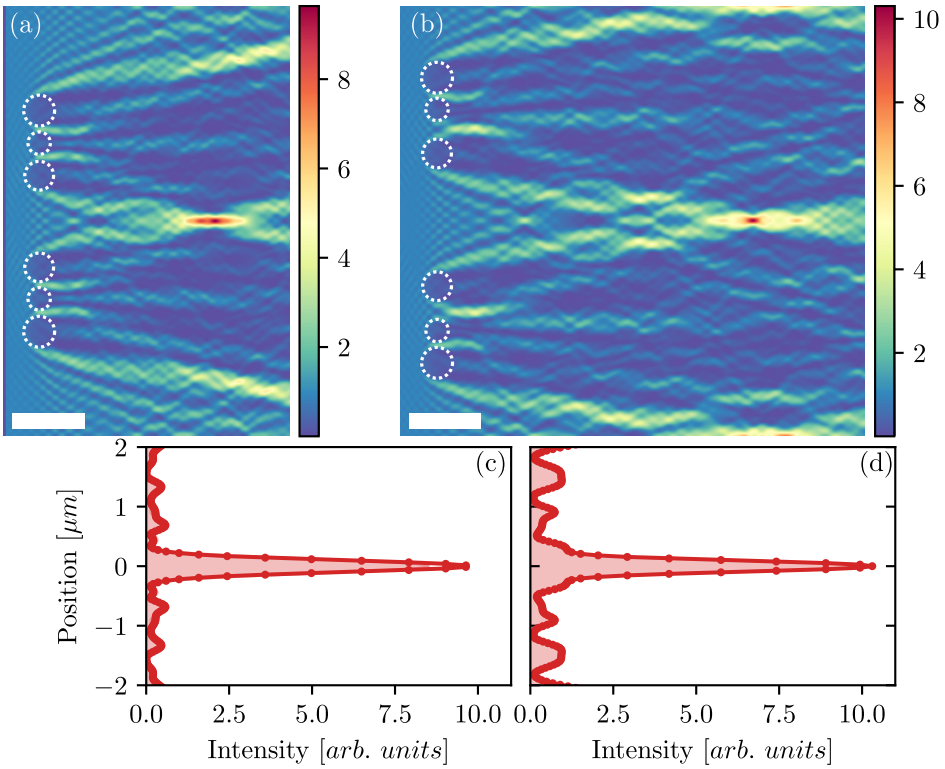

Figure 6.6 Three dimensional FDTD simulations of FZPs. (a) Intensity map in the Si_3N_4 for a focal length of 5 µm; (c) intensity profile in the focal plane of the FZP in (a). The plots in (b) and (d) show the same for a FZP with a 10 µm focal length. The scale bar is 2 µm.

Figure 6.6 contains intensity maps and cross sections for FZPs of focal length 5 µm (in (a) and (c)) and 10 µm (in (b) and (d)). The widths of the FZPs are (a) 7 µm and (b) 8.5 µm and the intensity is normalised to the intensity of the TM_0 mode which is the illumination for these simulations. The intensity maps in (a) and (b) are taken in the centre of the Si_3N_4 layer (where the intensity is expected to be greatest) although the intensity in the film layer was also recorded for comparison with experiment. The curves plotted in (c) and (d) are the intensity profiles along the focal plane for the intensity maps in (a) and (b),

respectively. Both elements focus the incident light to a narrow, high intensity spot that is well isolated from any side peaks.

Both of the focusing elements in figure 6.6 are made of six PVA filled holes in the Si_3N_4 core. For both FZPs, the diameter of the hole nearest the centre of the element is 0.8 µm and moving away from the centre the next holes have diameters of 0.6 and 0.9 µm, respectively; the only difference between the elements in (a) and (b) is the position of the holes used. The FZP in (a) focuses to a spot with a FWHM of 300 nm and a peak intensity 8.5 times the incident intensity; in (b) the focal spot has a FWHM of 230 nm and a peak intensity 10.3 times greater than the incident. (The focal length of the FZP in (b) is shorter than designed at 9 µm.) The design process for these focusing elements was concerned with maximising the power in the focus rather than minimising the width of the focal spot. A focal spot with a FWHM of $\sim\lambda_0/2$ was considered sufficient. However, narrower focal spots could be produced—the limit given by $\lambda_0/2\mathrm{NA}$ suggests a width of ~130 nm could be achieved in Si_3N_4 for $\lambda_0 = 532$ nm—by chaging the design. (The typical FZP has a minimum spot width dependent on the width of the outermost ring.) Simulations for similar FZPs designed for an incident TE_0 mode or different focal length produced equally satisfactory values for spot size and peak intensity. The power reflected to the source by these elements is very low (<1%) when the core of the waveguide is not terminated; it increases to ~10% when the core is terminated and PVA surrounds the core. It is expected that the reflected power would lie towards the lower end of these values if a target or secondary element was being coupled to.

6.3 Fabrication

To define the inclusions in the Si_3N_4 core, a couple of methods were explored. The first was focused ion beam (FIB) milling, a "direct write" process where the inclusions are fabricated in a single step. The second method was the more widely used electron beam lithography (EBL) which is a two step process and involves first patterning a resist layer to act as a mask in the second step—etching away only the undesired material. FIB milling seemed the more reliable method: since it has fewer steps there are fewer chances for errors and it was possible to examine the structures immediately after milling (since the FIB machine is a dual beam microscope it contains an SEM column as well). Having considered these factors, fabrication tests were carried out to find the optimum recipe for FIB milling sub-micron diameter holes into Si_3N_4.

FIB milling is a technique similar to SEM imaging; sub-atomic particles are focused onto a material using electric and magnetic fields. In the FIB system, the beam of electrons is replaced by a beam of ions (in this case gallium ions) which are much heavier. Bombarding a material with a narrowly focused beam of these heavy ions displaces atoms in the material thereby milling it away in a highly controllable fashion. When FIB milling, the displaced material is deposited behind the path the beam traces. (Described as being like a dog

digging a hole.) To examine and correct for this deposition, the fabrication tests varied the parameters beam current (I_b) and energy (E_b) and the number of passes (N_p) the beam made over the milling area. One other variable was the dose (D) which is simply the number of ions directed at the material's surface. Changing N_p is the same as milling the same area N_p times, each time using a dose of $^{D}/_{N_p}$. These parameters essentially control the rate and the force with which the ions strike the Si_3N_4 surface and therefore affect how the surface reacts and is milled. To demonstrate the effects these parameters have on the milled holes, some images of the fabrication tests are shown in figure 6.7. The ideal milled hole would have vertical sidewalls, not penetrate into the substrate and have the specified diameter. To control the beam during milling Raith ELPHY QUANTUM software was used. (These tests were initially carried out on the wafers with a 400 nm thick Si_3N_4 layer and the results could be directly applied to the 180 nm thick Si_3N_4.)

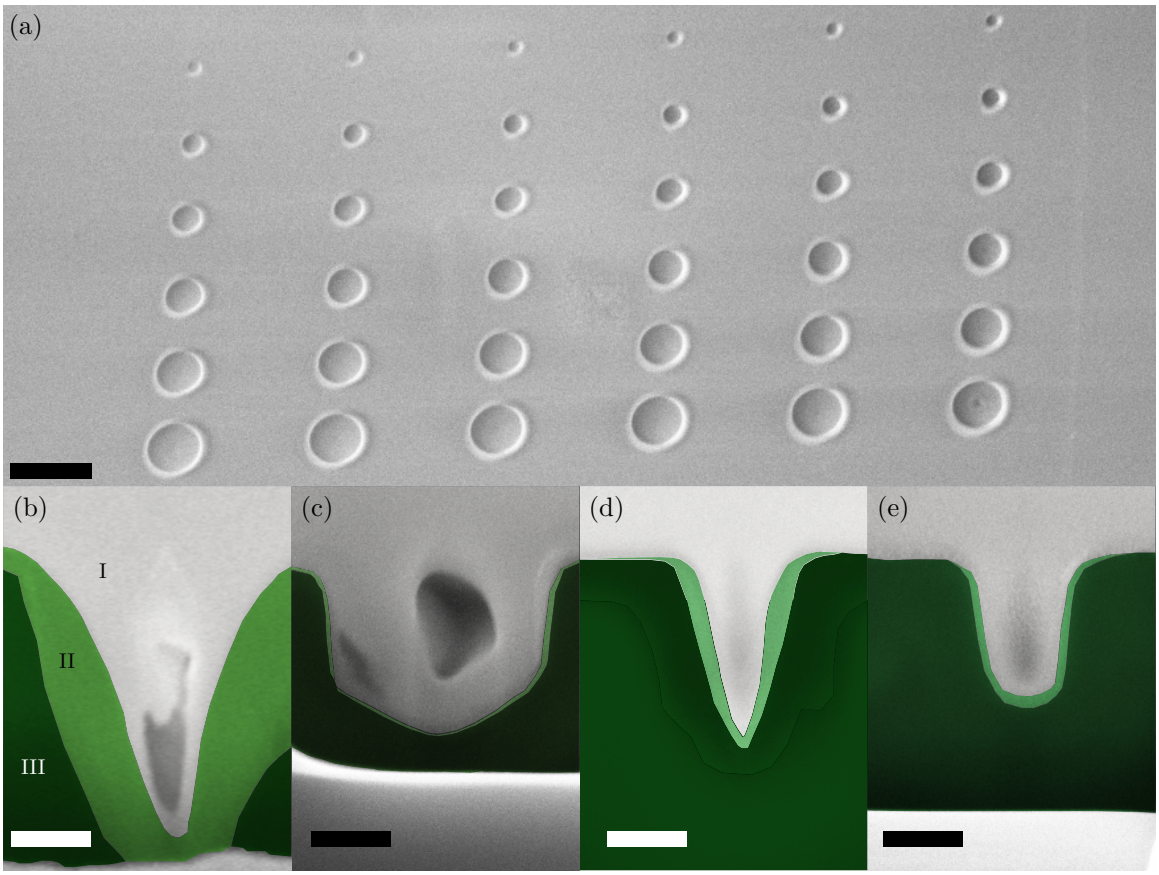

Figure 6.7 SEM images of holes FIB milled into Si_3N_4. (a) Looking down on a set of holes with diameter varying (100 nm–600 nm, 100 nm steps) vertically and dose varying horizontally. Scale bar is 1 µm. (b) Cross section of 600 nm diameter hole milled in a single pass; (c) 600 nm diameter milled in 5 passes; (d) 200 nm diameter, single pass; (e) 200 nm diameter, 5 passes. The images have been false coloured to highlight different regions (marked I, II, III in (b)). Scale bar is 200 nm.

The SEM images in figure 6.7 show a sample of the fabrication tests performed where

the dose, hole diameter and number of passes are varied. Figure 6.7(a) is a view from above the Si_3N_4 surface showing a grid of holes where the diameter was varied from 100 nm to 600 nm in steps of 100 nm in each column while the dose was varied from 100 mC cm^{-2} to 200 mC cm^{-2} in steps of 20 mC cm^{-2} in each row. (I_b was 20 pA and N_p was 5). The diameter of the holes increases slightly moving along the rows and, judging by the darkening colour, it appears that the holes become deeper as well. This is the expected effect of increasing the dose while keeping other parameters constant. The slight deviation from circular of some of the holes is due to the sample drifting during the milling process. This is one of the drawbacks of using $N_p > 1$ because the milled area might move from where the software controlling the beam expects it to be. To get more quantitative information of the sidewalls of the holes, cross sections were taken. These were made by FIB milling along each row. (Before FIB milling, platinum is deposited onto the surface to reinforce the structure being milled so that it doesn't cave in or reshape during the cross sectioning). Some of the cross sections comparing the effects of different N_p are shown in figure 6.7(b)–(e).

Figure 6.7(b) shows a cross section of a FIB milled hole intended to be 600 nm that was milled in a single pass of $D = 120$ mC cm^{-2} and $I_b = 20$ pA. (Each hole in (b)–(e) was milled at $I_b = 20$ pA; it was found during the tests that reducing I_b did not greatly improve the holes and only increased the milling time and that increasing I_b reduced the fine control required for milling.) The lightest region (marked I) is the platinum which shows the angle of the sidewalls and the depth of the hole. The hole goes through the entire Si_3N_4 layer and even into the substrate but is much narrower at the bottom (<100 nm) than at the top (~600 nm) because of what is believed to be the redeposition of the milled material (marked II). Measurement of the sidewall angle gave a nominal value of 50° (where 90° would correspond to perfectly vertical sidewalls), although it can be seen that the sidewalls are curved. (The darkest region, marked III, is untouched Si_3N_4.) The inconsistent diameter of the hole and the curvature of the sidewalls make it clear that this is not the ideal case. Figure 6.7(c) shows a cross section for a hole intended to have a diameter of 500 nm (when fabricated this was 600 nm) which was milled with a higher dose ($D = 180$ mC cm^{-2}) and more passes ($N_p = 5$). It can be seen that by increasing N_p the dose required to mill through the Si_3N_4 layer was increased. It is immediately apparent that the sidewalls are much steeper (typically >80°) and that the hole is shallower (though it still goes through the entire core layer). There is also less redeposited material left around the edges of the hole. Of (b) and (c) the parameters chosen to mill (c) clearly performed better. The cross sections in (d) and (e) are for 200 nm diameter with the parameters of (b) and (c), respectively. Again it is clear that using $N_p > 1$ improves the sidewall angle of the holes with the hole in figure 6.7(d) being conical. For early experiments, the holes and FZPs were fabricated using FIB milling with the parameters of 6.7(c) and (e). Later, aspects of the FIB system and the possible redeposition forced fabrication of the structures to switch from the FIB process to a more standard EBL one in certain cases.

As stated in section 6.2.1, the lower limit on cylinder diameter was 150 nm which was

set to ease the fabrication process. (A cylinder any smaller than this would cause near negligible scattering in any case.) Defining consistent structures 150 nm in size is not a straightforward procedure for e-beam patterning and is simply beyond the capabilities of many UV patterning facilities (which would be necessary for large scale production). The EBL process used for defining the structures was previously established within the group for depositing metals by the lift-off procedure—here the mask defined by EBL is used as an etch mask rather than a deposition mask. The resist used for the EBL process was PMMA A6 which was spin-coated to a thickness of ~300 nm. PMMA is a positive tone resist meaning that the exposed area is removed when immersed in a developing solution (MIBK:IPA). The remaining PMMA then acted as an etch mask during an ICP etch with Ar and CHF_3 which defined the cylinders in the Si_3N_4 layer.

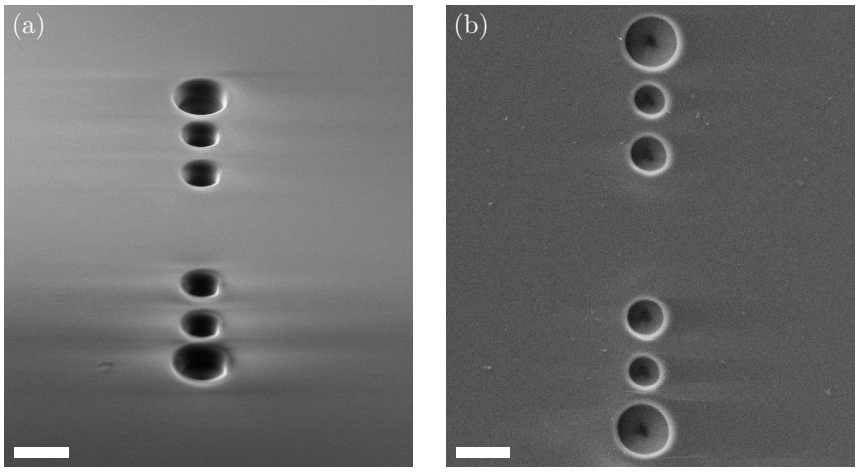

Figure 6.8 FZPs fabricated by FIB milling. (a) Angled SEM image of a FZP in a slab waveguide. (b) SEM image of FZP used to determine hole position and diameter. Scale bar is 1 µm.

SEM images of two FZPs used in experiment are shown in figure 6.8. These FZPs were fabricated by FIB milling of a slab waveguide. For both of the FZPs, the diameter of the holes were intended to be 600 nm, 500 nm and 900 nm moving outwards from the centre. The image in figure 6.8(a) was taken at an angle to try and get an idea of the sidewalls of the holes; in (b) the diameters of the fabricated holes could be measured and were found to be larger than designed at 660 nm, 560 nm and 950 nm. Using SEM images of these and other FZPs, the simulations were updated to match the fabricated structures so that they could be compared with experimental measurements.

6.4 Experiment

The set-up used for these measurements was described and shown in the previous chapter (see figure 5.4 in section 5.2). The structures were fabricated 2–3 mm from the waveguide's input end-face to avoid any complications of the laser beam directly illuminating the struc-

tures. The experimental images in this chapter are of the fluorescence of the RhB doped PVA film (with a couple of exceptions which are stated). The concentration of the RhB was the same as in the previous work so that the modes would propagate to the structures without much loss. However, in keeping the absorption losses low, the fluorescence which is excited is weak and the intensities in the images are thus quite low. Ideally, an optimisation of the fluorescent dye concentration would be performed or the dye would cover only the area near the structures. Unlike in the previous chapter, scattered images of the FZP focusing elements do not give a clear view of the intensity distribution near the structure as they are dominated by the scattering of the individual holes. In most cases, the Si_3N_4 core layer is not terminated and the focused beam is allowed to propagate far beyond the lens. In any final device, the core layer would be terminated at the focal plane of the FZP to allow for coupling to the subsequent element—most likely a plasmonic focusing element. The method of imaging the fluorescence provides adequate information on the focusing abilities of the FZPs in any case. A couple of examples of FZPs focusing to the end-face of a waveguide are briefly covered at the end of the chapter.

6.4.1 Individual holes

Before any full arrays were fabricated, a number of isolated holes were fabricated and measured to verify the simulated intensity maps. Holes with diameters ranging from 300 nm–900 nm were etched all the way through the Si_3N_4 core layer of the slab waveguide structure (shown earlier in figure 6.2). The RhB doped PVA solution was then spin coated on the Si_3N_4 to a thickness of ~100 nm. Light was coupled into the slab waveguide as described in earlier chapters and the diffraction of the waveguide mode by the holes was imaged and compared with simulations. Fluorescence images of a waveguide mode being diffracted by a 900 nm diameter hole are shown in figure 6.9.

The images in figure 6.9(a) and (b) are experimental intensity maps for the diffraction of a mode incident on a hole in the waveguide core. For comparison, simulated intensity maps are shown in 6.9(c) and (d). The simulated images have been 'blurred' to the same resolution as the experimental images—the method for this is described in chapter 2—to give a more realistic comparison. The intensity in each image is normalised so that the incident intensity is 1. For the experimental images, this was done by averaging the fluorescence over a 10 µm × 10 µm area before the hole and dividing the intensity everywhere by this value. The incident intensity was kept low to avoid photobleaching the dye and due to the low intensity of fluorescence there is some CCD noise in the images. However, the diffraction patterns match well with those of the FDTD simulations.

The simulated intensity maps in figure 6.9(c) and (d) are cross sections taken in the middle of the PVA film layer. The simulation was over a smaller area than shown in the experimental image but both sets of images are on the same scale. Compared to the experimental images, the simulated intensity maps have a greater contrast (the difference between the maximum and minimum intensity values) but the profiles are similar. Unlike

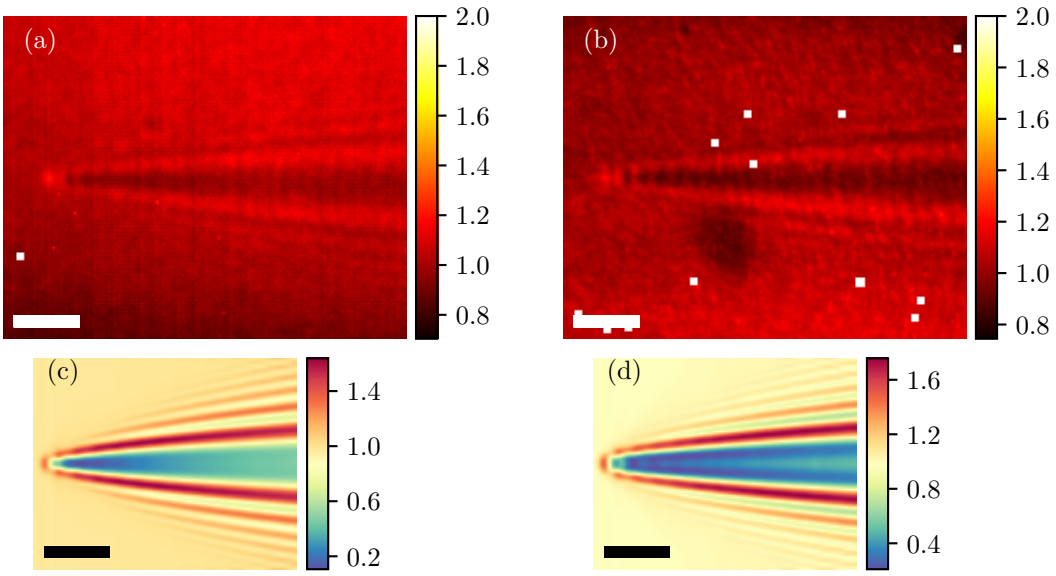

Figure 6.9 Diffraction of a mode by a hole in the waveguide core. (a), (b) Experimental images for a 600 nm and 900 nm diameter hole, respectively. (c), (d) Simulated intensity maps for the same structures as (a) and (b) which have been blurred to have the same resolution as the experimental images. Scale bar is 5 µm.

earlier simulations, the outer diffraction orders do not become distinguishable until a few microns after the hole. In intensity profiles taken from the experimental images at a distance of 5 µm beyond the holes only the first peak can be clearly seen, however, the position overlapped well with the positions from simulations. Since the outer diffraction orders are quite weak in the simulated intensity maps after they were blurred, it was decided that the experimental measurements were reliable but limited by the resolution of the imaging set-up. With the scattering of a mode verified experimentally, some complete FZPs were fabricated and measured.

6.4.2 Fresnel Zone Plates

Measurements of the FZPs were made by the same method that was used for the individual holes. A number of FZPs with focal lengths of 5 µm and 10 µm were fabricated in slab waveguides. Experimental, fluorescence images of two of the focusing elements are shown in figure 6.10.

Figure 6.10(a) and (b) are experimentally measured intensity maps of FZPs intended to have focal lengths of 5 µm and 10 µm, respectively. From the experimental images the focal lengths are closer to 7 µm and 12 µm. The increase of focal length is a result of the fabricated FZPs differing from the simulated ones. The focal length is sensitive to the positioning and size of the holes and the fabricated elements would need to match these for the focal lengths to be identical. The sidewalls of the holes not being perfectly vertical may also cause discrepancies between simulation and experiment. Again, the images are

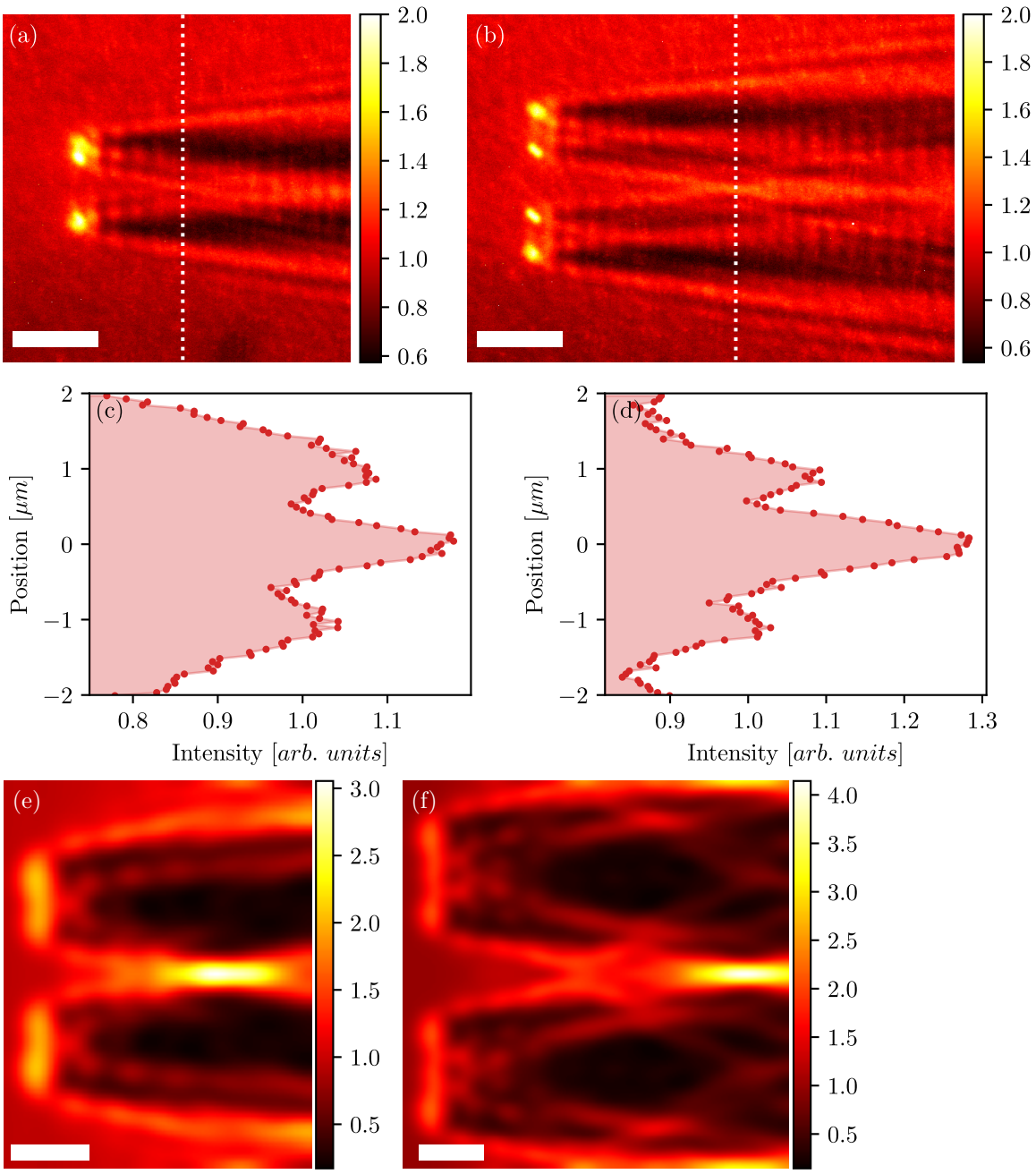

Figure 6.10 Diffractive focusing by an array of holes in the core of a slab waveguide. (a) Experimental intensity map for an element designed to focus light at a distance of 5 µm. (c) Intensity profile taken along the focal plane of the element in (a). (b) and (d) show the same for an element with a designed focal length of 10 µm. The scale bar is 5 µm. (e) and (f) are simulated intensity maps in the PVA film for the elements shown in (a) and (b); the intensity has been normalised such that the incident intensity in the PVA layer is 1. The scale bar is 2 µm.

normalised to the incident intensity. The focusing element in figure 6.10(a) consists of four holes—the two nearest to the centre have diameters of 780 nm and the two nearest the edges have 950 nm—and the overlap of their diffraction patterns can be seen to form a focus ~6 µm beyond the element. As with the experimental images of the individual holes, the maximum intensity is not a lot greater than the incident intensity and this is partly due to the size of the features being smaller than the resolution. (The contrast in the images might be improved by optimising the concentration of the fluorescent dye.) A cross section of the intensity across the focus is plotted in figure 6.10(c). Due to the low intensity levels, several rows of pixels were averaged to make the plots—this has the negative effect of reducing the peak intensity and broadening the width but without the averaging, the plots are too *jittery* to allow meaningful conclusions be drawn. The plot shows a central peak which is overlapped by lower intensity side peaks. A definitive FWHM for the focal spot cannot be determined though it would appear to be less than 1 µm. The maximum intensity of the focus is ~1.2 times the incident intensity which is not great for a focusing element but for sub-resolution features the intensity might be higher than measured. (This was shown in chapter 2.)

The focusing element shown in figure 6.10(b) consists of six holes: 880 nm, 700 nm and 940 nm moving outwards from the centre of the element. As with the FZP in (a), the individual diffraction orders can be seen to overlap and form a focus. The FZP in (b) appears to focus light to a higher intensity which might be expected as it has a greater width than the FZP in (a). The intensity profile across the focus (figure 6.10(d)) shows the increased peak intensity and a decrease of the side peak intensity, however the side peaks are still not fully resolved from the central focus. Again, it is difficult to go beyond putting an upper bound of 1 µm on the FWHM of the focal spot but the peak intensity for this element is ~1.3 times the input. The oscillations of the intensity directly beyond the FZPs in (a) and (b) were caused by the reflection from the Si base of light scattered out of the waveguide core by the holes.

For comparison, some simulated intensity maps are shown in figure 6.10(e) and (f). (The simulations are on a different size scale to the experimental images.) The maps were calculated for the intensity in the PVA film layer to match with the experimental images and they give some insight into the experimental images. In the simulated intensity maps the scattering of the individual holes at the element (the bright vertical lines to the left of the images) are constant across the element; this suggests that each hole is equally illuminated and that they all contribute to the focus. In contrast, the experimental images show uneven scattering at the element. This is most likely due differences between the fabricated structures and the simulated structures; the simulated structures are perfectly circular and have perfectly vertical sidewalls with no roughness.

The other FZPs that were measured produced similar results. Generally, the focal spot was overlapped by side peaks and the maximum intensity in the focus was ~1.2. The measurements of these samples could be improved by using an imaging set-up with a greater

resolution and a CCD sensor with better sensitivity for low light levels. In experimental images a higher intensity but wider 'secondary focus' was formed farther from the lens than designed. This second spot was obscured from simulation because of the limitations of the size of the simulation region but gives further evidence to the method of design.

Although the values of peak intensity and focal spot width are not as impressive as the values calculated in simulations, part of this is caused by the experimental set-up and optimising it could improve the measured values. One other reason for the disparity between simulated and measured intensities are that the simulated images map the intensity on an infinitely thin slice while the experimental images map the fluorescence from a 100 nm thick layer. Having a finite thickness, the features are not as sharp as in simulations.

Secondary focus

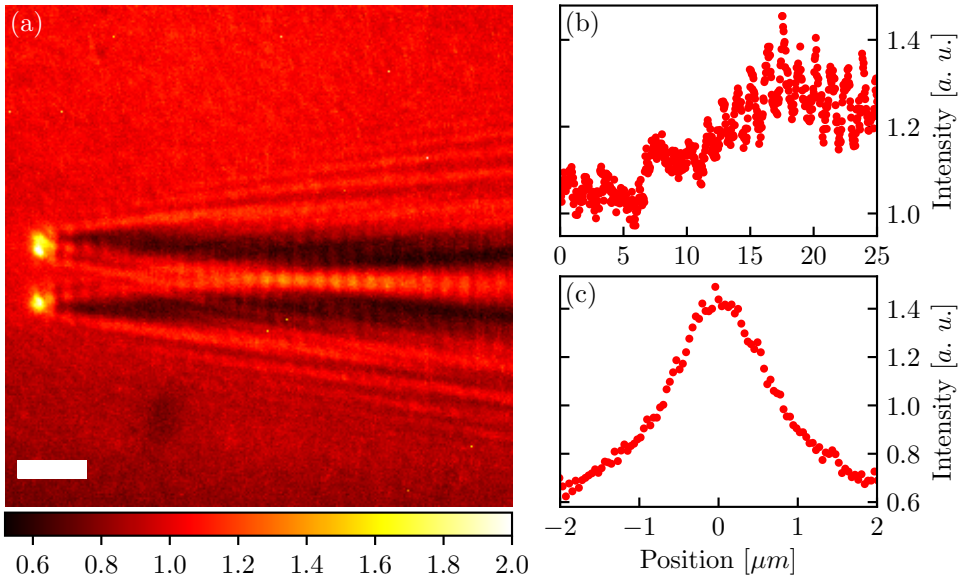

Figure 6.11 Light focusing beyond designed focus. (a) Experimentally measured intensity map for a FZP. The scale bar is 5 µm. (b) Longitudinal intensity profile through the focus of the FZP. (c) Transverse intensity profile through the focus.

The image in figure 6.11 is the experimentally measured fluorescence for a FZP similar to the one shown in figure 6.10(a). The FZP was intended to focus at a distance of 5 µm and while there is a weak focus slightly beyond this distance, a more intense peak is formed at a distance of ~20 µm. This secondary focus has a peak intensity of ~1.5× the incident intensity. The intensity profile plotted in figure 6.11(b) is taken along the propagation direction, through the centre of the focus. Disregarding the oscillations, it can be seen that the maximum intensity is ~18 µm beyond the focusing element. ('0' corresponds to the position of the FZP). In figure 6.11(c) a transverse cross section of the intensity at the focus is plotted. Unlike the plots in figure 6.10(c) and (d), this intensity profile contains only a single peak. The FWHM of the peak is ~1.4 µm which is larger than the diffraction limit

of the imaging set-up and larger than would be desired in applications.

6.5 FZP in Rectangular Waveguides

In applications, an integrated optical focusing element would more likely be incorporated into a rectangular waveguide than a slab waveguide. To demonstrate the practicality of these designs for rectangular waveguides a few meaurements are shown here. The design method for a FZP in a rectangular waveguide is very similar to the method described earlier. One difference in this configuration is that the holes towards the outside of the focusing element have less of an influence because the incident mode is weaker away from the centre of the waveguide—as was seen for the microdisk simulations in the previous chapter. The mode of the rectangular waveguide was found using Lumerical's FDE (see chapter 2) and although for this illumination the incident intensity varies across a hole, there is no drastic change of the scattered fields. To extend the design, a second type of FZP is shown here; this design aimed to position the holes along a curve rather than a straight line as with the FZPs shown earlier. To position the holes for this type of FZP, the change from the earlier method was to replace the linear profile taken 5 µm beyond each hole with an arc of radius 5 µm. Two fabricated FZPs are shown in figure 6.12.

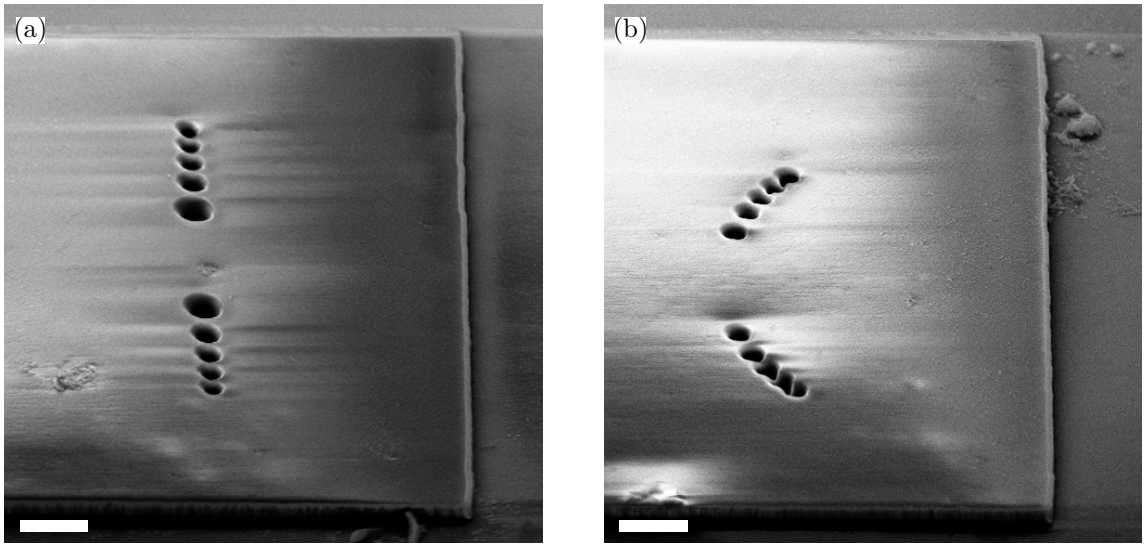

Figure 6.12 FZPs in rectangular waveguides. (a) SEM image of a linear FZP in a 10 µm wide rectangular waveguide. (b) Curved FZP in a waveguide of the same width. The scale bar is 1 µm.

The SEM images in figure 6.12 show FZPs designed to focus onto the end-face of the waveguide. The waveguide core is 10 µm wide in both cases. The holes were FIB milled into the waveguide core after the waveguide was fabricated by EBL. (The waveguide and FZP could be fabricated in a single EBL process but at the time the EBL was being done with a negative tone resist which would have made defining the holes within the core unreliable.) The curved FZP was used as it would keep the 'hole-focus' distance smaller thus increasing

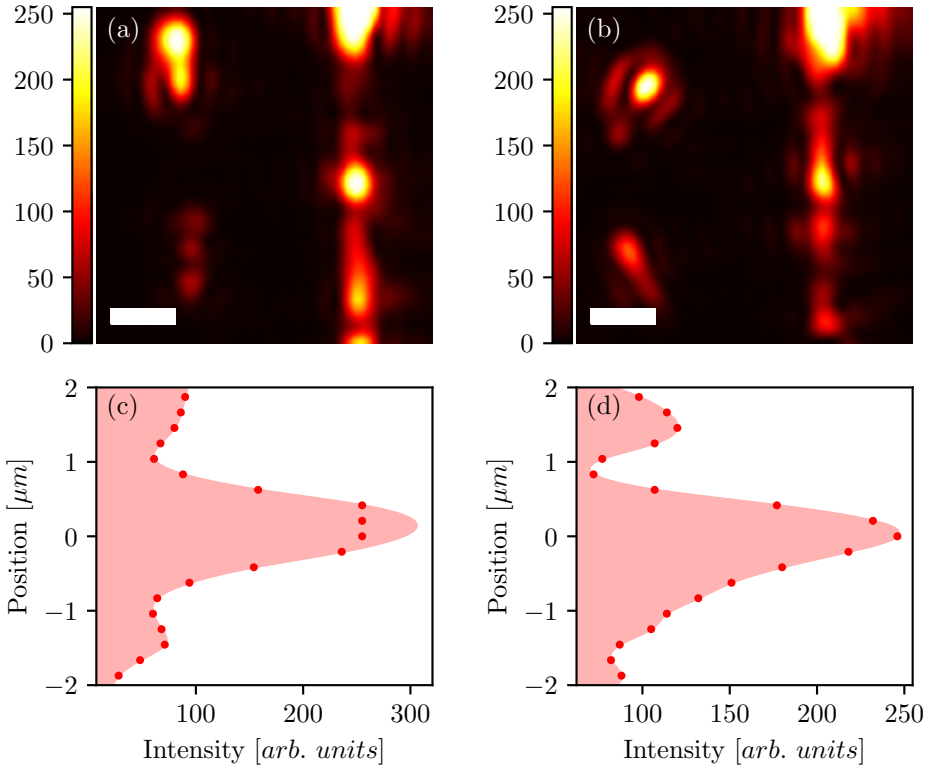

Figure 6.13 FZP focusing elements in rectangular waveguides. (a) Experimental image of the scattered light for the FZP shown in figure 6.12(a); (c) Plot of the intensity profile along the end-face of the waveguide in (a). (b) and (d) show similar for the FZP in figure 6.12(b). The scale bar is 1 µm.

the intensity since the intensity of the scattered field decreases with distance. Both elements were designed to have focal lengths of 5 µm and so were positioned 5 µm before the end of the waveguide core. For these structures no PVA cladding was used and the measurements taken were of the scattered light. Experimental scattered light images of focusing elements similar to those in figure 6.12 are shown in figure 6.13.

For the rectangular waveguides, the separation of the input to the waveguide and the focusing element was less than in the slab case and to avoid light from the laser beam entering the imaging system, a microscope objective with a lower magnification and lower NA was used. This reduced the resolution of the images and the data plotted in figure 6.13 has been interpolated (rather than being shown pixelated). The image in figure 6.13(a) shows the light scattered when a mode of the rectangular waveguide was incident on the FZP shown in figure 6.12(a). An intense spot was formed on the end-face of the waveguide, however, since the top half of the FZP itself scattered more light it is unlikely that the illumination was ideal. The intensity along the end-face of the waveguide is plotted in figure 6.13(c) and the width of the central peak is ~900 nm which was the limit for the imaging set-up. The same measurements were made of the curved FZP and are shown in figure 6.13(b) and (d).

The illumination for the element in (b) was more even across the FZP. Again, the element focused to a spot on the end-face ~900 nm in width. It is expected that a curved FZP could produce a more intense (and possibly narrower) focus since the holes towards the outer edges of the element are nearer to the focus than they would be in a linear element. (The higher angle scattering also increases the effective NA of the focusing element.) Although it is difficult to give quantitative measures of the focusing efficiency or focal spot size from these measurements, it is clear that the FZPs can produce an intense, narrow spot on the end-face of the waveguide and thus could be used to couple into other elements.

6.6 Conclusions

Focusing of a waveguide mode by a structure contained within the core was demonstrated. The structure consisted of holes etched into the core which were either filled with PVA for the slab waveguide measurements or with air for the rectangular waveguide measurements. The positioning and size of the individual holes in the focusing element was determined from analytical simulations of scattering by cylinders and the complete focusing element was simulated using 3D FDTD software. Experimental measurements of the elements verified the focusing of slab and rectangular waveguide modes.

The holes were made in the waveguide core by FIB, milling (and later by ICP etching). It was found that milling a region numerous times with a low dose of ions gave the best results. However, when the sample 'drifted' on the stage of the FIB milling numerous times caused the holes to become misshapen. The sidewalls were adequately vertical ($>80°$ the interfaces of the materials) and smooth. Holes etched using ICP (with an etch mask defined in EBL) were not as smooth though they did not suffer from the problems of drifting.

3D FDTD simulations of the individual holes showed that some light was scattered out of the waveguide and thus lost, reducing the light gathering efficiency of the element. The holes did not reflect much light ($\ll 1\%$) back toward the source however, making them suited for scenarios where back reflections would cause issues for other elements. The 3D simulations matched the analytical simulations for an infinitely tall cylinder so the design of the full element could be done with the analytical caluculations which are much faster. Simulations of the focusing elements suggested focal spot widths smaller than 230 nm ($\sim 0.43\lambda_0$) and a peak intensity more than ten times the incident intensity. The design of the focusing element was based on gathering power rather than minimising the focal spot width and it is expected that a narrower focus could be achieved with similar elements.

Experimental measurements of the FZPs and individual holes were made by imaging the fluorescence of a thin dye doped film which was coated on the surface of the waveguide core. (Some measurements were made of rectangular waveguides by imaging the scattered light at the end-face of the waveguide.) The resolution of the images was limited by the optical imaging set-up but the scattering of the individual holes and focusing of modes by complete elements was observed. The measured focal widths of the elements were closer to

1 µm and the intensity was ~1.3× the incident intensity. However, there was good agreement between the profiles of the experimental and simulated intensity maps after the simulated images were blurred to a resolution similar to the experimental set-up. One factor for the discrepancy in the absolute values is believed to be that certain holes in the element did not scatter as much (compared to others) as simulations predicted. Improvements to the experimental set-up—e.g. optimised dye concentration, higher NA imaging system—might also produce a better match to the theoretical simulations.

7 Outlook

In this thesis, the propagation and manipulation of visible light in planar, dielectric waveguides was discussed. Through simulation and experimental measurement, characteristics of slab and rectangular waveguides were demonstrated for multi-mode propagation. Two focusing elements, with sizes and focal lengths of a few micrometres, were presented as integrated optical structures. Simulation of the structures predicted high intensity focal spots and measurements verified the simulations.

Multi-mode propagation in dielectric slab waveguides was investigated experimentally. It was shown that the interference of the modes produces an intensity pattern that is constant in time due to a fixed phase relationship when the modes are excited. The intensity was imaged using a fluorescent dye coated on the surface of the waveguide core. The interference pattern was related to the effective index difference between the propagating modes and experimental measurements of the differences matched well with theory. It was demonstrated that other mode characteristics, such as the relative coupling and propagation losses could be extracted from the intensity pattern.

Similar imaging analysis was demonstrated for rectangular waveguides. In the structures examined here, it was found that the number of modes inhibited quantitative measurements but the analysis could be applied to waveguides which support only a few propagating modes, such as in low refractive index contrast systems. The intermodal coupling caused by micrometre scale bends in the waveguide core was shown along with multi-mode focusing by tapering the core.

A focusing element for integrated optical applications was fabricated and measured. The microdisk was positioned at the end-face of the waveguide and illuminated by a mode radiating from it. Simulations predicted focal spots $\sim 0.4\lambda_0$ wide and intensities five times greater than the incident intensity. Experimental results showed good agreement, however, the efficiency of the focusing element was reduced by light lost as the beam diverged upon exiting the waveguide.

A second focusing element, which was part of the core of the waveguide, was then

investigated. The Fresnel zone plate (FZP) focused a waveguide mode by etching holes in the core to cause scattering. The position and size of the holes were determined from the phase and amplitude calculated from Mie solutions for an infinite cylinder. Simulations of the FZPs suggested focal spots sizes similar to those formed by the microdisk ~$0.4\lambda_0$ but peak intensities ten times greater than the incident intensity were predicted. Experimental measurements of the fabricated structures were limited by the optical imaging system but a clear demonstration of focusing was seen.

The purpose of this thesis was to develop micron scale dielectric focusing elements which could be easily integrated in planar waveguides. The immediate application of these elements was as part of an optical heating element in a HAMR write-head. In recent years, research has been carried out on microspheres as focusing elements while the planar elements studied have generally been tens of micrometres in size. The large field confinement achievable with plasmonic structures has made them the forerunner for nanofocusing. A drawback of plasmonic elements is the localised heating in the plasmonic structure itself. This thesis investigated two dielectric elements focusing elements both a few micrometres in size and integrated with planar dielectric waveguides. The size of the elements means they could be quickly fabricated in industrial scales with UV lithography and easily incorporated with existing designs for HAMR write-heads. Simulations found that both elements focus to spot sizes smaller than 250 nm which would be useful for coupling to micron and sub-micron size plasmonic elements. The small back-reflections from the elements are essential for reducing the light returning to the source; light coupled back into the source can have detrimental effects and reduce its operational lifetime. While fine-tuning may be needed in the fabrication when studying the elements, it is clear that the elements presented here could be used as integrated planar focusing elements.

Further to this, a measurement technique for planar waveguides was presented. The measurement requires only a basic optical imaging set-up but extracts information about the modes propagating in a waveguide and how the modes are perturbed by different waveguide components (e.g. bends). This method provides a simplified alternative to NSOM which, though it can achieve better resolution (as low as ~100 nm), requires specialised equipment. The technique also provides an *in situ* alternative for quantifying the number of modes propagating in a waveguide. This is typically done by coupling modes out of the waveguide using a prism or a grating, thus giving an angular distribution of the modes—different modes will couple out at different angles. However, grating coupling is a destructive method and prism coupling is not well suited to micro/nanophotonics structures due to the size difference of the prism and the waveguide. The method demonstrated in this thesis is ideal for studying mode propagation in micro/nanophotonic waveguides.

It is planned to publish more of the work from this thesis in the coming months. At present, a manuscript on the simulation and experimental measurement of the FZP as a planar focusing element is in the final draft and is planned to be submitted to Optics Letters this month (titled “Planar Focusing Element based on Scattering Structures in a Dielectric

Waveguide"). An abstract on the same topic has been accepted for presentation at CLEO (Conference on Lasers and Electro-Optics) for May 2018. It is also hoped to publish some of the research on rectangular waveguides and on microdisks but the specific content has not yet been finalised and may require further work.

Carrying on from this thesis, initial work could concentrate on improving fabrication methods. The fabrication recipes used in this thesis were adapted from other students' work in which either standalone structures or larger structures on different substrates were made. While some time was put into refining the processes to work for the sizes and material systems used in this thesis, it seems that further improvement is needed. More precise fabrication of the focusing elements should lead to better agreement of the experimental results with the simulations. Such improvements might include reducing the overlap of the waveguide and microdisk, smoothing any sidewall roughness and increasing the sidewall angle of both the microdisk and the FZP elements. Beyond this, the immediate direction of work would be to design different shapes of FZP focusing elements. Most of the work on FZPs presented in this thesis investigated linear arrays of holes, however, it might be expected that a circular array would produce a higher intensity focus as the separation between each hole and the focus would be smaller. Since there is typically a $^1/r^2$ falloff of the intensity moving away from the hole, it is important to minimise the distance to the focus. Other array shapes were considered briefly and research into these could be done straightaway. Perhaps one other thing that could be considered in the immediate follow-on from this thesis is to improve the experimental measurement set-up. The current set-up is limited to a resolution of ~500 nm which is not ideal for quantifying focusing capabilities of different elements. The combination of fabrication limitations and the set-up also inhibited the measurement of elements in rectangular waveguides. This was caused by the large separation needed between the focusing elements and the point where light was coupled into the waveguide. Any initial work after this thesis should concentrate on optimising the fabrication process, improving the measurement set-up and then testing and comparing different array shapes of FZPs. Further work which could be carried out following this is suggested in the section below.

Future Work

Continuing the research into planar, dielectric focusing elements is the main outlook from this thesis. Although the design of different types of focusing elements can be suggested, some modifications which might improve the performance of the existing structures are proposed here. An emerging technique for localised field enhancement is also mentioned briefly.

Reduced separation microdisk

As was seen in chapter 5, the microdisk's focusing capabilities were diminished because of the divergence of the field between the waveguide end-face and the disk itself. The simplest way to reduce the divergence would be to use a thicker core layer, however, this might not always be suitable. To overcome the effects of divergence, the disk could be reshaped into an element similar to a Fresnel lens which would minimise the average separation. A diagram is given in figure 7.1. The sketch is a primitive version but illustrates the concept.

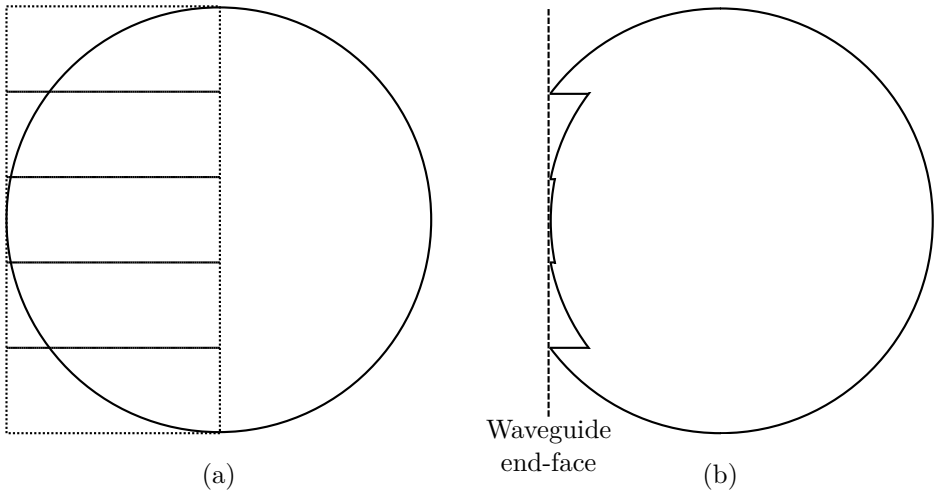

Figure 7.1 Reshaping the microdisk to reduce the waveguide to disk separation. (a) The disk is split into sections of constant width and length. (b) The sections are displaced such that they touch the end-face of the waveguide.

Reducing the separation but maintaining the curvature of the microdisk maintains the refractive characteristics of the focusing element. However, introducing discontinuities might impair the diffractive effects and reduce the focusing efficiency. In fabricating such an element, it would be challenging to maintain the curvature of the different sections but simulations could test the sensitivity to fabrication discrepancies.

Computationally designed focusing element

Recently, computational design of micrometre scale photonic elements has been demonstrated [172, 180, 181]. Structures with sizes of a few micrometres can be simulated relatively quickly with modern computing power, and methods such as the genetic algorithms or inverse electromagnetic design can be used to optimise the performance of a photonic element given an adequate initial structure. Some of these methods are randomised optimisation schemes—e.g. the genetic algorithm simulates the performance of a group of initial structures then chooses aspects of the best performing structures to design the next group (as well as adding some random *mutation*) and continues like this until a specified performance is reached or until the simulated performance plateaus. The structures designed by

these methods are often unseemly, the best designs for optics on this scale are not simply miniaturised versions of 'bulk' optics.

A computational method could be used to redesign the Fresnel zone plate focusing elements presented in chapter 6. The design method in that chapter positioned the individual holes in the focusing element along a straight line but this might not be the best design. Using a computational method, a larger parameter space could be explored (e.g. the position, shape, size, depth of the holes) and the element could be optimised for different needs; the FZPs were designed to maximise the focal power but the light gathering efficiency or the focal spot size could be optimised instead. As this design approach is rarely analytical, structures optimised for a given set of circumstances cannot generally be easily tailored to other circumstances (a complete redesign is necessary). This drawback, along with the time and computing power needed for simulations are the main disadvantages of the computational design method.

Combining dielectric and plasmonic elements

As mentioned earlier in the thesis, a plasmonic focusing element is needed to achieve focal spot sizes far below 100 nm. Coupling light into plasmonic structures requires momentum matching of the incident light field and the plasmonic mode. (Plasmonic modes have high momentum—i.e., short wavelengths—which is how they can produce such small spot sizes.) Using a dielectric element to focus a waveguide mode onto a plasmonic element achieves the momentum matching. However, this arrangement requires multi-step fabrication: first the dielectric focusing element and waveguide are defined and then the metal for the plasmonic structure is deposited. Alignment of these structures is critical to maximising coupling and is not trivial.

Resonant scatterer

To avoid the intrinsic losses associated with plasmonic structures, resonant dielectric particles have been proposed for localisation of light. These structures take advantage of Mie resonances—certain geometrical shapes excite highly localised fields when on resonance, i.e. at certain size to wavelength ratios—to achieve high amplitude scattering. The field localisation of these particles can be similar to that of metallic nanoparticles of comparable size but they do not suffer from the heating associated with metals. However, the dielectric constant of the particles must be quite high (the effects begin to be seen for refractive indexes $\gtrsim 4$) to get strong fields and the structures need to be quite small (typically a few hundred nm).

References

[1] The international disk drive equipment and materials association (IDEMA). (2018). 2016 ASTC technology roadmap, [Online]. Available: http://idema.org/?page_id=5868 (visited on 25/02/2018).

[2] Seagate Technologies LLC. (2017). HAMR: the Next Leap Forward is Now, [Online]. Available: https://blog.seagate.com/intelligent/hamr-next-leap-forward-now/ (visited on 01/02/2018).

[3] P. Lu and S. H. Charap, "Magnetic viscosity in high-density recording", *Journal of Applied Physics*, vol. 75, no. 10, pp. 5768–5770, 1994.

[4] P. Curie, "Propriétés magnétiques des corps a diverses températures", PhD thesis, Université de Paris, 1895.

[5] D. Weller, G. Parker, O. Mosendz, A. Lyberatos, D. Mitin, N. Y. Safonova and M. Albrecht, "Review Article: FePt heat assisted magnetic recording media", *Journal of Vacuum Science & Technology B, Nanotechnology and Microelectronics: Materials, Processing, Measurement, and Phenomena*, vol. 34, no. 6, p. 060 801, 2016.

[6] M. H. Kryder, E. C. Gage, T. W. McDaniel, W. A. Challener, R. E. Rottmayer, G. Ju, Y. T. Hsia and M. F. Erden, "Heat assisted magnetic recording", *Proceedings of the IEEE*, vol. 96, no. 11, pp. 1810–1835, 2008.

[7] R. Hazra. (2012). Heat assisted magnetic recording, [Online]. Available: http://technopits.blogspot.ie/2012/04/hamr-heat-assisted-magnetic-reader_21.html (visited on 23/05/2017).

[8] W. A. Challener, T. W. McDaniel, C. D. Mihalcea, K. R. Mountfield, K. Pelhos and I. K. Sendur, "Light delivery techniques for heat-assisted magnetic recording", *Japanese Journal of Applied Physics*, vol. 42, no. 2S, p. 981, 2003.

[9] W. A. Challener, C. Peng, A. V. Itagi, D. Karns, W. Peng, Y. Peng, X. Yang, X. Zhu, N. J. Gokemeijer, Y.-T. Hsia, G. Ju, R. E. Rottmayer, M. A. Seigler and E. C. Gage, "Heat-assisted magnetic recording by a near-field transducer with efficient optical energy transfer", *Nature Photonics*, vol. 3, pp. 220–224, 2009.

[10] Y. Kong, M. Chabalko, E. Black, S. Powell, J. A. Bain, T. E. Schlesinger and Y. Luo, "Evanescent coupling between dielectric and plasmonic waveguides for HAMR applications", *IEEE Transactions on Magnetics*, vol. 47, no. 10, pp. 2364–2367, 2011.

[11] G. Singh, V. Krishnamurthy, J. Pu and Q. Wang, "Efficient plasmonic transducer for nanoscale optical energy transfer in heat-assisted magnetic recording", *Journal of Lightwave Technology*, vol. 32, no. 17, pp. 3074–3080, 2014.

[12] V. Krishnamurthy, D. K. T. Ng, K. P. Lim and Q. Wang, "Efficient integrated light-delivery system design for HAMR: Maximal optical coupling for transducer and nanowaveguide", *IEEE Transactions on Magnetics*, vol. 52, no. 2, pp. 1–7, 2016.

[13] P. W. Flanigan, C. Zhong, B. Jennings, G. Atcheson, F. Bello, D. McCloskey and J. Donegan, "Efficient waveguide-to-plasmon coupling and adiabatic nanofocusing for HAMR applications", in *Conference on Lasers and Electro-Optics*, Optical Society of America, 2017, FTh4H.7.

[14] B. C. Stipe, T. C. Strand, C. C. Poon, H. Balamane, T. D. Boone, J. A. Katine, J.-L. Li, V. Rawat, H. Nemoto, A. Hirotsune, O. Hellwig, R. Ruiz, E. Dobisz, D. S. Kercher, N. Robertson, T. R. Albrecht and B. D. Terris, "Magnetic recording at $1.5\,\mathrm{Pbit\,m^{-2}}$ using an integrated plasmonic antenna", *Nature Photonics*, vol. 4, pp. 484–488, 2010.

[15] S. P. Powell, E. J. Black, T. E. Schlesinger and J. A. Bain, "The influence of media optical properties on the efficiency of optical power delivery for heat assisted magnetic recording", *Journal of Applied Physics*, vol. 109, no. 7, 07B775, 2011.

[16] T. Matsumoto, F. Akagi, M. Mochizuki, H. Miyamoto and B. Stipe, "Integrated head design using a nanobeak antenna for thermally assisted magnetic recording", *Optics Express*, vol. 20, no. 17, pp. 18 946–18 954, 2012.

[17] J. D. Love and W. M. Henry, "Quantifying loss minimisation in single-mode fibre tapers", *Electronics Letters*, vol. 22, no. 17, pp. 912–914, 1986.

[18] D. Fattal, L. Jingjing, P. Zhen, M. Fiorentino and R. G. Beausoleil, "Flat dielectric grating reflectors with focusing abilities.", *Nature Photonics*, vol. 4, no. 7, pp. 466–470, 2010.

[19] W. A. Challener, C. Mihalcea, C. Peng and K. Pelhos, "Miniature planar solid immersion mirror with focused spot less than a quarter wavelength", *Optics Express*, vol. 13, no. 18, pp. 7189–7197, 2005.

[20] D. McCloskey, K. E. Ballantine, P. R. Eastham and J. F. Donegan, "Photonic nanojets in fresnel zone scattering from non-spherical dielectric particles", *Optics Express*, vol. 23, no. 20, pp. 26 326–26 335, 2015.

[21] H. Choi, D. F. P. Pile, S. Nam, G. Bartal and X. Zhang, "Compressing surface plasmons for nano-scale optical focusing", *Optics Express*, vol. 17, no. 9, pp. 7519–7524, 2009.

[22] Q. Wu, G. D. Feke, R. D. Grober and L. P. Ghislain, "Realization of numerical aperture 2.0 using a gallium phosphide solid immersion lens", *Applied Physics Letters*, vol. 75, no. 26, pp. 4064–4066, 1999.

[23] D. McCloskey and J. F. Donegan, "Planar elliptical solid immersion lens based on a cartesian oval", *Applied Physics Letters*, vol. 103, no. 9, p. 091 101, 2013.

[24] S.-C. Kong, A. V. Sahakian, A. Heifetz, A. Taflove and V. Backman, "Robust detection of deeply subwavelength pits in simulated optical data-storage disks using photonic jets", *Applied Physics Letters*, vol. 92, no. 21, p. 211 102, 2008.

[25] E. McLeod and C. B. Arnold, "Subwavelength direct-write nanopatterning using optically trapped microspheres", *Nature Nanotechnology*, vol. 7, no. 3, pp. 413–417, 2008.

[26] Z. Chen, A. Taflove and V. Backman, "Photonic nanojet enhancement of backscattering of light by nanoparticles: a potential novel visible-light ultramicroscopy technique", *Optics Express*, vol. 12, no. 7, pp. 1214–1220, 2004.

[27] A. Devilez, B. Stout, N. Bonod and E. Popov, "Spectral analysis of three-dimensional photonic jets", *Optics Express*, vol. 16, no. 18, pp. 14 200–14 212, 2008.

[28] B. S. Luk'yanchuk, R. Paniagua-Domínguez, I. Minin, O. Minin and Z. Wang, "Refractive index less than two: photonic nanojets yesterday, today and tomorrow", *Optical Materials Express*, vol. 7, no. 6, pp. 1820–1847, 2017.

[29] D. McCloskey, J. J. Wang and J. Donegan, "Low divergence photonic nanojets from Si_3N_4 microdisks", *Optics Express*, vol. 20, no. 1, pp. 128–140, 2012.

[30] D. K. Gramotnev and S. I. Bozhevolnyi, "Nanofocusing of electromagnetic radiation", *Nature Photonics*, vol. 8, no. 1, pp. 13–22, 2014.

[31] H. Raether, *Surface Plasmons on Smooth and Rough Surfaces and on Gratings*. Berlin, Heidelberg: Springer Berlin Heidelberg, 1988.

[32] R. Ikkawi, N. Amos, Y. Hijazi, D. Litvinov and S. Khizroev, "Design, fabrication, and characterization of near-field apertures for 1 Tbit in^{-2} areal density", *IEEE Transactions on Magnetics*, vol. 44, no. 11, pp. 3364–3367, 2008.

[33] J. Gosciniak, M. Mooney, M. Gubbins and B. Corbett, "Novel droplet near-field transducer for heat-assisted magnetic recording", *Nanophotonics*, vol. 4, no. 1, pp. 503–510, 2015.

[34] X. Xu, N. Zhou, Y. Li and L. Traverso, "Optical and thermal behaviors of plasmonic bowtie aperture and its NSOM characterization for heat-assisted magnetic recording", *IEEE Transactions on Magnetics*, vol. 52, no. 2, pp. 1–5, 2016.

[35] T. W. McDaniel, W. A. Challener and K. Sendur, "Issues in heat-assisted perpendicular recording", *IEEE Transactions on Magnetics*, vol. 39, no. 4, pp. 1972–1979, 2003.

[36] N. Abadía, F. Bello, C. Zhong, P. Flanigan, D. M. McCloskey, C. Wolf, A. Krichevsky, D. Wolf, F. Zong, A. Samani, D. V. Plant and J. F. Donegan, "Optical and thermal analysis of the light-heat conversion process employing an antenna-based hybrid plasmonic waveguide for HAMR", *Optics Express*, vol. 26, no. 2, pp. 1752–1765, 2018.

[37] J. Shang, F. Cheng, M. Dubey, J. M. Kaplan, M. Rawal, X. Jiang, D. S. Newburg, P. A. Sullivan, R. B. Andrade and D. M. Ratner, "An organophosphonate strategy for functionalizing silicon photonic biosensors", *Langmuir*, vol. 28, no. 6, pp. 3338–3344, 2012.

[38] M.-J. Bañuls, R. Puchades and Á. Maquieira, "Chemical surface modifications for the development of silicon-based label-free integrated optical (IO) biosensors: A review", *Analytica Chimica Acta*, vol. 777, pp. 1–16, 2013.

[39] B. Schmidt, V. Almeida, C. Manolatou, S. Preble and M. Lipson, "Nanocavity in a silicon waveguide for ultrasensitive nanoparticle detection", *Applied Physics Letters*, vol. 85, no. 21, pp. 4854–4856, 2004.

[40] T. Stomeo, M. Grande, A. Qualtieri, A. Passaseo, A. Salhi, M. D. Vittorio, D. Biallo, A. D'orazio, M. D. Sario, V. Marrocco, V. Petruzzelli and F. Prudenzano, "Fabrication of force sensors based on two-dimensional photonic crystal technology", *Microelectronic Engineering*, vol. 84, no. 5, pp. 1450–1453, 2007, Proceedings of the 32nd International Conference on Micro- and Nano-Engineering.

[41] J. Jágerská, H. Zhang, Z. Diao, N. L. Thomas and R. Houdré, "Refractive index sensing with an air-slot photonic crystal nanocavity", *Optics Letters*, vol. 35, no. 15, pp. 2523–2525, 2010.

[42] A. Densmore, D.-X. Xu, S. Janz, P. Waldron, T. Mischki, G. Lopinski, A. Delâge, J. Lapointe, P. Cheben, B. Lamontagne and J. H. Schmid, "Spiral-path high-sensitivity silicon photonic wire molecular sensor with temperature-independent response", *Optics Letters*, vol. 33, no. 6, pp. 596–598, 2008.

[43] D.-X. Xu, M. Vachon, A. Densmore, R. Ma, S. Janz, A. Delâge, J. Lapointe, P. Cheben, J. H. Schmid, E. Post, S. Messaoudène and J.-M. Fédéli, "Real-time cancellation of temperature induced resonance shifts in SOI wire waveguide ring resonator label-free biosensor arrays", *Optics Express*, vol. 18, no. 22, pp. 22 867–22 879, 2010.

[44] J. V. Jokerst, J. W. Jacobson, B. D. Bhagwandin, P. N. Floriano, N. Christodoulides and J. T. McDevitt, "Programmable nano-bio-chip sensors: Analytical meets clinical", *Analytical Chemistry*, vol. 82, no. 5, pp. 1571–1579, 2010.

[45] M. Estevez, M. Alvarez and L. Lechuga, "Integrated optical devices for lab-on-a-chip biosensing applications", *Laser & Photonics Reviews*, vol. 6, no. 4, pp. 463–487, 2012.

[46] D. Sikdar and M. Premaratne. (2015). Optical nanoantennas set the stage for a NEMS lab-on-a-chip revolution, [Online]. Available: `http://www.newswise.com/articles/optical-nanoantennas-set-the-stage-for-a-nems-lab-on-a-chip-revolution` (visited on 10/05/2017).

[47] D. Thomson, A. Zilkie, J. E. Bowers, T. Komljenovic, G. T. Reed, L. Vivien, D. Marris-Morini, E. Cassan, L. Virot, J.-M. Fédéli, J.-M. Hartmann, J. H. Schmid, D.-X. Xu, F. Boeuf, P. O'Brien, G. Z. Mashanovich and M. Nedeljkovic, "Roadmap on silicon photonics", *Journal of Optics*, vol. 18, no. 7, p. 073 003, 2016.

[48] Y.-D. Yang, Y. Li, Y.-Z. Huang and A. W. Poon, "Silicon nitride three-mode division multiplexing and wavelength-division multiplexing using asymmetrical directional couplers and microring resonators", *Optics Express*, vol. 22, no. 18, pp. 22 172–22 183, 2014.

[49] A. Alduino and M. Paniccia, "Interconnects: Wiring electronics with light", *Nature Photonics*, vol. 1, no. 3, pp. 153–155, 2007.

[50] C. Gunn, "CMOS photonics for high-speed interconnects", *IEEE Micro*, vol. 26, no. 2, pp. 58–66, 2006.

[51] M. Haurylau, G. Chen, H. Chen, J. Zhang, N. A. Nelson, D. H. Albonesi, E. G. Friedman and P. M. Fauchet, "On-chip optical interconnect roadmap: Challenges and critical directions", *IEEE Journal of Selected Topics in Quantum Electronics*, vol. 12, no. 6, pp. 1699–1705, 2006.

[52] W. S. Zaoui, A. Kunze, W. Vogel, M. Berroth, J. Butschke, F. Letzkus and J. Burghartz, "Bridging the gap between optical fibers and silicon photonic integrated circuits", *Optics Express*, vol. 22, no. 2, pp. 1277–1286, 2014.

[53] C. Kachris and I. Tomkos, "A roadmap on optical interconnects in data centre networks", in *2015 17th International Conference on Transparent Optical Networks (ICTON)*, 2015, pp. 1–3.

[54] C. Dragone, "An $N \times N$ optical multiplexer using a planar arrangement of two star couplers", *IEEE Photonics Technology Letters*, vol. 3, no. 9, pp. 812–815, 1991.

[55] L. Chen, C. R. Doerr, P. Dong and Y.-k. Chen, "Monolithic silicon chip with 10 modulator channels at 25 Gbps and 100 GHz spacing", *Optics Express*, vol. 19, no. 26, B946–B951, 2011.

[56] P. Dong, "Silicon photonic integrated circuits for wavelength-division multiplexing applications", *IEEE Journal of Selected Topics in Quantum Electronics*, vol. 22, no. 6, pp. 370–378, 2016.

[57] M. R. Watts, H. A. Haus and E. P. Ippen, "Integrated mode-evolution-based polarization splitter", *Optics Letters*, vol. 30, no. 9, pp. 967–969, 2005.

[58] H. Fukuda, K. Yamada, T. Tsuchizawa, T. Watanabe, H. Shinojima and S.-i. Itabashi, "Silicon photonic circuit with polarization diversity", *Optics Express*, vol. 16, no. 7, pp. 4872–4880, 2008.

[59] L. Chen, C. R. Doerr and Y.-K. Chen, "Compact polarization rotator on silicon for polarization-diversified circuits", *Optics Letters*, vol. 36, no. 4, pp. 469–471, 2011.

[60] W. D. Sacher, T. Barwicz, B. J. F. Taylor and J. K. S. Poon, "Polarization rotator-splitters in standard active silicon photonics platforms", *Optics Express*, vol. 22, no. 4, pp. 3777–3786, 2014.

[61] K. Preston, S. Manipatruni, A. Gondarenko, C. B. Poitras and M. Lipson, "Deposited silicon high-speed integrated electro-optic modulator", *Optics Express*, vol. 17, no. 7, pp. 5118–5124, 2009.

[62] V. J. Sorger, N. D. Lanzillotti-Kimura, R.-M. Ma and X. Zhang, "Ultra-compact silicon nanophotonic modulator with broadband response", *Nanophotonics*, vol. 1, no. 1, pp. 17–12, 2012.

[63] R. Bruck, K. Vynck, P. Lalanne, B. Mills, D. J. Thomson, G. Z. Mashanovich, G. T. Reed and O. L. Muskens, "All-optical spatial light modulator for reconfigurable silicon photonic circuits", *Optica*, vol. 3, no. 4, pp. 396–402, 2016.

[64] C. M. Wilkes, X. Qiang, J. Wang, R. Santagati, S. Paesani, X. Zhou, D. A. B. Miller, G. D. Marshall, M. G. Thompson and J. L. O'Brien, "60 dB high-extinction auto-configured Mach-Zehnder interferometer", *Optics Letters*, vol. 41, no. 22, pp. 5318–5321, 2016.

[65] R. Haldar, V. Mishra, A. Dutt and S. K. Varshney, "On-chip broadband ultra-compact optical couplers and polarization splitters based on off-centered and non-symmetric slotted Si-wire waveguides", *Journal of Optics*, vol. 18, no. 10, p. 105 801, 2016.

[66] R. Azzam and N. Bashara, *Ellipsometry and polarized light*. North-Holland Publishing Company, 1977.

[67] M. Sochacka, E. L. Lago and Z. Jaroszewicz, "Refractive-index profiling of planar gradient-index waveguides by phase-measuring microinterferometry", *Applied Optics*, vol. 33, no. 16, pp. 3342–3347, 1994.

[68] W. A. Ramadan, E. Fazio and M. Bertolotti, "Measurement of the refractive-index profile of planar waveguides by the use of a double Lloyd's interferometer", *Applied Optics*, vol. 35, no. 31, pp. 6173–6178, 1996.

[69] A. Saftics, E. Agócs, B. Fodor, D. Patkó, P. Petrik, K. Kolari, T. Aalto, P. Fürjes, R. Horvath and S. Kurunczi, "Investigation of thin polymer layers for biosensor applications", *Applied Surface Science*, vol. 281, pp. 66–72, 2013, EMRS 2012 Fall Meeting Symposium on highly precise characterization of materials for nano and bio technologies.

[70] R. Ramponi, R. Osellame and M. Marangoni, "Two straightforward methods for the measurement of optical losses in planar waveguides", *Review of Scientific Instruments*, vol. 73, no. 3, pp. 1117–1120, 2002.

[71] R. G. Hunsperger, "Waveguide input and output couplers", in *Integrated Optics: Theory and Technology*. New York, NY: Springer New York, 2009, pp. 129–152.

[72] J. F. Bauters, M. J. R. Heck, D. John, D. Dai, M.-C. Tien, J. S. Barton, A. Leinse, R. G. Heideman, D. J. Blumenthal and J. E. Bowers, "Ultra-low-loss high-aspect-ratio Si_3N_4 waveguides", *Optics Express*, vol. 19, no. 4, pp. 3163–3174, 2011.

[73] H. Osterberg and L. W. Smith, "Transmission of optical energy along surfaces: Part II, inhomogeneous media", *Journal of the Optical Society of America*, vol. 54, no. 9, pp. 1078–1084, 1964.

[74] J. E. Goell and R. D. Standley, "Integrated optical circuits", *Proceedings of the IEEE*, vol. 58, no. 10, pp. 1504–1512, 1970.

[75] F. Zernike, "Fabrication and measurement of passive components", in *Integrated Optics*, T. Tamir, Ed. Berlin, Heidelberg: Springer Berlin Heidelberg, 1979, pp. 201–241.

[76] R. Ulrich and R. Torge, "Measurement of thin film parameters with a prism coupler", *Applied Optics*, vol. 12, no. 12, pp. 2901–2908, 1973.

[77] P. K. Tien and R. Ulrich, "Theory of prism–film coupler and thin-film light guides", *Journal of the Optical Society of America*, vol. 60, no. 10, pp. 1325–1337, 1970.

[78] H. P. Weber, F. A. Dunn and W. N. Leibolt, "Loss measurements in thin-film optical waveguides", *Applied Optics*, vol. 12, no. 4, pp. 755–757, 1973.

[79] J. Cardin and D. Leduc, "Determination of refractive index, thickness, and the optical losses of thin films from prism-film coupling measurements", *Applied Optics*, vol. 47, no. 7, pp. 894–900, 2008.

[80] K.-S. Chiang and S. Cheng, "Technique of applying the prism-coupler method for accurate measurement of the effective indices of channel waveguides", *Optical Engineering*, vol. 47, no. 3, p. 034 601, 2008.

[81] X. Prieto-Blanco and J. Linares, "Two-mode waveguide characterization by intensity measurements from exit face images", *IEEE Photonics Journal*, vol. 4, no. 1, pp. 65–79, 2012.

[82] L.-W. Luo, N. Ophir, C. P. Chen, L. H. Gabrielli, C. B. Poitras, K. Bergmen and M. Lipson, "WDM-compatible mode-division multiplexing on a silicon chip", *Nature Communications*, vol. 5, p. 3069, 2014.

[83] I. Papakonstantinou, K. Wang, D. R. Selviah and F. A. Fernández, "Transition, radiation and propagation loss in polymer multimode waveguide bends", *Optics Express*, vol. 15, no. 2, pp. 669–679, 2007.

[84] M. Kovar, M. A. Nohe, N. Petersen and P. Norton. (2014). NSOM: Discovering new worlds, [Online]. Available: `https://www.photonics.com/a25127/NSOM_Discovering_New_Worlds` (visited on 23/02/2018).

[85] R. C. Reddick, R. J. Warmack, D. W. Chilcott, S. L. Sharp and T. L. Ferrell, "Photon scanning tunneling microscopy", *Review of Scientific Instruments*, vol. 61, no. 12, pp. 3669–3677, 1990.

[86] E. Betzig, M. Isaacson and A. Lewis, “Collection mode near-field scanning optical microscopy”, *Applied Physics Letters*, vol. 51, no. 25, pp. 2088–2090, 1987.

[87] L. Novotny and B. Hecht, *Principles of Nano-Optics*. Cambridge University Press, 2006.

[88] S. Bourzeix, J. M. Moison, F. Mignard, F. Barthe, A. C. Boccara, C. Licoppe, B. Mersali, M. Allovon and A. Bruno, “Near-field optical imaging of light propagation in semiconductor waveguide structures”, *Applied Physics Letters*, vol. 73, no. 8, pp. 1035–1037, 1998.

[89] D. P. Tsai, C. W. Yang, S.-Z. Lo and H. E. Jackson, “Imaging local index variations in an optical waveguide using a tapping-mode near-field scanning optical microscope”, *Applied Physics Letters*, vol. 75, no. 8, pp. 1039–1041, 1999.

[90] M. L. M. Balistreri, J. P. Korterik, L. Kuipers and N. F. van Hulst, “Local observations of phase singularities in optical fields in waveguide structures”, *Physical Review Letters*, vol. 85, pp. 294–297, 2 2000.

[91] M. L. M. Balistreri, J. P. Korterik, L. Kiupers and N. F. van Hulst, “Phase mapping of optical fields in integrated optical waveguide structures”, *Journal of Lightwave Technology*, vol. 19, no. 8, pp. 1169–1176, 2001.

[92] G. Yuan, K. L. Lear, M. D. Stephens and D. S. Dandy, “Characterization of a 90° waveguide bend using near-field scanning optical microscopy”, *Applied Physics Letters*, vol. 87, no. 19, p. 191 107, 2005.

[93] K. P. Lim, V. Krishnamurthy, J. F. Ying, J. Pu and Q. Wang, “Ultrahigh index and low-loss silicon rich nitride thin film for NIR HAMR optics”, *IEEE Transactions on Magnetics*, vol. 53, no. 5, pp. 1–7, 2017.

[94] J. S. Levy, “Integrated nonlinear optics in silicon nitride waveguides and resonators”, PhD thesis, Cornell University, 2011.

[95] K. Ikeda, R. E. Saperstein, N. Alic and Y. Fainman, “Thermal and Kerr nonlinear properties of plasma-deposited silicon nitride/silicon dioxide waveguides”, *Optics Express*, vol. 16, no. 17, pp. 12 987–12 994, 2008.

[96] G. Gao, D. Chen, S. Tao, Y. Zhang, S. Zhu, X. Xiao and J. Xia, “Silicon nitride O-band (de)multiplexers with low thermal sensitivity”, *Optics Express*, vol. 25, no. 11, pp. 12 260–12 267, 2017.

[97] Y. Huang, J. Song, X. Luo, T.-Y. Liow and G.-Q. Lo, “CMOS compatible monolithic multi-layer Si_3N_4-on-SOI platform for low-loss high performance silicon photonics dense integration”, *Optics Express*, vol. 22, no. 18, pp. 21 859–21 865, 2014.

[98] K. Shang, S. Pathak, B. Guan, G. Liu and S. J. B. Yoo, “Low-loss compact multilayer silicon nitride platform for 3D photonic integrated circuits”, *Optics Express*, vol. 23, no. 16, pp. 21 334–21 342, 2015.

[99] W. D. Sacher, Z. Yong, J. C. Mikkelsen, A. Bois, Y. Yang, J. C. Mak, P. Dumais, D. Goodwill, C. Ma, J. Jeong, E. Bernier and J. K. Poon, "Multilayer silicon nitride-on-silicon integrated photonic platform for 3D photonic circuits", in *Conference on Lasers and Electro-Optics*, Optical Society of America, 2016, JTh4C.3.

[100] W. Xie, T. Stöferle, G. Rainò, T. Aubert, Y. Zhu, R. F. Mahrt, E. Brainis, Z. Hens and D. V. Thourhout, "Integrated silicon nitride microdisk lasers based on quantum dots", in *Conference on Lasers and Electro-Optics*, Optical Society of America, 2016, JTh4B.6.

[101] S. Romero-García, F. Merget, F. Zhong, H. Finkelstein and J. Witzens, "Silicon nitride CMOS-compatible platform for integrated photonics applications at visible wavelengths", *Optics Express*, vol. 21, no. 12, pp. 14 036–14 046, 2013.

[102] A. Rahim, E. Ryckeboer, A. Z. Subramanian, S. Clemmen, B. Kuyken, A. Dhakal, A. Raza, A. Hermans, M. Muneeb, S. Dhoore, Y. Li, U. Dave, P. Bienstman, N. L. Thomas, G. Roelkens, D. V. Thourhout, P. Helin, S. Severi, X. Rottenberg and R. Baets, "Expanding the silicon photonics portfolio with silicon nitride photonic integrated circuits", *Journal of Lightwave Technology*, vol. 35, no. 4, pp. 639–649, 2017.

[103] B. Momeni, E. S. Hosseini and A. Adibi, "Planar photonic crystal microspectrometers in silicon-nitride for the visible range", *Optics Express*, vol. 17, no. 19, pp. 17 060–17 069, 2009.

[104] T. Barwicz, M. A. Popovic, P. T. Rakich, M. R. Watts, H. A. Haus, E. P. Ippen and H. I. Smith, "Microring-resonator-based add-drop filters in SiN: fabrication and analysis", *Optics Express*, vol. 12, no. 7, pp. 1437–1442, 2004.

[105] N. Ma, C. Li and A. W. Poon, "Laterally coupled hexagonal micropillar resonator add-drop filters in silicon nitride", *IEEE Photonics Technology Letters*, vol. 16, no. 11, pp. 2487–2489, 2004.

[106] P. Pintus, F. D. Pasquale and J. E. Bowers, "Integrated TE and TM optical circulators on ultra-low-loss silicon nitride platform", *Optics Express*, vol. 21, no. 4, pp. 5041–5052, 2013.

[107] Y. Liu, M. Davanco, V. Aksyuk and K. Srinivasan, "Electromagnetically induced transparency and wideband wavelength conversion in silicon nitride microdisk optomechanical resonators", *Physical Review Letters*, vol. 110, no. 22, p. 223 603, 2013.

[108] W. D. Sacher, Y. Huang, L. Ding, T. Barwicz, J. C. Mikkelsen, B. J. F. Taylor, G.-Q. Lo and J. K. S. Poon, "Polarization rotator-splitters and controllers in a Si_3N_4-on-SOI integrated photonics platform", *Optics Express*, vol. 22, no. 9, pp. 11 167–11 174, 2014.

[109] C. H. Henry, R. F. Kazarinov, H. J. Lee, K. J. Orlowsky and L. E. Katz, "Low loss Si_3N_4-SiO_2 optical waveguides on si", *Applied Optics*, vol. 26, no. 13, pp. 2621–2624, 1987.

[110] A. Z. Subramanian, P. Neutens, A. Dhakal, R. Jansen, T. Claes, X. Rottenberg, F. Peyskens, S. Selvaraja, P. Helin, B. D. Bois, K. Leyssens, S. Severi, P. Deshpande, R. Baets and P. V. Dorpe, "Low-loss singlemode PECVD silicon nitride photonic wire waveguides for 532–900 nm wavelength window fabricated within a CMOS pilot line", *IEEE Photonics Journal*, vol. 5, no. 6, pp. 2 202 809–2 202 809, 2013.

[111] N. Daldosso, M. Melchiorri, F. Riboli, F. Sbrana, L. Pavesi, G. Pucker, C. Kompocholis, M. Crivellari, P. Bellutti and A. Lui, "Fabrication and optical characterization of thin two-dimensional Si_3N_4 waveguides", *Materials Science in Semiconductor Processing*, vol. 7, no. 4–6, pp. 453–458, 2004, Papers presented at the E-MRS 2004 Spring Meeting Symposium C: New Materials in Future Silicon Technology.

[112] A. Gondarenko, J. S. Levy and M. Lipson, "High confinement micron-scale silicon nitride high Q ring resonator", *Optics Express*, vol. 17, no. 14, pp. 11 366–11 370, 2009.

[113] E. S. Hosseini, S. Yegnanarayanan, A. H. Atabaki, M. Soltani and A. Adibi, "High quality planar silicon nitride microdisk resonators for integrated photonics in the visible wavelength range", *Optics Express*, vol. 17, no. 17, pp. 14 543–14 551, 2009.

[114] D. T. Spencer, J. F. Bauters, M. J. R. Heck and J. E. Bowers, "Integrated waveguide coupled Si_3N_4 resonators in the ultrahigh-Q regime", *Optica*, vol. 1, no. 3, pp. 153–157, 2014.

[115] J. S. Levy, M. A. Foster, A. L. Gaeta and M. Lipson, "Harmonic generation in silicon nitride ring resonators", *Optics Express*, vol. 19, no. 12, pp. 11 415–11 421, 2011.

[116] T. Ning, H. Pietarinen, O. Hyvärinen, J. Simonen, G. Genty and M. Kauranen, "Strong second-harmonic generation in silicon nitride films", *Applied Physics Letters*, vol. 100, no. 16, p. 161 902, 2012.

[117] Y. Okawachi, K. Saha, J. S. Levy, Y. H. Wen, M. Lipson and A. L. Gaeta, "Octave-spanning frequency comb generation in a silicon nitride chip", *Optics Letters*, vol. 36, no. 17, pp. 3398–3400, 2011.

[118] L. Wang, L. Chang, N. Volet, M. H. P. Pfeiffer, M. Zervas, H. Guo, T. J. Kippenberg and J. E. Bowers, "Frequency comb generation in the green using silicon nitride microresonators", *Laser & Photonics Reviews*, vol. 10, no. 4, pp. 631–638, 2016.

[119] H. Zhao, B. Kuyken, S. Clemmen, F. Leo, A. Subramanian, A. Dhakal, P. Helin, S. Severi, E. Brainis, G. Roelkens and R. Baets, "Visible-to-near-infrared octave spanning supercontinuum generation in a silicon nitride waveguide", *Optics Letters*, vol. 40, no. 10, pp. 2177–2180, 2015.

[120] J. P. Epping, T. Hellwig, M. Hoekman, R. Mateman, A. Leinse, R. G. Heideman, A. van Rees, P. J. van der Slot, C. J. Lee, C. Fallnich and K.-J. Boller, "On-chip visible-to-infrared supercontinuum generation with more than 495 THz spectral bandwidth", *Optics Express*, vol. 23, no. 15, pp. 19 596–19 604, 2015.

[121] X. Liu, M. Pu, B. Zhou, C. J. Krückel, A. Fülöp, V. Torres-Company and M. Bache, "Octave-spanning supercontinuum generation in a silicon-rich nitride waveguide", in *Conference on Lasers and Electro-Optics*, Optical Society of America, 2016, SW1Q.3.

[122] V. Weldon, D. McInerney, R. Phelan, M. Lynch and J. Donegan, "Characteristics of several NIR tuneable diode lasers for spectroscopic based gas sensing: A comparison", *Spectrochimica Acta Part A: Molecular and Biomolecular Spectroscopy*, vol. 63, no. 5, pp. 1013–1020, 2006, 5th International Conference on Tunable Diode Laser Spectroscopy, 2005.

[123] D. P. O'Dwyer, C. F. Phelan, K. E. Ballantine, Y. P. Rakovich, J. G. Lunney and J. F. Donegan, "Conical diffraction of linearly polarised light controls the angular position of a microscopic object", *Optics Express*, vol. 18, no. 26, pp. 27 319–27 326, 2010.

[124] D. P. O'Dwyer, K. E. Ballantine, C. F. Phelan, J. G. Lunney and J. F. Donegan, "Optical trapping using cascade conical refraction of light", *Optics Express*, vol. 20, no. 19, pp. 21 119–21 125, 2012.

[125] M. Soltani, J. Lin, R. A. Forties, J. T. Inman, S. N. Saraf, R. M. Fulbright, M. Lipson and M. D. Wang, "Nanophotonic trapping for precise manipulation of biomolecular arrays", *Nature Nanotechnology*, vol. 9, no. 6, pp. 448–452, 2014.

[126] A. Gorin, A. Jaouad, E. Grondin, V. Aimez and P. Charette, "Fabrication of silicon nitride waveguides for visible-light using PECVD: A study of the effect of plasma frequency on optical properties", *Optics Express*, vol. 16, no. 18, pp. 13 509–13 516, 2008.

[127] K. Okamoto, "Chapter 2 - Planar optical waveguides", in *Fundamentals of Optical Waveguides (Second Edition)*, K. Okamoto, Ed., Second Edition, Burlington: Academic Press, 2006, pp. 13–55.

[128] E. Jones, T. Oliphant, P. Peterson *et al.* (2018). SciPy: Open source scientific tools for Python, [Online]. Available: `http://www.scipy.org/` (visited on 05/02/2018).

[129] E. A. J. Marcatili, "Dielectric rectangular waveguide and directional coupler for integrated optics", *The Bell System Technical Journal*, vol. 48, no. 7, pp. 2071–2102, 1969.

[130] A. Kumar, K. Thyagarajan and A. K. Ghatak, "Analysis of rectangular-core dielectric waveguides: an accurate perturbation approach", *Optics Letters*, vol. 8, no. 1, pp. 63–65, 1983.

[131] G. Mie, “Beitrage zur optik truber medien, speziell kolloidaler metallosungen”, *Annalen der Physik*, vol. 330, no. 3, pp. 377–445, 1908.

[132] C. F. Bohren and D. R. Huffman, “A Potpourri of Particles”, in *Absorption and Scattering of Light by Small Particles*. Wiley-VCH Verlag GmbH, 2007, pp. 181–223.

[133] L. Tsang, J. A. Kong and K.-H. Ding, “Introduction to Electromagnetic Scattering by a Single Particle”, in *Scattering of Electromagnetic Waves: Theories and Applications*. John Wiley & Sons, Inc., 2002, pp. 1–52.

[134] W. J. Wiscombe, “Improved Mie scattering algorithms”, *Applied Optics*, vol. 19, no. 9, pp. 1505–1509, 1980.

[135] Lumerical Solutions Inc. (2015). Lumerical FDTD Solver Description, [Online]. Available: `https://kb.lumerical.com/en/solvers_finite_difference_eigenmode.html` (visited on 07/03/2017).

[136] A. Taflove and S. C. Hagness, *Computational Electrodynamics: The Finite-Difference Time-Domain Method*. Artech House, 2005.

[137] K. S. Kunz and R. J. Luebbers, *The Finite Difference Time Domain Method for Electromagnetics*. CRC Press, 1993.

[138] K. Yee, “Numerical solution of initial boundary value problems involving Maxwell’s equations in isotropic media”, *IEEE Transactions on Antennas and Propagation*, vol. 14, no. 3, pp. 302–307, 1966.

[139] Z. Zhu and T. G. Brown, “Full-vectorial finite-difference analysis of microstructured optical fibers”, *Optics Express*, vol. 10, no. 17, pp. 853–864, 2002.

[140] J. W. S. 3rd Baron Rayleigh, “XV. on the theory of optical images, with special reference to the microscope”, *The London, Edinburgh, and Dublin Philosophical Magazine and Journal of Science*, vol. 42, no. 255, pp. 167–195, 1896.

[141] Q. Q. Cheng, T. Li, R. Y. Guo, L. Li, S. M. Wang and S. N. Zhu, “Direct observation of guided-mode interference in polymer-loaded plasmonic waveguide”, *Applied Physics Letters*, vol. 101, no. 17, p. 171 116, 2012.

[142] B. C. Wonsiewicz, W. G. French, P. D. Lazay and J. R. Simpson, “Automatic analysis of interferograms: Optical waveguide refractive index profiles”, *Applied Optics*, vol. 15, no. 4, pp. 1048–1052, 1976.

[143] P. K. Tien, R. Ulrich and R. J. Martin, “Modes of propagating light waves in thin deposited semiconductor films”, *Applied Physics Letters*, vol. 14, no. 9, pp. 291–294, 1969.

[144] L. McCaughan and E. Bergmann, “Index distribution of optical waveguides from their mode profile”, *Journal of Lightwave Technology*, vol. 1, no. 1, pp. 241–244, 1983.

[145] D. P. Tsai, H. E. Jackson, R. C. Reddick, S. H. Sharp and R. J. Warmack, "Photon scanning tunneling microscope study of optical waveguides", *Applied Physics Letters*, vol. 56, no. 16, pp. 1515–1517, 1990.

[146] E. Flück, M. Hammer, A. M. Otter, J. P. Korterik, L. Kuipers and N. F. van Hulst, "Amplitude and phase evolution of optical fields inside periodic photonic structures", *Journal of Lightwave Technology*, vol. 21, no. 5, pp. 1384–1393, 2003.

[147] G. G. Stokes, "XXX. On the change of refrangibility of light", *Philosophical Transactions of the Royal Society of London*, vol. 142, pp. 463–562, 1852.

[148] J. W. Cooley and J. W. Tukey, "An algorithm for the machine calculation of complex Fourier series", *Mathematics of Computation*, vol. 19, no. 2, pp. 297–301, 1965.

[149] K. Gut, "Mode beat measurement of planar optical waveguide", in *Proceedings of SPIE*, vol. 5956, 2005, 59561N.

[150] Y. A. Vlasov and S. J. McNab, "Losses in single-mode silicon-on-insulator strip waveguides and bends", *Optics Express*, vol. 12, no. 8, pp. 1622–1631, 2004.

[151] M.-S. Kwon and J.-S. Shin, "Investigation of 90° submicrometer radius bends of metal-insulator-silicon-insulator-metal waveguides", *Optics Letters*, vol. 39, no. 3, pp. 715–718, 2014.

[152] L. H. Gabrielli, D. Liu, S. G. Johnson and M. Lipson, "On-chip transformation optics for multimode waveguide bends", *Nature Communications*, vol. 3, p. 1217, 2012.

[153] Z. Han, P. Zhang and S. I. Bozhevolnyi, "Calculation of bending losses for highly confined modes of optical waveguides with transformation optics", *Optics Letters*, vol. 38, no. 11, pp. 1778–1780, 2013.

[154] M. L. M. Balistreri, J. P. Korterik, L. Kuipers and N. F. van Hulst, "Visualization of mode transformation in a planar waveguide splitter by near-field optical phase imaging", *Applied Physics Letters*, vol. 79, no. 7, pp. 910–912, 2001.

[155] F. Gesuele, C. Pang, G. Leblond, S. Blaize, A. Bruyant, P. Royer, R. Deturche, P. Maddalena and G. Lerondel, "Towards routine near-field optical characterization of silicon-based photonic structures: An optical mode analysis in integrated waveguides by transmission AFM-based SNOM", *Physica E: Low-dimensional Systems and Nanostructures*, vol. 41, no. 6, pp. 1130–1134, 2009, Proceedings of the E-MRS 2008 Symposium C: Frontiers in Silicon-Based Photonics.

[156] D. McCloskey, "Visible light scattering from micron scale silicon nitride structures", PhD thesis, Trinity College Dublin, 2012.

[157] A. V. Itagi and W. A. Challener, "Optics of photonic nanojets", *Journal of the Optical Society of America A*, vol. 22, no. 12, pp. 2847–2858, 2005.

[158] C.-Y. Liu, "Superenhanced photonic nanojet by core-shell microcylinders", *Physics Letters A*, vol. 376, no. 23, pp. 1856–1860, 2012.

[159] A. Darafsheh and D. Bollinger, "Systematic study of the characteristics of the photonic nanojets formed by dielectric microcylinders", *Optics Communications*, vol. 402, pp. 270–275, 2017.

[160] G. Gu, R. Zhou, Z. Chen, H. Xu, G. Cai, Z. Cai and M. Hong, "Super-long photonic nanojet generated from liquid-filled hollow microcylinder", *Optics Letters*, vol. 40, no. 4, pp. 625–628, 2015.

[161] C.-Y. Liu and K.-L. Hsiao, "Direct imaging of optimal photonic nanojets from core-shell microcylinders", *Optics Letters*, vol. 40, no. 22, pp. 5303–5306, 2015.

[162] X. Cui, D. Erni and C. Hafner, "Optical forces on metallic nanoparticles induced by a photonic nanojet", *Optics Express*, vol. 16, no. 18, pp. 13 560–13 568, 2008.

[163] S.-C. Kong, A. Sahakian, A. Taflove and V. Backman, "Photonic nanojet-enabled optical data storage", *Optics Express*, vol. 16, no. 18, pp. 13 713–13 719, 2008.

[164] H. Wang, X. Wu and D. Shen, "Trapping and manipulating nanoparticles in photonic nanojets", *Optics Letters*, vol. 41, no. 7, pp. 1652–1655, 2016.

[165] M. Zwanenburg, J. Bongaerts, J. Peters, D. Riese and J. van der Veen, "Focusing of coherent X-rays in a tapered planar waveguide", *Physica B: Condensed Matter*, vol. 283, no. 1, pp. 285–288, 2000.

[166] T. Rausch, C. Mihalcea, K. Pelhos, D. Karns, K. Mountfield, Y. A. Kubota, X. Wu, G. Ju, W. A. Challener, C. Peng, L. Li, Y.-T. Hsia and E. C. Gage, "Near field heat assisted magnetic recording with a planar solid immersion lens", *Japanese Journal of Applied Physics*, vol. 45, no. 2S, p. 1314, 2006.

[167] A. Heifetz, J. J. Simpson, S.-C. Kong, A. Taflove and V. Backman, "Subdiffraction optical resolution of a gold nanosphere located within the nanojet of a Mie-resonant dielectric microsphere", *Optics Express*, vol. 15, no. 25, pp. 17 334–17 342, 2007.

[168] S. Yang, A. Taflove and V. Backman, "Experimental confirmation at visible light wavelengths of the backscattering enhancement phenomenon of the photonic nanojet", *Optics Express*, vol. 19, no. 8, pp. 7084–7093, 2011.

[169] X. Wan, B. Shen and R. Menon, "Diffractive lens design for optimized focusing", *Journal of the Optical Society of America A*, vol. 31, no. 12, B27–B33, 2014.

[170] L. Feng, K. A. Tetz, B. Slutsky, V. Lomakin and Y. Fainman, "Fourier plasmonics: Diffractive focusing of in-plane surface plasmon polariton waves", *Applied Physics Letters*, vol. 91, no. 8, p. 081 101, 2007.

[171] A. V. Baez, "Fresnel zone plate for optical image formation using extreme ultraviolet and soft X radiation", *Journal of the Optical Society of America*, vol. 51, no. 4, pp. 405–412, 1961.

[172] J. Marqués-Hueso, L. Sanchis, B. Cluzel, F. de Fornel and J. P. Martínez-Pastor, "Genetic algorithm designed silicon integrated photonic lens operating at 1550 nm", *Applied Physics Letters*, vol. 97, no. 7, p. 071 115, 2010.

[173] W. Chang and P. Ashley, "Fresnel lenses in optical waveguides", *IEEE Journal of Quantum Electronics*, vol. 16, no. 7, pp. 744–754, Jul. 1980.

[174] P. Mottier and S. Valette, "Integrated fresnel lens on thermally oxidized silicon substrate", *Applied Optics*, vol. 20, no. 9, pp. 1630–1634, May 1981.

[175] T. Suhara, K. Kobayashi, H. Nishihara and J. Koyama, "Graded-index fresnel lenses for integrated optics", *Applied Optics*, vol. 21, no. 11, pp. 1966–1971, 1982.

[176] S. Valette, A. Morque and P. Mottier, "High-performance integrated Fresnel lenses on oxidised silicon substrate", *Electronics Letters*, vol. 18, no. 1, pp. 13–15, 1982.

[177] A. L. Belostotsky and A. S. Leonov, "Design of aplanatic waveguide Fresnel lenses and aberration-free planar optical systems", *Journal of Lightwave Technology*, vol. 11, no. 8, pp. 1314–1319, 1993.

[178] N. Fabre, L. Lalouat, B. Cluzel, X. Mélique, D. Lippens, F. de Fornel and O. Vanbésien, "Optical near-field microscopy of light focusing through a photonic crystal flat lens", *Physical Review Letters*, vol. 101, p. 073 901, 7 2008.

[179] B. D. F. Casse, W. T. Lu, R. K. Banyal, Y. J. Huang, S. Selvarasah, M. R. Dokmeci, C. H. Perry and S. Sridhar, "Imaging with subwavelength resolution by a generalized superlens at infrared wavelengths", *Optics Letters*, vol. 34, no. 13, pp. 1994–1996, 2009.

[180] A. Y. Piggott, J. Lu, K. G. Lagoudakis, J. Petykiewicz, T. M. Babinec and J. Vučković, "Inverse design and demonstration of a compact and broadband on-chip wavelength demultiplexer", *Nature Photonics*, vol. 9, no. 6, pp. 374–377, 2015.

[181] B. Shen, P. Wang, R. Polson and R. Menon, "An integrated-nanophotonics polarization beamsplitter with $2.4 \times 2.4\,\mu m^2$ footprint.", *Nature Photonics*, vol. 9, no. 6, pp. 378–382, 2015.